

DESIGN AND ANALYSIS OF A VTOL TILT-WING UAV

A THESIS SUBMITTED TO
THE GRADUATE SCHOOL OF NATURAL AND APPLIED SCIENCES
OF
MIDDLE EAST TECHNICAL UNIVERSITY

BY

HASAN ÇAKIR

IN PARTIAL FULFILLMENT OF THE REQUIREMENTS
FOR
THE DEGREE OF DOCTOR OF PHILOSOPHY
IN
AEROSPACE ENGINEERING

JULY 2020

Approval of the thesis:

DESIGN AND ANALYSIS OF A VTOL TILT-WING UAV

submitted by **HASAN ÇAKIR** in partial fulfillment of the requirements for the degree of **Doctor of Philosophy in Aerospace Engineering, Middle East Technical University** by,

Prof. Dr. Halil Kalıpçılar
Dean, Graduate School of **Natural and Applied Sciences**

Prof. Dr. İsmail Hakkı Tuncer
Head of the Department, **Aerospace Engineering**

Prof. Dr. Dilek Funda Kurtuluş
Supervisor, **Aerospace Engineering, METU**

Examining Committee Members:

Prof. Dr. Ozan Tekinalp
Aerospace Eng., METU

Prof. Dr. Dilek Funda Kurtuluş
Aerospace Eng., METU

Assoc. Prof. Dr. Munir Elfarra
Aerospace Eng., Ankara Yıldırım Beyazıt University

Assist. Prof. Dr. Ali Türker Kutay
Aerospace Eng., METU

Assist. Prof. Dr. Kutluk Bilge Arıkan
Mechanical Eng., TED University

Date: 14.07.2020

I hereby declare that all information in this document has been obtained and presented in accordance with academic rules and ethical conduct. I also declare that, as required by these rules and conduct, I have fully cited and referenced all material and results that are not original to this work.

Name, Last name: Hasan akır

Signature:

ABSTRACT

DESIGN AND ANALYSIS OF A VTOL TILT-WING UAV

Çakır, Hasan
Doctor of Philosophy, Aerospace Engineering
Supervisor : Prof. Dr. D.Funda Kurtuluş

July 2020, 160 pages

In this study, the design and analysis of a UAV, which is capable of vertical take-off and landing using fixed six rotors placed on the tilt-wing and tilt-tail, will be explained. The aircraft has four rotors on its wing and two rotors on its tail. The main wing and horizontal tail are capable of 90° tilting. Both aerodynamic and thrust forces are used during VTOL, transition, and forward flight. Aerodynamic analysis has been performed in ANSYS Fluent v.18. A non-linear six DoF model, involving a 3D CAD model of the aircraft, has been created in MATLAB/Simulink/Simscape. The transition problem has been identified. Three types of robust controller algorithms, involving PID and LQR methods, have been implemented to overcome the challenges which have been faced while performing transition from vertical to horizontal flight phase and vice versa, and the results of each controller type have been compared concerning those criteria. Eight trim points have been identified for full mission profile, and for each trim condition, separate controllers have been designed. Gain scheduling has been employed between trim points for a smooth transition.

Keywords: VTOL, Tilt-Wing, UAV

ÖZ

DIKEY İNİŞ/KALKIŞ YAPABİLEN VE KANATLARI DÖNDÜRÜLEBİLEN BİR İNSANSIZ HAVA ARACININ TASARIMI VE ANALİZİ

Çakır, Hasan
Doktora, Havacılık ve Uzay Mühendisliği
Tez Yöneticisi: Prof. Dr. D.Funda Kurtuluş

Temmuz 2020, 160 sayfa

Bu çalışmada, hareketli kanadına ve kuyruğuna yerleştirilmiş altı motor sayesinde dikey iniş ve kalkış yapabilen bir insansız hava aracının tasarımı ve analizi anlatılacaktır. Uçağın kanatlarında dört, yatay kuyruğunda iki motor bulunmaktadır. Uçağın kanadı ve kuyruğu 90° dönebilme kabiliyetine sahiptir. Dikey iniş ve kalkış sırasında ve dikey uçuştan yataya uçuşa geçiş sırasında hem aerodinamik hem de itki kuvveti kullanılmaktadır. Aerodinamik analizler ANSYS Fluent v.18 ile yapılmıştır. MATLAB/Simulink/Simscape’de uçağın üç boyutlu modelini de içeren altı serbestlik dereceli doğrusal olmayan model tasarlanmıştır. Dikey uçuştan yatay uçuşa geçiş problemi tanımlanmış olup geçiş uçuşu sırasındaki problemlerin aşılması amacıyla PID ve LQR methodları kullanılarak üç tip gürbüz kontrolcü algoritması uygulanmış ve kontrolcü tiplerinin geçiş uçuşu sırasındaki davranışları karşılaştırılmıştır. Sekiz adet trim noktası belirlenerek her bir trim noktası için ayrı ayrı kontrolcü tasarlanmıştır. Yumuşak bir geçiş yapmak için trim noktaları arasında kazanç ayarlaması yapılmıştır.

Anahtar Kelimeler: Dikey İniş ve Kalkış, Hareketli Kanat, İHA

To my wife and son...

ACKNOWLEDGMENTS

I would like to express my deep and sincere gratitude to my supervisor Prof. Dr. Dilek Funda Kurtuluş for her invaluable kindness, patience, academic experience, and knowledge at all steps of this study. I could not be able to complete this study without her support, energy, and enthusiasm.

I would also like to thank my thesis advisory committee members Asst. Prof. Dr. Ali Türker Kutay, Asst. Prof. Dr. Kutluk Bilge Arıkan and my older sister Prof. Dr. Sevgi Demirel, for reviewing my thesis.

I would like to express my very great gratitude to my family for their love, support, and encouragement throughout my life.

Lastly, but most importantly, I would like to express my eternal love to my wife for her love, support, and encouragement throughout doctoral education.

TABLE OF CONTENTS

ABSTRACT.....	v
ÖZ	vi
ACKNOWLEDGMENTS	viii
TABLE OF CONTENTS.....	ix
LIST OF TABLES	xiii
LIST OF FIGURES	xv
LIST OF ABBREVIATIONS	xix
LIST OF SYMBOLS	xx
CHAPTERS	
1 INTRODUCTION	1
1.1 Motivation	1
1.2 Problem Statement	2
1.3 Literature Survey.....	3
1.3.1 Platforms in the Literature	3
1.3.2 Control System Architectures in the Literature	8
1.4 Research Question and Contributions to the Literature	13
1.5 Major Objectives	14
1.6 Outline of the Thesis	15
2 AERODYNAMIC DESIGN AND OPTIMIZATION.....	17
2.1 Conceptual design	17
2.1.1 Design Requirements	17
2.1.2 Planform Selection.....	18

2.1.3	Conceptual Design Process	24
2.2	Preliminary Design	25
2.2.1	Design Methodology	25
2.2.2	Design Trade Studies	27
2.3	Final Aircraft	35
2.4	Aerodynamic Analysis.....	37
2.4.1	Aerodynamic Database Generation.....	43
2.4.2	Aerodynamic Analysis Results	47
2.4.3	Motor and Battery Database Generation	57
3	NONLINEAR DYNAMIC MODEL	61
3.1	Reference Frames and Coordinate Systems	61
3.1.1	Earth-Centered Inertial (ECI) and Earth-Centered-Earth-Fixed (ECEF) frames	62
3.1.2	Vehicle Body-Fixed Frame	64
3.1.3	Wind Frame.....	67
3.1.4	Velocity (Flight Path).....	67
3.1.5	Propulsion or Wing Coordinate Systems	68
3.2	Kinematic Relationships.....	69
3.3	Coordinate Transformations	71
3.4	Angular Velocities and Angular Rates	72
3.5	Equations of motion.....	73
3.6	Equations of motion.....	75
3.7	Forces and Moments.....	76
3.8	Non-Linear Model	78

3.8.1	Pilot Model	78
3.8.2	Controller	80
3.8.3	Plant Model.....	81
3.8.4	Disturbance Model.....	83
3.8.5	Sensor Model	84
4	LINEAR ANALYSIS	85
4.1	Trimming Methodology	86
4.1.1	Trim Results.....	88
4.2	Linearization	90
4.3	Open Loop Stability	91
4.4	Controllability	95
5	CONTROLLER DESIGN	97
5.1	Transition Mode Problem Statement	99
5.2	Control Allocation.....	104
5.3	Linear Quadratic Problem	108
5.4	PID Controller Design.....	111
6	SIMULATION RESULTS	113
6.1	Mission Definition	113
6.2	Linear and Non-Linear Closed-Loop Response.....	113
6.2.1	VTOL Simulation Results	113
6.2.2	Level Flight Simulation Results	115
6.3	Controller Methods' Comparison Results.....	119
6.4	The Effect of Using Separate Signals for Each Motor.....	121
6.5	CFD Resolution Effect on Model Accuracy	122

6.6	Full Mission Simulation Results.....	123
6.7	Vulnerability Analysis Against Parameter Variations.....	127
7	CONCLUSION	129
	REFERENCES	133
	APPENDICES	
A.	Aerodynamic Database.....	149
B.	Linearized System Matrices.....	156
	CURRICULUM VITAE	159

LIST OF TABLES

TABLES

Table 1.1 Platform Types in the Literature	4
Table 1.2 VTOL UAV Types	7
Table 1.3 Tilt-Wing UAVs	7
Table 1.4 Controller Survey of the VTOL UAVs.....	11
Table 2.1 Performance Requirements	17
Table 2.2 Figure of Merit for VTOL FW Aircrafts	18
Table 2.3 Figure of Merit for Planform Types.....	19
Table 2.4 Figure of Merit for Tail Types	19
Table 2.5 Figure of Merit for Wing Position	20
Table 2.6 Design Space Survey for Control Inputs	23
Table 2.7 Aerodynamic Design Parameters.....	31
Table 2.8 Motor specifications	34
Table 2.9 Transition Mode Power Requirements for One Motor	35
Table 2.10 Mass and Inertia Information.....	36
Table 2.11 Transition Flight Mode Power Requirements for One Motor	42
Table 3.1 Nomenclature for Vector Components Resolved in Vehicle Body Coordinates	65
Table 3.2 Aerodynamic Damping Derivatives	77
Table 3.3 Upper and Lower Limits of the Actuators	82
Table 4.1 Inputs Variation During Transition.....	89
Table 5.1 Control Allocation Chart	104
Table 5.2 Controller Gains Determination.....	112
Table 6.1 Performance Results of Each Method.....	122
Table 6.2 Performance Results of Each Method.....	122
Table A.1 Aerodynamic Coefficients for $TWA = 0^\circ$	149
Table A.2 Aerodynamic Coefficients for $TWA = 15^\circ$	150

Table A.3 Aerodynamic Coefficients for TWA = 30°	151
Table A.4 Aerodynamic Coefficients for TWA = 45°	152
Table A.5 Aerodynamic Coefficients for TWA = 60°	153
Table A.6 Aerodynamic Coefficients for TWA = 75°	154
Table A.7 Aerodynamic Coefficients for TWA = 90°	155

LIST OF FIGURES

FIGURES

Figure 2.1. Mission Profile	17
Figure 2.2. Tilting mechanism	21
Figure 2.3. CoM of Tilting Wing and CoM of the aircraft	22
Figure 2.4. Configurations Studied in terms of Control Inputs	22
Figure 2.5. Aerodynamic Characteristics of Competitive Airfoils	28
Figure 2.6. Wing Area and AR Optimization	30
Figure 2.7. Moment Coefficient variation with respect to Angle of Attack	31
Figure 2.8. Propulsion Package Selection Process	33
Figure 2.9. Current study CAD models	35
Figure 2.10. Major Components of the Aircraft and Ground Control Station.....	37
Figure 2.11. Vehicle Body, Wind and Velocity Frames, and Coordinate Systems	38
Figure 2.12. Effective Velocity and Angle of Attack changes during the transition	42
Figure 2.13. Grid Refinement Results for CL and CD.....	48
Figure 2.14. Grid Domain of the study	49
Figure 2.15. CL Variation for Different Flight Conditions	49
Figure 2.16. CD Variation for Different Flight Conditions.....	50
Figure 2.17. Cm Variation for Different Flight Conditions	50
Figure 2.18. Cl Variation for Different Flight Conditions	50
Figure 2.19. Cn Variation for Different Flight Conditions	51
Figure 2.20. Pressure Contours at Different Angles of Attack	52
Figure 2.21. Pressure Contours at Different Sideslip Angles	52
Figure 2.22. Pressure Contours at Different Elevator Angles	53
Figure 2.23. Pressure Contours at Different Aileron Angles.....	54
Figure 2.24. Pressure Contours at Different Tilt Angles	54
Figure 2.25. Vorticity Contours at Different Angles of Attack	55
Figure 2.26. Vorticity Contours at Different Sideslip Angles	55

Figure 2.27. Vorticity Contours at Different Elevator Angles	56
Figure 2.28. Vorticity Contours at Different Aileron Angles	56
Figure 2.29. Vorticity Contours at Different Tilt Angles	57
Figure 2.30. Front Motors Database	57
Figure 2.31. Rear Motors Database	58
Figure 2.32. Front Batteries Discharge Database	58
Figure 2.33. Rear Batteries Discharge Database	59
Figure 3.1. Earth Frames and Coordinate Systems	63
Figure 3.2. Vehicle Body, Wind and Velocity Frames, and Coordinate Systems ..	65
Figure 3.3. Vehicle Reference Coordinate System	66
Figure 3.4. Sign Convention for Aerodynamic Control Inputs	69
Figure 3.5. Orientation Angles Connecting All Frames and Coordinate Systems ..	70
Figure 3.6. Dynamic and Kinematic Relations between inputs and states	75
Figure 3.7. Nonlinear Model	78
Figure 3.8. Pilot Block.....	79
Figure 3.9. Controller Block.....	80
Figure 3.10. Plant Model	81
Figure 3.11. Transient Response of the Actuators	82
Figure 3.12. Transient Response of the Tilting Mechanisms	83
Figure 3.13. Disturbance Model	83
Figure 4.1. Linear Model for Trimming	88
Figure 4.2. Velocity Changes with respect to Tilt-Angle.....	89
Figure 4.3. Impulse Responses of the Aircraft for Forward Flight	93
Figure 4.4. Impulse Responses of the Aircraft During Hover.....	94
Figure 5.1. Controller Architecture without Mixer	97
Figure 5.2. Controller Architectures with Mixer	98
Figure 5.3. Possible Ways of Going from One State to Another	101
Figure 5.4. Total Time change with respect to a and b constants	103
Figure 5.5. Body Velocity u change during transition from 15° to 0°.....	103
Figure 5.6. The Flowchart of the Mixer	108

Figure 6.1. Roll Angle Response of the Aircraft in VTOL mode.....	114
Figure 6.2. Pitch Angle Response of the Aircraft in VTOL mode	114
Figure 6.3. Altitude Response of the Aircraft in VTOL mode	115
Figure 6.4. Altitude Command and Altitude Response of the Aircraft in VTOL Mode	115
Figure 6.5. Roll Command and Roll Angle Response of the Aircraft in Forward Flight Mode.....	116
Figure 6.6. Roll Angle Response of the Aircraft in Forward Flight Mode.....	116
Figure 6.7. Pitch Angle Response of the Aircraft in Forward Flight Mode	116
Figure 6.8. Yaw Command and Yaw Angle Response of the Aircraft in Forward Flight Mode.....	117
Figure 6.9. Yaw Angle Response of the Aircraft in Forward Flight Mode	117
Figure 6.10. Altitude Command and Altitude Response of the Aircraft in Forward Flight Mode.....	118
Figure 6.11. Altitude Response of the Aircraft in Forward Flight Mode	118
Figure 6.12. Tilt-Wing Angle and Battery Consumption Time History during Transition	119
Figure 6.13. Altitude and Axial Velocity Change during Transition.....	119
Figure 6.14. Euler Angles and Vertical Body Velocity Time History during Transition	120
Figure 6.15. Propeller Angular Velocity Changes during Transition	120
Figure 6.16. Elevator and Aileron Deflection during Transition.....	121
Figure 6.17. Altitude Change during Transition.....	122
Figure 6.18. The trajectory of the Aircraft during the Mission.....	123
Figure 6.19. Random Gust Generated by the Disturbance Block.....	124
Figure 6.20. Tilt-Wing Angle and Battery Level Time Histories during the Mission	124
Figure 6.21. Desired and Actual Body Velocities During the Mission	125
Figure 6.22. Roll Command and Roll Angle Histories During the Mission.....	125
Figure 6.23. Yaw Angle History During the Mission.....	125

Figure 6.24. Control Surface Deflection History During the Mission	126
Figure 6.25. Front Motor Angular Velocity Time History During the Mission....	126
Figure 6.26. Rear Motor Angular Velocity Time History During the Mission.....	127
Figure 6.27. Pitch Angle Response of the Aircraft with respect to Several Parameter Changes	128

LIST OF ABBREVIATIONS

ABBREVIATIONS

AR	Aspect ratio
CAD	Computer-aided design
CFD	Computational fluid dynamics
CoM	Center of mass
FWMAVs	Flapping-wing micro air vehicles
MAC	Mean aerodynamic chord
PWM	Pulse-Width Modulation
TWA	Tilt-Wing Angle
UAV	Unmanned aerial vehicle
VTOL	Vertical takeoff and landing

LIST OF SYMBOLS

SYMBOLS

A	Area of the propeller disc
b	Wingspan
\bar{c}	Mean aerodynamic chord
C_D	Drag coefficient
C_{HT}	Horizontal tail volume coefficient
C_L	Lift coefficient
C_l	Rolling Moment coefficient
C_m	Pitching Moment coefficient
C_n	Yawing Moment coefficient
C_X	Axial force coefficient
C_Y	Side force coefficient
C_Z	Vertical force coefficient
h	Geometric altitude
M	Mach number
p	Roll rate
\bar{q}	Dynamic pressure
q	Pitch rate
r	Yaw rate

S	Reference wing area
S_H	Horizontal tail reference area
$\tilde{T}^{(B,W)}$	Transformation matrix from Wind Coordinates to Body Coordinates
T	Thrust
u	The velocity of the body on x-axes
V_{Prop}	Propeller slipstream velocity
v	The velocity of the body on y-axes
V_T	True airspeed
V_{stall}	Stall speed
V_{wing}	Effective velocity vector over the wing
w	The velocity of the body on z-axes
x_w	The distance from CoM to 25% of MAC

Greek Symbols

α	Angle of attack
α_{wing}	The angle of attack of the wing
β	Sideslip angle
Γ	Geometric dihedral angle
δ_a	Aileron deflection
δ_e	Elevator deflection
δ_f	Flap deflection
δ_{TW}	Tilt-wing angle
η_H	The ratio of dynamic pressure at the tail to that of the free stream
θ	Wing twist angle

$\Lambda_{c/4}$ Quarter chord sweep angle

ρ The density of the air

CHAPTER 1

INTRODUCTION

It is crucial to design an air vehicle that is efficient, affordable, reliable, and also capable of serving the needs throughout its lifecycle. In accordance with this target, several air vehicles were designed throughout aviation history in terms of their wing motion. Unmanned air vehicles can be classified into three groups in terms of their wing motion. These are fixed-wing, rotary-wing, and flapping wing[1]. There are advantages and disadvantages to each group. Therefore, one type can become dominant in compliance with the application area with respect to others. While fixed-wing airplanes have a disadvantage about take-off and landing distances, rotary-wing and flapping wing airplanes have difficulties in terms of payload capacity and flying to long distances with respect to fixed-wing airplanes. The primary purpose of this study is to combine the advantages of all three types and reveal a more efficient kind of UAV design.

1.1 Motivation

Since field battles have lost their importance and fights are made against smaller groups in narrower places in recent years, the systems which are human-independent as much as possible are getting more and more required. Moreover, the systems which can be carried easily in hand or on vehicles, available for service as soon as possible, take off and land from everywhere needed would be great for the use.

If these systems are integrated into our national technology, the operational forces will gain a great ability against spontaneous incidents, which have both reconnaissance and attacking features. The more aforementioned forces utilize

technological means and capabilities in steep terrain and climate conditions of the area, the more they prevent loss of expert personnel. Also, the possibility of the success of the ongoing operation will increase.

1.2 Problem Statement

As aviation technology becomes sophisticated, the challenges faced are getting complicated day by day. The development of a robust controller of VTOL systems in the transition phase of the flight has been investigated around the world in recent years[2]. Nevertheless, there are still very few examples in use since there is not a rugged way of designing an optimal controller capable of doing vertical, transitional, and horizontal flights at the same time.

Fixed-wing UAVs are the most used platforms which are providing long endurance and long-range, for which researchers [3] show that a mini fixed-wing UAV has at least two times more of flight endurance compared to a mini helicopter. On the other hand, rotary-wing and flapping wing UAVs, such as helicopters, multi-rotors, and flapping-wing micro air vehicles (FWMAVs), can provide hover capability. However, the high-power requirement is limiting flight time and operation radius. Frequent maintenance is required for helicopters. Additionally, they are difficult and expensive platforms to operate due to their mechanical complexity.

Different types of control and guidance methods are used in the literature for VTOL UAVs, and these methods are varying through flight characteristics and control elements of that aircraft. The necessity of high fidelity dynamic model construction using aerodynamic principles has been observed. This need led us to investigate different types of dynamic models in the literature.

The necessity of the control allocation should not be underestimated. Effective controlled design requires an optimal allocation of the control surfaces. Since we are needed to have high endurance and high range capability aircraft, it is very crucial

to use its optimal energy. During the transition phase, a robust controller with a minimum steady-state error should be studied.

1.3 Literature Survey

1.3.1 Platforms in the Literature

Fixed-wing airplanes are obliged to operate above their stall speeds; thus, they are not able to have the capability of hover, and they have to land on their landing gears or bellies or should land by parachute, which makes it susceptible to mechanical failures and crashes.

Multi-rotors have a simple mechanical design; however, they have high power requirements, which limit their payload capacity. Tail-sitters, tilt-rotors, and tilt-wings are VTOL capable platforms, and they have similar features with helicopters and multi-rotors. Even though tail-sitters are mechanically more straightforward platforms, they are difficult to control, and they are not very successful in rejecting disturbances.

There are quadrotor-fixed wing UAVs, but they have less endurance than tilt-rotor and tilt-wing aircraft since they have vertical rotors in the level flight. Although tilt-rotors have reasonable endurance, they lose so much thrust power in vertical flight since rotors are vertical to the wing in that flight. Because of all these reasons, there is a need for an aircraft type that is aerodynamically efficient and has the advantage of vertical and level flight.

VTOL, hover, level flight, transition flight, payload capacity, endurance, control system simplicity, maintainability can be expected from a UAV platform, according to mission requirements. Table 1.1 shows the comparison of capabilities of different UAV platforms, which provides an insight into their mission profiles. When vertical takeoff/landing or hover is required for a mission, then rotary-wing aircraft, such as helicopters or multi-rotors are most optimal. However, if endurance or range is a

priority, then a fixed-wing type will most likely be preferred. When all of these capabilities are expected from one platform, then a VTOL capable UAVs provides the best solution, as a hybrid platform with some trade-offs in its capabilities.

Table 1.1 Platform Types in the Literature

Capability	Platform Types			
	Multirotor	Helicopter	Airplane	Tilt-Wing, Tilt-Rotor, Quadrotor-FW
VTOL Capacity	+	+	-	+
Aerodynamic Efficiency	-	-	+	+
Weight	+	o	o	o
Endurance	-	-	+	o
Range	-	-	+	+
Durability	-	-	+	+
Maintainability	+	-	o	o
Manufacturability	+	-	+	o
Payload Capacity	-	-	+	+
Stability	-	-	+	+
Control System Complexity	+	o	+	-

Demonstrating both fixed and rotary wing capabilities in one platform is one of the main targets in the UAV design process. Having merits of both fixed-wing and rotary-wing, VTOL capable UAVs make missions, which cannot be achieved by either fixed-wing or rotary-wing UAVs alone, achievable. Such UAV types can fly in harsh terrain and effectively take off and land in predetermined regions without a runway, which provides flexibility to us to operate in any theatre. Thanks to level flight, long-range and endurance flight through efficient flight can be achievable. The versatility of the aircraft will be increased by these capabilities. Additionally, there will be less need for human interaction in launch and recovery. It is also allowing for consistent target tracking, guidance in obstacle-filled terrains with extended flight range, and endurance.

Lately, the area of research for the scientific community and industry is very interested in VTOL capable UAVs. Configurations of these platforms differentiate

by the method they have used in combining the control elements. Even though every type has its advantages and disadvantages, some of them seem more promising for future VTOL capable aircraft.

Within the context of scientific researches about VTOL capable platforms, NASA GL-10 [4] is about 30 kg weight, and it has 2 hours of flight endurance. It flies between 15 and 30 m/s, and its service ceiling is about 5000 ft. It has ten motors on it, of which eight are placed on the main wing, and two are placed on the tail. A conceptual aircraft study [5], named as a convertible tail-sitter UAV, with two counter-rotating propellers, is designed. VertiKUL is developed by Researchers at KuLeuven. It is a quadcopter-tail-sitter flying wing [6] with only VTOL control elements that achieves transition through tilting fuselage. SUAVI [7], which is mainly designed for surveillance, has 17 m/s cruise speed. They have mainly studied the controller and avoided the aerodynamical complexity as much as possible. The whole aircraft, which has four rotors and 4.5 kg take-off weight, is manufactured from carbon fiber. It has symmetry in the pitch axis due to using two tandem wings, which are identically the same and placed sequentially. This symmetry provides to design a less complicated flight controller. However, the aerodynamic performance is affected negatively since the backward wing is affected by the front wing.

QTW-UAV[8], which has 24 kg take-off weight, is designed as four-motored. The wings generate lift while rotors tilted because of the accelerated air by rotor blades in VTOL mode. This feature helps them to have one more input to maneuver the aircraft during the VTOL and transition modes. The AVIGLE [9], which is capable of performing the mission between 0 and 40 m/s velocity range has 10 kg take-off weight. This aircraft, which has a different design from the others, is designed to have two rotors. The moment is balanced by using a small fan blade; that is, we can say that this UAV has three rotors in total. It is made from carbon fiber. This type is considered riskier than the others since the aircraft will become uncontrollable in case of a rotor loss. Another study by Onen et al. [10] performed hover for a tri-copter fixed-wing UAV configuration. Also, another tail-sitter aircraft is developed with a coaxial propulsion system [11], and they have performed hover with this

aircraft. The QUX-02A [12], which has two wings and four rotors, has a 4.2 kg take-off weight, and it is capable of doing missions between 10 and 25 m/s velocity. In another study [13], a tail-sitter configuration with variable pitch propellers is utilized. Stone [14] developed a T-wing tail-sitter UAV with two counter-rotating propellers in 2005.

Another interesting example is TURAC [15], which is a flying wing-tiltrotor with a ducted fan configuration. It has a 4.2 m wingspan, 25 m/s cruise speed, and 47 kg maximum take-off weight with 8 kg payload.

Korea Aerospace Research Institute has designed and manufactured a Tilt-Rotor Aircraft [16] for the Smart UAV development program. For the sake of the program, they built a scaled model and tested it successfully. The aircraft maximum take-off weight is approximately 210 kg with 250 km/h top speed. It has an endurance of 5-6 hours, and its wingspan is about 5 m.

The main difference in these experimental VTOL platform studies is the method of transition used in switching the aircraft between flight modes. A tail-sitter platform tilts its fuselage by control surfaces through stalling the aircraft in transition. A tilt-rotor tilts its fuselage by changing angular positions of rotors and by operating wings at stall conditions in transition maneuvers. A tilt-wing tilts its wings operating in pre-stall conditions, while the fuselage remains parallel to the ground.

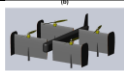

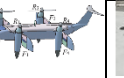


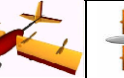
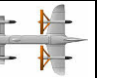
Apart from the Academic Researches, Industrial examples of VTOL capable platforms are also increasing day by day because of the operational requirements. Among them, Xcraft Company's X Plus One [17] is a quadrotor flying wing. Additionally, Arcturus UAV Company's Jump [18] is a quadrotor-fixed wing hybrid, which is a tractor propeller. Comquest Ventures Company's Vertex VTOL [19] and KrossBlade Company's Skyprowler [20] are quadrotor-fixed wing types hybrid with tilt-rotors and retractable rotors, respectively.

Table 1.2 VTOL UAV Types

					
	Tail-sitter	Ducted fan	Tilt-wing	Tilt-rotor	Quadrotor-FW
Control	2	4	3	3	4
Transition	3	4	3	3	4
Hovering capability	1	3	4	3	4
Horizontal flight	3	2	4	4	2
Energy efficiency	4	2	5	5	2
Mechanical complexity	4	2	4	3	5
Payload volume	2	1	4	3	2

Table 1.2 shows that Tilt-Wing Platforms come forward per VTOL UAV types. Therefore, in this study, a Tilt-Wing VTOL capable UAV will be studied. Some examples of Tilt-Wing UAVs can be seen in Table 1.3.

Table 1.3 Tilt-Wing UAVs

							
	SUA VI	NASA GL-10	QTW-UAV	AVIGLE	QUX-02A	HARVee	QTW-UAS FS4
Driven By	Electric Driven	Hybrid Driven	Electric driven	Electric driven	Electric driven	Electric driven	Electric driven
Concept	Quad Tilt Wing	Tilt-Wing	Quad Tilt Wing	Tilt-Wing	Quad Tilt wing	Tilt-Wing	Quad Tilt wing
Made of	Composite	Composite	Composite	Composite	Foam	Wood	Composite
Wing Pos.	Mid wing	High Wing	High Wing	High wing	High Wing	Mid-Wing	High wing
Max. Weight	4.46 kg	30 kg	24 kg	10 kg	4.2 kg	27 lb	30 kg
Rotor Num.	4 Rotors	10 Rotors	4 Rotors	3 Rotors	4 Rotors	2 Rotors	4 Rotors
Fuselage	1 m	1.85 m	1 m	1.85 m	1.1 m	4.5 ft	1.86 m
Wing span	1 m	3.16 m	1 m	2 m	1.38 m	5.7 ft	1.80 m
Chord length	0.25 m	0.25	0.3 m	0.35	0.132 m	N/A	0.30 m
AR	4	12.8		5.7	5.23	N/A	6
Opt./Max. speed	40/60 km/h	22.7/- m/s	-/150 km/h	15/40 m/s	10/25 m/s	15/- m/s	100/150 km/h
Speed Range	0-60 km/h	0-??? m/s	0-150 km/h	0-40 m/s	10-25 m/s	N/A	0-150 km/h
Payload	N/A	2 kg	5 kg	1.5 kg	N/A	N/A	5 kg
Endurance	60 min	120 min	15 min	60 min	N/A	N/A	60 min

The objective of these studies (Table 1.3) was to make an aircraft that has a less complicated flight controller compared to literature designs, although this reduces the aerodynamic performance. It is clearly seen that most of the studies about the

tilt-wing aircraft concept include motors that are symmetrically placed around pitching and rolling axis since it has less control complexity. However, these types do not have that much aerodynamic performance since they use tandem wing instead of pair of the wing and horizontal tail. NASA GL-10 uses a wing and horizontal tail pair, which makes its controller a little bit complex; therefore, it is aerodynamically efficient. The current study aims to investigate a VTOL UAV platform that has both sufficient aerodynamic and controller performance as well.

1.3.2 Control System Architectures in the Literature

Aircrafts, thanks to the flight control system, are able to be stabilized, track guidance commands, reject disturbances, and be robust to the parameter variations and the uncertainties. For the VTOL capable UAVs, the flight control system should perform flight modes switching, which requires switching between different trim conditions [3]. Switching the aircraft from vertical flight mode to forward flight has very complex, highly non-linear dynamics since the trim condition of the aircraft is always changing during the transition. Hence, control system architecture should aim to achieve a successful transition without steady-state error, which means without any altitude change in transition.

There are two different domains related to a control strategy. The first one is tracking action ([21],[22]), which takes place around trim states, and means that control around the states involving continuous feedback with small amplitude actions that result in small amplitude state changes. In this type, the aircraft dynamics can be assumed that it is changing linearly. The desired state trajectory is followed in conventional flight by using tracking control. It is common in these design strategies to linearize the system around a trimmed flight condition and to use a basic steady-state near trim flight kinematic relationships to simplify control law design. If the altitude and the airspeed are needed to be changed or extended, control techniques such as gain scheduling [23] can be used with no change in the control system design strategy.

The second control strategy is maneuvering actions [24], which starts with one trim state and end on another one. This control activity generally involves significant amplitude actions that result in large amplitude state changes. While tracking trim states is a well-known area, maneuvering, which generally has nonlinear dynamics, has many challenges because of highly nonlinear dynamics. For maneuvering actions, gain scheduling has been employed in most of the aircraft. While changing trim states, gain scheduling involves linearization of the system at several operating points and interpolation of the controller gains for the conditions between these operating points. To have a robust closed-loop system and not to affect controllability, this class of controllers typically causes to lean significant limitations on the aircraft's allowable attitude, velocity, and altitude deviations, and it limits the operation points in the flight envelope, where the aircraft's flight dynamics change slowly. However, these controllers are widely used in VTOL capable aircrafts.

In this study, tracking actions will be used to follow guidance commands in any of the flight modes, and maneuvering actions will be utilized in achieving transitions between flight modes. Although human pilots can perform intricate maneuvers, it still falls short of the aircraft's capabilities. Therefore, the flight control system will be in use in all flight modes, from vertical take-off to forward flight. The control system for a Tilt-Wing UAV should be able to control the aircraft within large deviations without having lost the agile maneuverability to benefit from the capabilities of the aircraft.

There are many studies on different types of UAV platforms, designed for combining the desired features of Fixed Wing and Rotary Wing aircraft. Platforms in this category, like tilt-wing, tiltrotor, and tail-sitter, are capable of level flight and VTOL. In literature, there are several types of controllers to have robust control over the vertical and forward flight. Studies in the literature can be summarized as follows;

NASA GL-10 [4] uses an L1 Adaptive Robust control technique to control the aircraft. The flight controller provides closed-loop feedback control utilizing body-axis angular rates and attitudes to control the vehicle. It uses separate PID gains

assigned during forward flight and hover. The settings to control the feedback gains for Hover and Forward Flight are blended linearly during the transition. During hover, the pilot input is mixed to the assigned motor and servo outputs, which correspond to a “Y-copter” multi-rotor configuration. During forward flight, the pilot input is appointed as per the standard RC airplane configuration (aileron, elevator, throttle, and rudder). The scheduled rotation of the wing and tail are set to a 10 second transition period where the mixing is slowly transferred from the Y-copter control (Mode 1) to the wing-borne forward flight control.

SUAVI [25] proposes a hierarchical control system architecture, which has the position and attitude subsystems and uses a dynamic inversion method, with anti-aliasing filters. A 100-hertz hard real-time control loop gives sufficient closed-loop stability to the aircraft. They implemented a Dryden Wind-Gust Model to 6-DoF model to increase the robustness of the PID controller. They also used the LQR controller for the vertical flight. Aircraft deviated from the desired altitude by only 30 cm in vertical flight. Pitch control is made with a thrust difference at VTOL, which means the elevator is not being used during VTOL maneuvers.

Hover capability is essential for VTOL maneuvers. Related with the hover capabilities, a convertible tail-sitter UAV [26], which is a conceptual aircraft study, with two counter-rotating propellers, is designed, and PID controllers are employed for hover demonstration. Another study [27] performed hover for a tri-copter, which was a fixed-wing UAV, by using optimal control techniques. Hover condition for tail-sitter has also been investigated by other researchers such that Matsumoto[28] has used PID controllers with quaternions, and Escareno [29] divided the dynamics into three parts as lateral, longitudinal, and axial dynamics. He has developed separate nonlinear controllers for hover. Lyapunov functions are used by Garcia [30] to control the aircraft during the hover maneuver.

Table 1.4 Controller Survey of the VTOL UAVs

		Control Inputs	Controller Type	System Freq.	Gain Scheduling	Transition Time	Steady State Error	Controller Level	Filter	Disturbance Observer
1		4R	DI PID LQR	100 Hz.	No	40 s	30 cm	2	Anti-aliasing	Yes
2		10R Alrn. Elv.	L1 PID	N/A	Yes	10 s	6.6 m/s	2	N/A	Yes
3		4R	LQI PID	N/A	Yes	N/A	N/A	2	Kalman	Yes
4		3R Flp. Elv.	PID	N/A	Yes	30 s	0.5 m/s	3	No	Yes
5		4R Flp. Elv.	PID	N/A	Yes	100 s	60 m	3	No	No
6		4R	H_{∞}	N/A	Yes	20 s	0	2	Pre-Filter	Yes
7		3R	LQR LQT PID	50 Hz.	N/A	N/A	N/A	N/A	Washout	No
8		2R	TDC* PSO **	50 Hz.	Yes	600 s	Yes	2	Rate Limiter	
11		4R	LADRC PID LQR	300 Hz.	N/A	N/A	N/A	3	N/A	N/A
12		4R	DAC*** DI**** H_{∞} , LQR	50 Hz.	Yes	10 s	No	2	Kalman	Yes
13		4R	LQR	N/A	Yes	10 s	N/A	2	N/A	NNo

SUAVI, NASA GL-10, QTW-UAV, AVIGLE, QUX-02A, FS4 QTW-UAS, HARVee, ONEN's Tricopter, Korean Tilt Rotor, Guclu's Hybrid Air Vehicle, QTW-UAV, RPAS

*Time Delay control

**Particle Swarm Optimization

***Disturbance Accommodation Control

****Dynamic Inversion

VTOL aircrafts mainly deal with the transition maneuvers between level flight and hover, which makes the transition maneuver a primary concern in VTOL aircraft. One of the pioneering studies for VTOL-capable UAVs was T-wing tail-sitter UAV with two counter-rotating propellers, which was started in 2005. Stone ([31],[14]) has designed a flight control system, which includes low-level and mid-level guidance controllers. These controllers were a mixture of LQR and PID controllers. Flight tests [32] proved that successful flights could be performed using these controllers.

Kubo [33] studied a similar but smaller platform with two tails, and simulations showed that using slats and flaps helped the aircraft to perform transitions between level flight and hover in a shorter time by an optimal controller. Hogge [34] designed a platform that is capable of doing agile maneuvers by performing hover and level flight with manual controls. A quick turn maneuver is realized by [35] and [36], after the transition maneuver. Tumble-stall maneuver [37] was applied for achieving transitions by using the dynamic inversion method, which confines doing continuous transition and leaves aircraft vulnerable to disturbances. Wang [38] studied the back-stepping control technique for a coaxial-rotor tail-sitter UAV, and simulations showed that hover, level flight, and transitions could be performed successfully. Knoebel [39] used both back-stepping method and the least-squares based model reference, adaptive controller. In his following research [39], he defined quaternion-based attitude control in transitions by proposing an online system identification method. Aksugur ([40] and [41]) used a propeller-ducted fan hybrid propulsion system and determined force and moment conditions for different flight modes.

VTOL capable UAV studies generally focus on controlling specialized maneuvers. However, these maneuvers are highly dependent on the aircraft's dynamics. A control method that is applicable to real-world flight with a more general approach that works well even under model uncertainties, disturbances is desirable for Tilt-Wing UAVs.

1.4 Research Question and Contributions to the Literature

The main contributions of this study are to build up an approach to the problem of combining the advantages of Fixed-Wing and Rotary-Wing aircrafts in one platform and establish methods for control to improve its versatility by using mode transitions and multi-modes. The aircraft has been designed with combined VTOL and Fixed Wing control elements that increase aerodynamic efficiency. Having VTOL and Fixed Wing modes together, the aircraft is able to be operated in an extended flight envelope from hover to high speeds of level flight. Therefore, the nonlinear model of the aircraft is developed considering pre-stall conditions as well. Also, the utilization of aerodynamic surfaces provides extra benefits in VTOL mode. MATLAB Simulations proved that the aircraft could be operated at close trim conditions in different modes for smooth transitions.

In this study, an aircraft that has no vertical tail or fin has been studied. Active, asymmetric thrust control has been implemented to control the lateral-directional axis of the system. The distributed electric propulsion method has helped to control vertical tailless aircraft since there are much of engine available to have excess power for asymmetric thrust. However, this does not mean that unnecessary motors have been used. In contrast, the distributed propulsion method is beneficial for both VTOL and horizontal flight. In VTOL flight, increasing the number of electric driven engines increases the total efficiency. Additionally, it reduces the risk of failure effects on the control system. In other words, in case one of the engines failed the probability of catastrophic failure is decreasing since there are sufficient numbers of motors to compensate for this failure. In horizontal flight, rear motors with ailerons are employed to control the lateral-directional axis, which means that there are no unused or unnecessary engines on aircraft.

Aerodynamic analysis for a Tilt-Wing aircraft for different tilt angles will have significant contributions since it is not easy to find detailed CFD analysis for transition flight. Pressure distribution, vorticity contours, static aerodynamic coefficients for a conventional tilt-wing aircraft can easily be found in this study.

Smooth transition methods have been investigated for different tilt angles, and the problem has been defined to prevent a transient response. Desired control inputs have been found by using smooth transition methods, which will optimize the energy consumption during the transition. Additionally, the minimum time problem has been examined to optimize the consumed time during the transition.

Standard control methods have been applied to Tilt-Wing UAV to control the aircraft in level flight, hover separately. However, in transition flight, a method has been proposed by exploiting available methods to decrease the deviation from desired states and for a smooth transition. Available control methods have been tailored to suit tilt-wing UAV's characteristics to obtain non-conflicting results for the same guidance objectives.

As a result, the contributions of this research can be summarized as; Designing of Tilt-Wing UAV with integrating VTOL and level flight control elements, developing a non-linear model of Tilt-Wing UAV including pre-stall conditions, Extending conventional aircrafts' flight envelope and increasing versatility of them, designing a control system structure for Tilt-Wing UAV, designing of different flight mode controllers, implementing a transition control technique between different flight modes, providing multi-modes through the utilization of redundant control elements, designing a vertical tailless aircraft, performing the CFD analysis for the transition period.

1.5 Major Objectives

The system, which will be capable of flying for 60 minutes, electric driven and radio-controlled, will have a one km operational radius, 2.5 kg payload capacity, and 15-25 m/s cruise speed. The VTOL UAV, which will practice the take-off and landing using thrust supplied by the electric motors fixed in front of the tilting wing, which is placed vertical to XY plane of the body, will perform the level flight by making the wings parallel to the body after take-off. When demanded, it will be able

to bring the wings to a vertical place and start to hover again. Aircraft will land using the same operation logic with take-off. There will be six electric motors, of which four will be on the wing, and two will be on the horizontal tail. Especially in the transition phase, during which characteristic of the system will change rapidly, the aircraft will be under the control of the autopilot to prevent losing control. Stability coefficients that will be needed while designing the controller have been obtained using a commercial CFD code (FLUENT [42]).

1.6 Outline of the Thesis

Chapter 1 presents an introduction, puts forward the motivation and problem statement, reviews literature, shows the contributions and significant objectives of this research.

Chapter 2 defines design criteria, aerodynamic and mechanical design, and CFD analysis results of the aircraft.

Chapter 3 introduces the non-linear model of VTOL Tilt-Wing UAV by defining reference frames, equations of motion, and block models of aircraft's components.

Chapter 4 tells about the linear analysis of the aircraft by providing the methods, trim conditions, linearization results, open-loop stability, and controllability.

Chapter 5 defines the control system design methodology and details the structure of the controller.

Chapter 6 presents and discusses the results of the flight tests conducted in MATLAB simulation environments.

Chapter 7 concludes the thesis by discussing the advantages and disadvantages of the proposed aircraft and control methods. Additionally, future studies of this work are presented in this section.

CHAPTER 2

AERODYNAMIC DESIGN AND OPTIMIZATION

2.1 Conceptual design

2.1.1 Design Requirements

The Design Performance Requirements of the system are given in Table 2.1.

Table 2.1 Performance Requirements

Requirements	Value
Flight Time (min)	60
Operational Radius (m)	1000
Payload (kg)	2.5
Cruise Speed(m/s)	15-25
Engine Type	Electric Driven
Engine Number	6
Hover	Yes
VTOL	Yes

The aircraft should be capable of performing the mission profile, which is given in Figure 2.1.

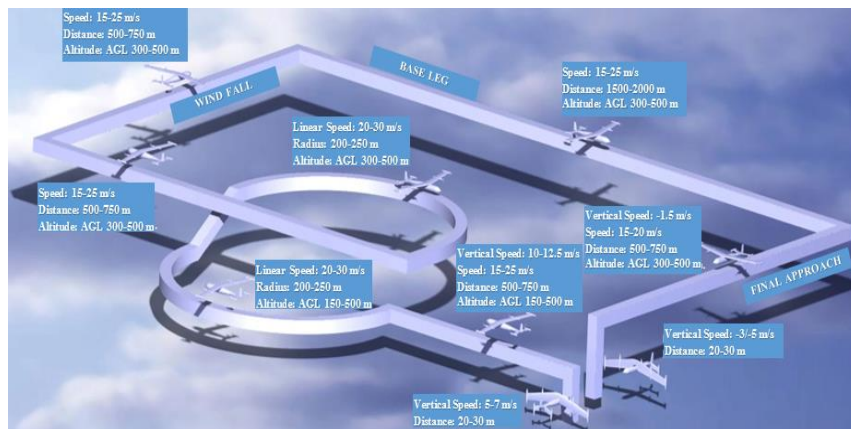


Figure 2.1. Mission Profile






Mission will start on the ground at VTOL mode. The aircraft will climb 10-meter altitude and start to transition flight. The transition flight speed range will be between 0-16 m/s. After the transition phase, aircraft will start to climb. When the desired altitude is achieved, turn maneuvers will be started. After the 360° turn is completed, aircraft will track windfall, base leg and final approach. The aircraft will finish the mission with a transition flight from level flight to vertical flight.

2.1.2 Planform Selection

2.1.2.1 Figures of Merit

VTOL capable aircraft configurations mentioned in Chapter 1 have been evaluated using the figure of merit (Table 2.2). It is seen from the table that the tilt-wing aircraft had the top score. The most important reason to choose the tilt-wing aircraft is that its aerodynamic performance and payload capacity is the best. After having selected the tilt-wing aircraft, configuration selection is performed using several figures of merit.

Table 2.2 Figure of Merit for VTOL FW Aircrafts

					
	Tilt-rotor	Tail-sitter	Quadrotor-FW	Ducted fan	Tilt-wing
Aerodynamic	5	4	2	2	5
Durability	3	5	5	3	5
Flight Time	4	3	2	2	4
Weight	4	5	4	3	4
Payload	3	2	2	1	4
Manufacturability	3	4	5	2	4
Stability	3	2	4	4	3
Control System	2	2	4	4	2
Maintainability	3	4	4	2	3
Total Score	30	31	32	23	34

The first step of the configuration selection is to determine the best aircraft planform type (Table 2.3). Scoring of the Figure of Merits has been performed using the information found in the literature [43]. Conventional aircraft had the top score according to the parameters and weight matrix. In the literature, we can easily see that designers choose conventional type since it has fewer risks than the others.

Table 2.3 Figure of Merit for Planform Types



Figure of Merit	Weight	Conventional	Flying Wing	Canard	Bi-Plane	Blended	Elliptical
Weight	30	3	4	3	2	3	3
Payload	15	4	2	3	3	2	3
Aerodynamics	20	4	3	3	1	4	5
Manufacturing	10	3	2	3	3	3	1
Control System	25	3	1	2	4	3	3
Maintainability	10	3	3	2	3	3	3
TOTAL	100	365	275	295	285	335	350

For the tail types selection, Table 2.4 is used. Conventional horizontal tail types will be used in the aircraft design because of their complexity. Like planform type, in the selection of tail type, risky areas tried to be eliminated.

Table 2.4 Figure of Merit for Tail Types




Figure of Merit	Weight	Boom Mounted or Normal	T-tail	Conventional	U-tail	V-tail	Cruciform
Weight	30	4	3	2	3	4	2
S&C	30	2	4	3	4	3	4
Aerodynamics	30	4	3	4	4	2	3
Manufacturing	10	3	4	3	4	3	3
TOTAL	100	330	340	330	370	270	360

Conventional Tail - simple, easy to manufacture, and usually provides sufficient stability and control with a light structure weight. However, it should be considered that it is possible to lose effectiveness due to wing wake effects.

V-Tail - overcomes the problems mentioned in the Conventional Tail part, and also offers reduced wetted area. Nevertheless, the use of the same control surfaces as an elevator and rudder brings some control actuation complexity. Additionally, moving the control surfaces toward one side to act as a rudder produces an awkward rolling moment in opposition to the desired direction of the turn.

T-Tail – it is usually heavier, necessitating a strong vertical tail to support the horizontal tail structurally. However, it is easy to manufacture and control, and also offers a few remarkable advantages. Locating the horizontal surface upward is decreasing the wing wake effects, increasing its effectiveness, and allowing reduction of its size, hence its weight. Furthermore, the horizontal surfaces high position prevents it from touching the ground during belly landings and guarantees an excellent clearance from the thrower's upper body during hand launch. The disadvantage of the configuration is that landing gear will be needed if this type of tail will be chosen.

Table 2.5 Figure of Merit for Wing Position




Figure of Merit	Weight	Low Wing	High Wing	Middle Wing
Aerodynamics	50	4	3	4
Stability	30	2	4	4
Durability	20	3	4	3
TOTAL	100	320	350	380

Low Wing – Wing is positioned below the centerline of the body. Aircraft may become unstable in the lateral direction. However, it will have better maneuverability.

Middle Wing – This is a conventional type. It has advantages in both maneuverability and stability. The wing is positioned around the centerline of the body. It can have benefits at take-off and landings.

High Wing – Wing is positioned above the centerline of the body. Aircraft will become very stable in the lateral direction. However, it will have worse maneuverability.

In the first iteration of this study, the high wing was chosen. However, a high wing position was precarious for the study because of the distance of the landing gear to the ground. Our landing gear is on the wingtips, and when we tilt the wing, the landing gear should touch to the ground. Also, by choosing the middle wing position, we are eliminating the risk of a complex tilting mechanism.

2.1.2.2 Tilt Wing Mechanism

The tilting mechanism aims to tilt the wings to the desired position. The mechanism is designed as simple as possible to eliminate the risk of failure. The wing tilting mechanism has three parts; servo motor, which will be mounted to the bottom of the fuselage, bearing which will be on both sides of the fuselage, and gear which is mounted on the spar of the middle wing. The gear ratio of the servo and gear will be the same. Servo power will be transferred directly to the gear. As gear tilts, the wing will be tilting. The CAD Model of the tilt-wing mechanism can be seen in Figure 2.2.

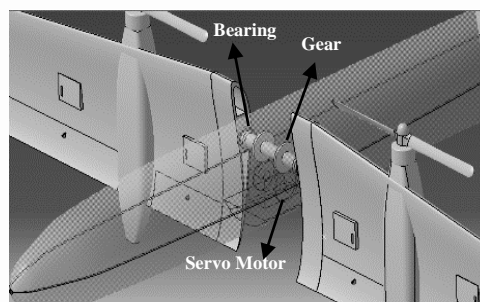


Figure 2.2. Tilting mechanism

As wing tilts around the fuselage, the inertia and center of mass may change. The CoM of the wing is placed at the center of the tilting line, which lines with the middle of the wing spar (Figure 2.3) to hinder the change of the CoM of the aircraft. The same condition is valid for the tail. By using this way, the displacement of CoM of aircraft and inertia matrix during the transition will be zero.

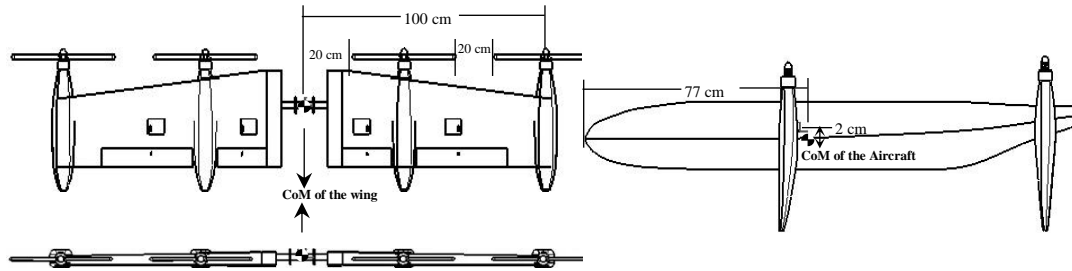


Figure 2.3. CoM of Tilting Wing and CoM of the aircraft

2.1.2.3 Control Inputs

There are three types of control inputs for the tilt-wing aircraft, including rotors, tilting mechanisms, and control surfaces. For the selection of the number of these inputs, the information in the literature is employed. The advantages and disadvantages of the alternatives are introduced. Table 2.6 gives the design space survey for the control inputs, which lead us to choose six rotors, two tilting mechanisms, and three control surfaces.

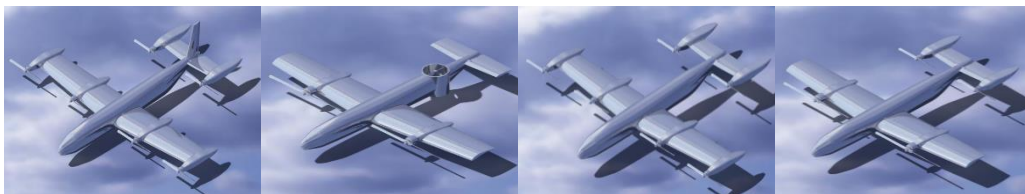


Figure 2.4. Configurations Studied in terms of Control Inputs

As part of the control input selection study, four planforms are studied. Each planform was having different types of control inputs. If the planform were designed with a rudder, the total aircraft weight would be increased by %5, and drag would be

increased by %4. Hence it has been decided that it would be better not to use rudder as part of this study.

One of the alternatives about the VTOL aircraft is using tilt-wing without tilt-tail. Constraints about that planform were in case of losing one engine aircraft would be uncontrollable, the aerodynamic efficiency will be decreased because of the fan duct, and finally, propeller diameter is constrained by the fuselage diameter. The constrained propeller will result from having less thrust than it is needed. Moreover, there will be an additional landing gear need in case of using a ducted balance fan. Another disadvantage is decreasing the structural endurance of the body. Apart from these disadvantages, there is a slight decrease in total aircraft weight because of not using engine nacelle, rear motors, and batteries.

Table 2.6 Design Space Survey for Control Inputs

	Preferable. Good to choose.				
	It can be chosen.				
	A little bit risky.				
	Do not use it.				
	Alternative 1	Alternative 2	Alternative 3	Alternative 4	Remarks
Rotor Number	3	4	6	10	Three rotors should not be chosen; aircraft will be uncontrollable in case of an emergency.
Tilting mechanism number	1	2			Hard to stabilize at hover and transition
Actuator number	Aileron Rudder Elevator	Aileron Elevator	Aileron Rudder	Aileron Only	All actuators should be used in level flight because of the aerodynamic efficiency. However, very much excess motor power in airplane mode lets us not to use a rudder.

NASA GL-10 [4] suggests that utilizing all motors during forward flight is the “dirtiest” form of the aircraft, and it is designed to be operated when inboard motors would be turned off. Only forward motors would be used for forward flight. Hence, only four of the motors will be employed during forward flight. By using this logic, we can increase the endurance of the aircraft. Another issue about the stopped motors is the question of stopping the propeller or using windmilling. This is surveyed in the literature, and it is decided to stop the propeller during forward flight.

2.1.3 Conceptual Design Process

The aircraft design process starts directly with the requirements for the UAV. In tilt-wing aircraft design, the most challenging part is the transition period between vertical flight and forward flight. The main aim of the study is to produce enough aerodynamic force to lift the aircraft in a minimum time interval while aircraft velocity increases. The stall speed should be kept as low as possible to exploit from aerodynamic forces instead of thrust forces during conversion flight, considering this target. Another critical point is the targeted payload capacity, which is determined as 2.5 kg by searching for similar platforms in the literature.

The first step in the conceptual design is weight estimation[44]. By using the empty weight calculation formulas given in [44], the total weight is calculated approximately 10 kg. The CATIA model of aircraft showed us the approximate weights of the structural parts would be about 2 kg. After choosing the motor, our target design weight is 9.5 kg. Having determined that the target weight is 9.5 kg, the airfoil selection is performed. Since the estimated maximum Reynolds Number is about 500,000 and flight velocity is not too high, it is frequently aimed to select an airfoil that has higher L/D ratio. However, while passing through transition flight to level flight, which is the most demanding part of the flight, a high maximum lift coefficient will be needed. So beside L/D ratio, the maximum lift coefficient is also a parameter in the selection process of the airfoil. Different airfoils were analyzed at different Reynolds Numbers via using XFLR5 [45] program. The most suitable airfoil which satisfies the requirements was S1223 in the airfoil family at determined Reynolds number interval. The S1223 airfoil was selected due to its high lift coefficient at stall speed. Usually, low drag and high L/D ratio take precedence, but in our case, we should have stall speed as low as possible to eliminate the risk of the transition phase.

[44] suggests that for similar aircraft, fuselage length should be around 2 meters for the initial assumption. After longitudinal stability analysis performed, it was concluded that the fuselage length of 1.8 m could give sufficient pitch control power.

Lower fuselage length has been selected to decrease the drag effect of the fuselage. Fuselage equivalent diameter has been calculated as 0.2 m using relation given in [44].

2.2 Preliminary Design

Numerous trade studies were performed using software simulations and models to develop the optimum sizing for all components of the aircraft. The main design objectives are to minimize the stall speed, minimize empty weight, and maximize endurance.

2.2.1 Design Methodology

The preliminary design was developed through an iterative and collaborative process that required the input of numerous disciplines. The critical components in the preliminary design phase and their corresponding design requirements are described as follows:

2.2.1.1 Wing Design Methodology

Wing planform area (S): The wing area produces the lift required to support the aircraft payload. The stall speed constrains the wing area at transition flight. As a driving factor in the minimum stall speed, the wing area was optimized to reduce stall speed and aircraft weight.

Aspect Ratio (AR): High AR wings reduce induced drag, offering better transition and cruise performance than low AR wings. As a function of the wing chord, c , and wingspan, b , the AR of the wing largely determines, total lift and drag of the aircraft.

Airfoil: An open-source airfoil is employed to operate efficiently at low Reynolds numbers. The average Reynolds number for this airfoil to operate is $Re = 500,000$.

The airfoil is chosen to generate the required lift at transition and then optimized for (L/D) *cruise* to improve lifting efficiency and minimize the power required at cruise.

2.2.1.2 Tail Design Methodology

Raymer [44] stated that the Horizontal Tail Volume Coefficient, c_{HT} , which is given in Eq. 1 should be $c_{HT} = 0.5$ for homebuilt aircraft.

$$c_{HT} = \frac{L_{HT}S_{HT}}{\bar{c}_w S_w} \quad (1)$$

For the vertical stabilization, the Vertical Tail Volume Coefficient, c_{VT} , should be about $c_{VT} = 0.05$, according to Raymer [44]. However, for this study, it has been decided not to use a vertical stabilizer.

$$c_{VT} = \frac{L_{VT}S_{VT}}{b_w S_w} \quad (2)$$

Static Margin is an indicator of the static stability, which should be greater than zero to have a statically stable aircraft. Also, we can find the static margin by looking at the relation between c_{m_α} and c_{L_α} .

$$c_{m_\alpha} = \left\{ \frac{x_{cg}}{\bar{c}} - \frac{x_{NP}}{\bar{c}} \right\} c_{L_\alpha} \quad (3)$$

where $\left\{ \frac{x_{cg}}{\bar{c}} - \frac{x_{NP}}{\bar{c}} \right\}$ refers to the static margin.

2.2.1.3 Propulsion System Selection Methodology

The motor, propeller, and battery pack: The components were selected to meet the performance goals of the aircraft while minimizing the overall package weight. Two different configurations have been studied to see the effect of the motor number on the whole aircraft. One of them is a four-motored, which has two bigger motors on the wing and two smaller motors on the tail. The other configuration is equipped

with six motors, of which four are on the wing, and two are on the tail. The second configuration was chosen due to smaller overall weight and less energy consumption.

Motor Selection: A larger motor has increased power, increasing flight speed and payload capabilities, but weighs more, increasing the empty weight and thus the total aircraft weight.

Propeller Selection: A large diameter propeller spinning at slow speeds produces similar thrust to a small diameter propeller spinning at fast speeds. A large pitch-to-diameter ratio is most efficient at high airspeeds, and a small pitch-to-diameter propeller is most efficient at lower airspeeds.

Battery Selection: Lower capacity batteries are lighter and help produce greater RPM and voltage, but higher capacity batteries can store more energy and are able to endure higher current draws. Also, more cells have more power, allowing the aircraft to fly faster or with a heavier payload.

2.2.2 Design Trade Studies

2.2.2.1 Airfoil Selection

Since the estimated maximum Reynolds Number is about 500,000 and flight velocity is not high much, it is aimed to select an airfoil that has a high L/D ratio. However, while passing through transition flight to level flight, which is the most demanding part of our flight, we will need a high maximum lift coefficient. So beside L/D ratio, the maximum lift coefficient is also a parameter in choosing an airfoil. Different airfoils are analyzed at different Reynolds Numbers via using the XFLR5 program. The most suitable airfoil which satisfies the requirements was S1223 in the airfoil family at determined Reynolds number interval. Lift and drag coefficients and L/D ratios calculated at various Reynolds numbers and angle of attacks are given in Figure 2.5. A comparison of simulated coefficients was made using XFLR5 for several airfoils; the best are shown in Figure 2.5. The S1223 airfoil was selected due

to its high lift coefficient at stall speed. Usually, priority is low drag and high L/D ratio, but in our case, we should have stall speed as low as possible to eliminate the risk of the transition phase.

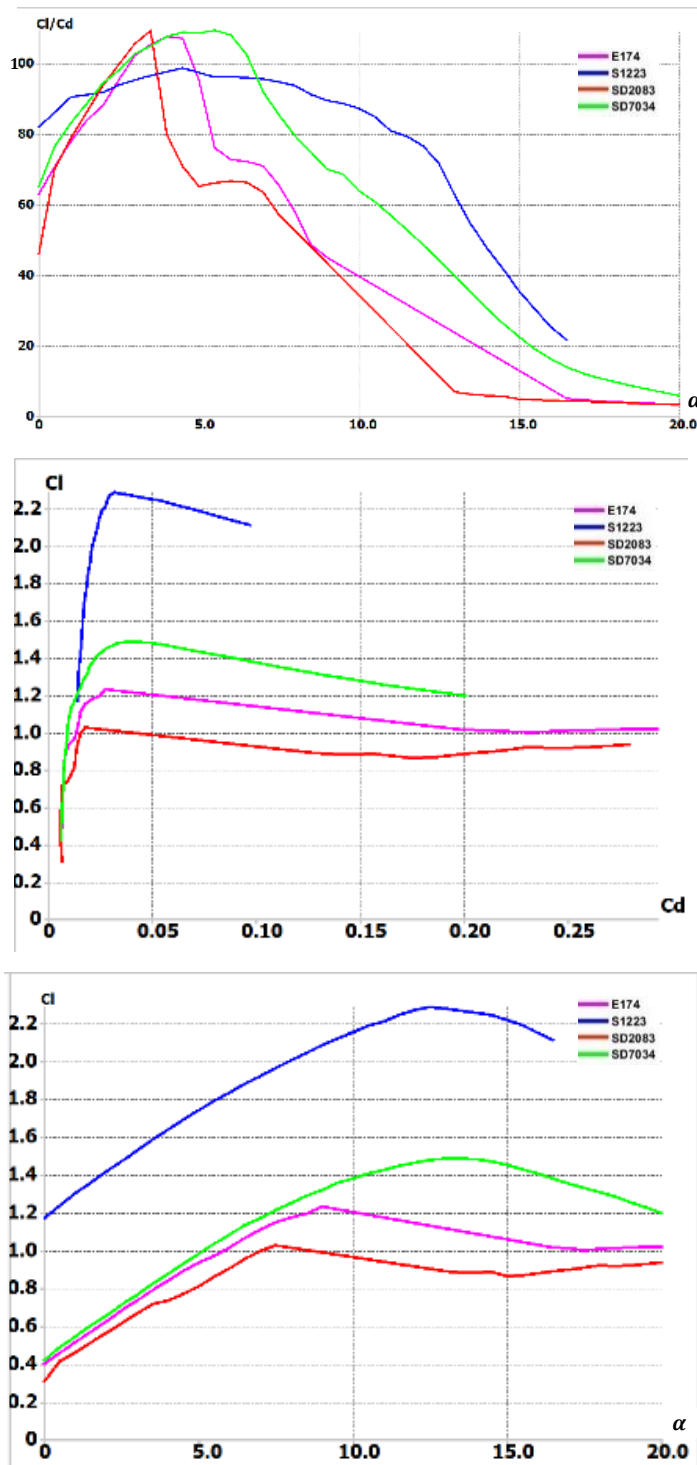


Figure 2.5. Aerodynamic Characteristics of Competitive Airfoils

For the horizontal stabilizer, there are four main options: thin or thick, symmetric, or semi-symmetric airfoils. The thickness of the airfoil determines its drag and lift characteristics. Thicker airfoil could produce more lift but also more drag. Because the stabilizer's purpose is to provide moments only, a thin airfoil was chosen due to its relatively low drag. In contrast, a relatively small lift force was compensated by designing a slightly longer arm.

Symmetric airfoil is commonly used in UAV's, gliders, and light aircraft, providing the vehicle more stability and identical pitch moment for both positive and negative angles of the stabilizer. On the other hand, a semi-symmetric foil could theoretically achieve a slightly higher total lift coefficient for the whole airplane, allowing the vehicle to reach a higher pitch-up moment. Also, a semi-symmetric foil-based wing is easier to manufacture.

Because the symmetric airfoil adds adequate stability, and possible lift addition from the horizontal stabilizer would be negligible due to its relatively small surface area in comparison to the main wing surface area, it was decided to use the NACA 0009 airfoil.

2.2.2.2 Wing Geometry

A trade study determining the effect of variations in AR , b , and S on L/D ratio was performed. The results of this trade study are shown in Figure 2.6, which presents the L/D vs. Wing Span.

The optimal wing geometry minimizes drag while still meeting the lift-off requirement. Studies showed that increasing the wing area decreases V_{stall} . However, this condition is increasing total drag by increasing aircraft dimensions and structural weight. Furthermore, increasing AR also decreases V_{stall} however, increasing the structural weight of the wing, which is fatal for the tilting spars. A limitation on wingspan is employed due to eliminating structural failures of the tilting spar. AR is limited between 5 and 7 to have logical results. The highest scoring wing

configuration has an AR of 6.95 and a wing area of 0.575 m^2 due to the wingspan limitation. The maximum (L/D) is positioned at almost the cruise flight α . This allows for relatively low drag in all phases of flight.

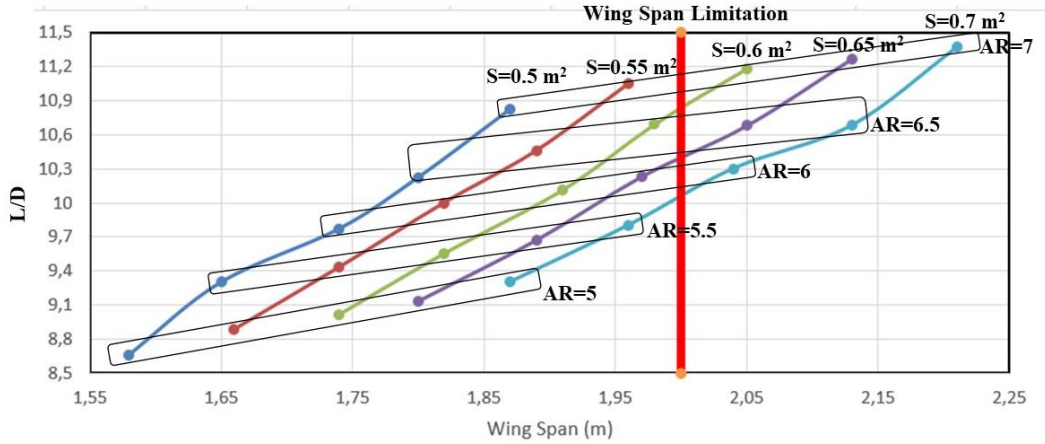


Figure 2.6. Wing Area and AR Optimization

2.2.2.3 Tail Geometry

[44] suggests that for an aircraft which has the design features like in this study " c_{HT} " should be around 0.5; however, the analysis showed that a small tail volume coefficient would not be enough to compensate for the moment which is generated by a high lift producer wing.

Horizontal Tail Volume Coefficient:

$$c_{HT} = \frac{L_{HT} S_{HT}}{\bar{c}_w S_w} = \frac{0.82 * 0.13}{0.29 * 0.575} = 0.61 \quad (4)$$

Static Margin can be calculated as 10% using Eq. 5, which means that the CoM of the aircraft is 3 cm forward from the neutral point.

$$\left\{ \frac{x_{cg}}{\bar{c}} - \frac{x_{NP}}{\bar{c}} \right\} = \left\{ \frac{0.085 - 0.115}{0.291} \right\} = -0.103 \quad (5)$$

As it can be seen from Figure 2.7, that wing and wing-body pair are highly unstable, and they have an extreme pitch-up characteristic. However, thanks to the tail with a high volume coefficient, we are able to compensate for these unstable features. As a result of the initial assessment, we can say that our aircraft is statically stable.

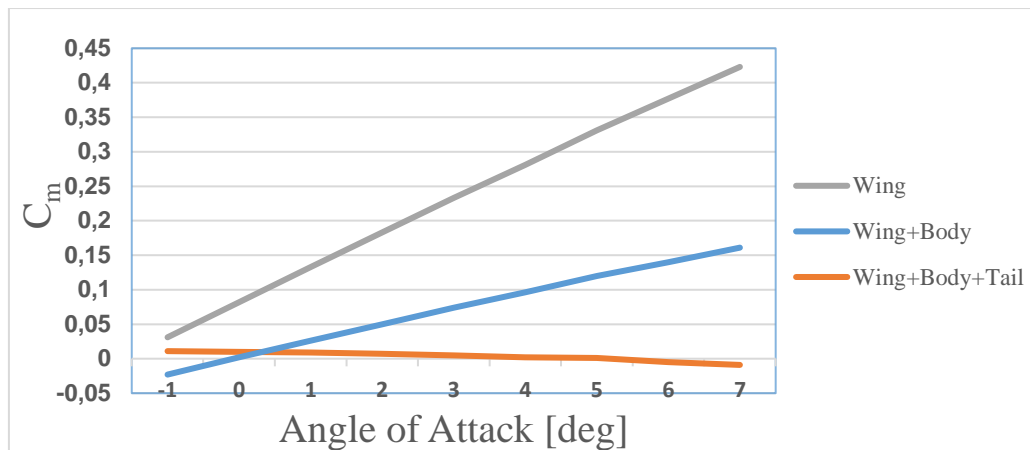


Figure 2.7. Moment Coefficient variation with respect to Angle of Attack

2.2.2.4 Design Parameters

Design Parameters found using [44] are evolved via using XFLR5 and ANSYS Fluent v.18 programs. It is being considered that the aerodynamic design parameters should be as given in Table 2.7 to fly safely in level flight according to the last analysis results.

Table 2.7 Aerodynamic Design Parameters

Wing Span	2 m	Wing Airfoil	S1223
Wing Area	0.575 m ²	Horizontal Tail Airfoil	NACA 0009
Length	1.8 m	Cruise True Airspeed	19.57 m/s
Mass	9.5 kg	C_L at Cruise	0.76
Wing Loading	16.52 kg/m ²	C_D	0.089
MAC	0.291 m	C_L/C_D	8.53
c_{root}	0.33 m	Aspect Ratio	6.957
c_{tip}	0.23 m	Taper Ratio	0.696

2.2.2.5 Propulsion System Selection

A common way to characterize the flight performance of model aircraft is through power loading or the propulsion package's instantaneous power output divided by the total weight of the plane. Electric driven UAVs should have a power loading of more than 300 W/kg [46] to have the capability of the vertical flight. For an initial

search of power components, a target power loading of 300 W/kg was chosen. 300 W/kg was used as an initial assumption based on previous experience with Li-Po batteries until further trade studies could fully optimize the propulsion package. Since our airframe was expected to weigh 9.5 kg, the initial power package selection was supposed to have a power output of approximately 2700 W. Additional assumptions for propulsion system weight were based on the literature survey [44] and other model airplanes. Namely that the propulsion system would be 40% of total aircraft weight or 3.6 kg, and that the battery pack would be 50% of the propulsion package weight or 1.8 kilograms.

The distributed electric propulsion concept is put forward by [47], which shows that increasing the number of propeller results in an increase of power to weight ratio. This phenomenon provides airflow, which flows all over the wing and tail during even hover conditions. This condition gives us an additional aerodynamic power to control the aircraft. A propeller which is covering all over the wing and tail was chosen to have enough propeller slipstream on the wing during the hover and transition phase (Figure 2.8). The propulsion system gives us enough power to stabilize the aircraft in the yaw axis in transition and forward flight; therefore, the vertical stabilizer is not used in the design.

The propulsion system was chosen to maximize the endurance and range of the aircraft while reducing weight. The following steps are performed To start the selection process; Maximum thrust need is determined as 15 kg in total since we aimed to have at least 1.5 thrust to weight ratio of which the forward motors should provide most of them. The center of mass is placed using the standard stability considerations; therefore, the CoM of the aircraft is very close to the thrust application point of the forward motors (Figure 2.8). On the other hand, the distance ratio of the front and rear motors are about eight; therefore, the thrust provided by forward engines should be approximately eight times greater than rear motors.

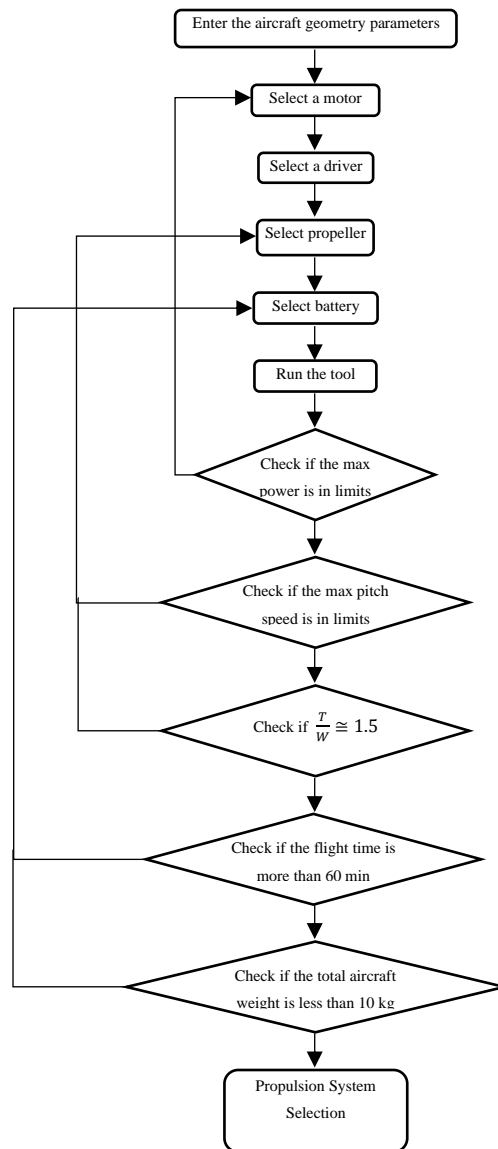


Figure 2.8. Propulsion Package Selection Process

Neu-Motors e-Calc motor and battery package selection tool [48] was used to determine the motor, battery, and propeller pairs accurately. This tool takes the total aircraft weight, the number of motors, wing area, drag coefficient, cross-sectional area, motor type, battery, driver, and propeller as inputs. The airframe weight was calculated as 2 kg, and the target payload was 2.5 kg, and it is estimated that electronic components would weigh about 1 kg. Therefore, total aircraft weight without motor, battery, and propeller is assumed to be 5500 grams. The variables of this selection method are motor type, battery type, driver, and propeller. The

propulsion system selection process is as given in Figure 2.8, where the tool refers to Neu-Motors e-Calc tool, maximum power refers to the power capacity of the chosen battery pack, pitch speed refers to the speed at which the propeller is most efficient.

Table 2.8 Motor specifications

	Forward Motors	Rear Motors
Motor	NeuMotors 1112/6D(1092)	NeuMotors 1902/4Y(1000)
Controller	CC Phoenix Edge 130	CC Phoenix Edge 75
Battery Cell	LiPo 450 mAh-20/30C 6X24	LiPo 1200 mAh-20/30C 3X4
Propeller	APC Electric E 14X16	APC Electric E 8X10
Weight (Each Pack)	748 grams	460 grams
Shaft Power	363.9 W	122.6 W

Several motors, battery, driver, and propeller combinations were analyzed. The propeller diameter was chosen in each iteration again, considering the wing semi span. Since there is a target to cover the wing with propeller slipstream, the diameter of the propeller should be around 15 inches to cover a reasonable area over the wing. As a result of the iterative selection process, it is chosen to use the motor pairs, which are given in Table 2.8.

The thrusts generated by forward and rear motors are different. Main thrust generators are forward motors, and the rear motors are used for moment balancing. During the forward flight, only forward motors will be used since the horizontal stabilizer will be active in forward flight to balance the pitch moment. The rear motors can also be used in forward flight if the endurance is wanted to be increased. The rear motors, since they are placed a little above from forward engines, are set with an angle of -3° with respect to the body frame to pass the thrust line through the center of gravity, which eliminates the motor pitching moment during forward flight. This condition is also required for balancing the moment with elevators since they have symmetrical airfoils.

Table 2.9 Transition Mode Power Requirements for One Motor

Horizontal Velocity (u) (m/s)	Throttle Level (Front)	Throttle Level (Rear)	δ_{TW} [°]	α [°]	Motor Power (W)	Current(A)
0	85%	63%	90	0	276	12.8
1.21	83%	56%	75	8.609	250	11.6
3.19	77%	53%	60	18.1	225.1	10.4
5.41	69%	45%	45	20.3	242	11.2
6.82	58%	0%	30	17.27	250	11.6
9.79	47%	0%	15	10.798	45.5	2.1
16.47	42%	0%	0	0	21.2	1

Longitudinal control of the aircraft mainly depends on the pitch control of the plane. Pitch control power can be generated either by the thrust difference between forward and rear motors or by changing the elevator deflection angle. From Table 2.9, it can be clearly seen that as the horizontal velocity increases, pitch control by PWM difference diminishes since the control power of the horizontal stabilizer is coming forward. Another remarkable result that can be seen from Table 2.9 is that the throttle level of the rear motors is dependent purely on the forward motor throttle level. The high-level controller decides the rear motor throttle level to stabilize the pitching moment coming from the forward engines during vertical and transition flight mode. Table 2.9 has been prepared under the trim conditions data, which is obtained from MATLAB/Simulink/Linear Analysis Toolbox.

2.3 Final Aircraft

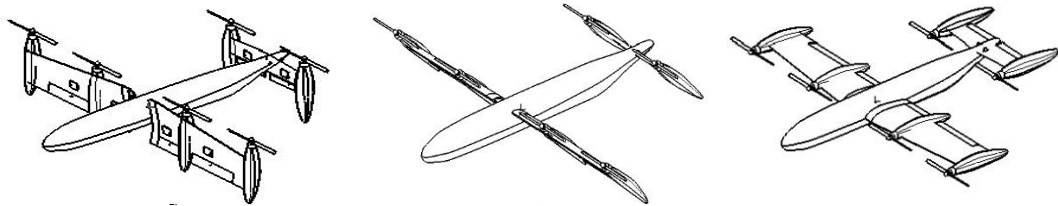


Figure 2.9. Current study CAD models

As a result of the preliminary design analysis, the final aerodynamic design has been delivered, which can be seen in Figure 2.9.

Weight and Mass Information has been taken from the CATIA Model and can be seen in Table 2.10.

Table 2.10 Mass and Inertia Information

Component	Mass[kg]	G _x [mm]	G _y [mm]	G _z [mm]	I _{xx} [kg.m ²]	I _{yy} [kg.m ²]	I _{zz} [kg.m ²]
Fuselage_Main	0.484	-68.638	-0.477	28.175	0.003	0.089	0.088
Fuselage_Payload	2.513	718.24	7.77E-14	31.35	1.01E-04	1.01E-04	1.01E-04
Fuselage_Gear	0.028	22.24	-7.59E-15	60.35	3.63E-05	1.27E-05	3.63E-05
Wing_Middle	0.266	26.289	0.0003	5.498	0.005	0.002	0.004
Wing_Right	0.33	29.485	482.645	31.788	0.016	0.001	0.015
Wing_Right_Aileron	0.047	35.246	498.379	183.138	0.002	1.62E-05	0.002
Wing_Left	0.33	29.207	-482.906	31.493	0.016	0.001	0.015
Wing_Left_Aileron	0.047	34.95	-498.625	182.842	0.002	1.62E-05	0.002
Engine_1_House	0.07	34.276	874.993	77.64	8.52E-04	8.31E-04	9.09E-05
Engine_1_Main	0.315	29.519	874.996	-140.499	7.97E-05	7.97E-05	9.50E-05
Engine_1_Battery	0.448	16.26	880.996	101.363	1.20E-04	7.47E-05	7.47E-05
Engine_2_House	0.07	34.311	399.995	78.803	8.51E-04	8.30E-04	9.09E-05
Engine_2_Main	0.315	29.519	399.996	-140.499	7.97E-05	7.97E-05	9.50E-05
Engine_2_Battery	0.448	11.26	399.996	36.363	1.20E-04	7.47E-05	7.47E-05
Engine_3_House	0.07	34.015	-400.201	77.87	8.52E-04	8.31E-04	9.09E-05
Engine_3_Main	0.315	29.24	-400.2	-140.794	7.97E-05	7.97E-05	9.50E-05
Engine_3_Battery	0.448	10.981	-400.2	36.068	1.20E-04	7.47E-05	7.47E-05
Engine_4_House	0.07	34.042	-875.203	78.629	8.52E-04	8.31E-04	9.09E-05
Engine_4_Main	0.315	29.24	-875.2	-140.794	7.97E-05	7.97E-05	9.50E-05
Engine_4_Battery	0.448	15.981	-881.2	101.068	1.20E-04	7.47E-05	7.47E-05
Tail_Main	0.116	-895.02	0.021	-14.499	0.004	1.31E-04	0.004
Tail_Elevator	0.035	-895.459	-0.002	69.619	8.90E-04	5.77E-06	8.84E-04
Engine_5_House	0.074	-897.495	323.051	51.25	9.30E-04	8.94E-04	1.17E-04
Engine_5_Main	0.315	-896.26	325	-159.194	7.97E-05	7.97E-05	9.50E-05
Engine_5_Battery	0.512	-899.343	325	11.145	8.53E-05	1.37E-04	8.53E-05
Engine_6_House	0.074	-895.029	-323.051	51.229	9.30E-04	8.94E-04	1.17E-04
Engine_6_Main	0.315	-896.26	-325	-159.194	7.97E-05	7.97E-05	9.50E-05
Engine_6_Battery	0.512	-899.115	-325	11.139	8.53E-05	1.37E-04	8.53E-05
Overall Aircraft	9.464	-0.00013	-0.07	0.00022	2.041	3.15	5.037

The major components of the aircraft are illustrated in Figure 2.10. The tilting mechanism and batteries are already mentioned in Sections 2.1.2.2 and 2.2.2.5. Additionally, there will be separate batteries for each motor to minimize energy loss due to long cables. Futaba S3003 servo actuators will be employed for aileron and elevator actuators. The payload is considered to be a camera with approximately 2.5 kg weight. An RF telemetry with 433 MHz frequency and 100 mW RF Power is decided to be used. IMU will be used for accelerometer, and gyroscope data need. The accelerometer range will be between -8 and 8 m/s², and the gyroscope will be

capable of measuring -100 to 100 deg/s. 200 kHz output rate will be enough for IMU. GPS with 3 m resolution and a 10 Hz output rate will be used for guidance commands, which will be given by the pilot manually. The electronic speed controller will be used for motor RPM control.

There will be a ground control station that is responsible for sending the commands to the aircraft and receive data sent by payload (camera), GPS, and the controller. The pilot will give the guidance commands manually, which means that the ground control station is a crucial factor to fly safely. Note that pilot will not control the aircraft, he will give commands, and the aircraft will be under the control of the controller.

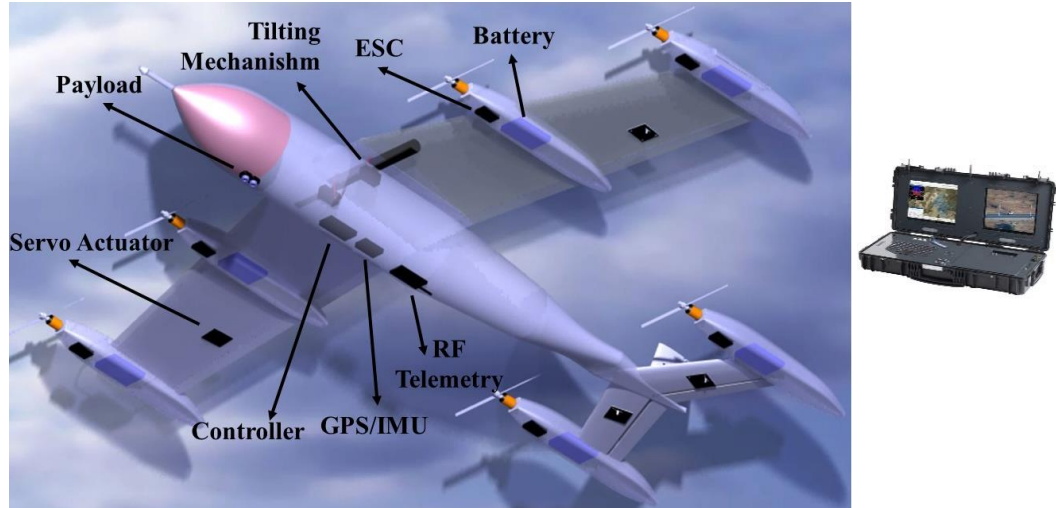


Figure 2.10. Major Components of the Aircraft and Ground Control Station

2.4 Aerodynamic Analysis

The vehicle body-fixed frame \mathcal{F}_B has its origin B located at the instantaneous CoM of the air vehicle, as shown in Figure 2.11. As the vehicle moves through the air, it experiences a relative wind over its body, which gives rise to aerodynamic forces. Introducing the wind frame $\mathcal{F}_W\{W; \hat{i}_W, \hat{j}_W, \hat{k}_W\}$, having its origin W coinciding with point B (vehicle CoM), the X_W -axis of its preferred wind coordinate system is also depicted in Figure 2.11. The wind frame \mathcal{F}_W , having origin W coinciding with B ,

relates $\vec{v}_{B/W}^E$ to the body frame \mathcal{F}_B . An additional frame is introduced called the velocity frame $\mathcal{F}_V\{\hat{i}_V, \hat{j}_V, \hat{k}_V\}$ (also known as the flight path frame), having origin V coinciding with B , and the X_V the coordinate axis of its preferred velocity coordinate system lies along the geographic velocity vector $\vec{v}_{B/E}^E$.

The velocity vector of the CoM with respect to the air can be expressed in terms of the geographic velocity vector of the CoM with respect to the earth and the velocity vector of the wind with respect to earth, as:

$$\vec{v}_{B/W}^E = \vec{v}_{B/E}^E - \vec{v}_{W/E}^E \quad (6)$$

Resolving this equation in vehicle body coordinates,

$$\check{T}^{(B,W)}\{\vec{v}_{B/W}^E\}^{(W)} = \check{T}^{(B,E)}\{\vec{v}_{B/E}^E\}^{(E)} - \check{T}^{(B,E)}\{\vec{v}_{W/E}^E\}^{(E)} = \{\vec{v}_{B/E}^E\}^{(B)} - \{\vec{v}_{W/E}^E\}^{(B)} \quad (7)$$

These velocities can be demonstrated in vector form as,

$$\{\vec{v}_{B/W}^E\}^{(W)} = \begin{bmatrix} V_T \\ 0 \\ 0 \end{bmatrix}, \quad \{\vec{v}_{B/E}^E\}^{(B)} = \begin{bmatrix} u \\ v \\ w \end{bmatrix}, \quad \{\vec{v}_{W/E}^E\}^{(B)} = \begin{bmatrix} u_W \\ v_W \\ w_W \end{bmatrix} \quad (8)$$

and V_T is the true airspeed, given by the magnitude of the velocity vector $\vec{v}_{B/W}^E$ of the CoM with respect to the air mass ($|\vec{v}_{B/W}^E|$), such that;

$$V_T = \sqrt{(u - u_W)^2 + (v - v_W)^2 + (w - w_W)^2} \quad (9)$$

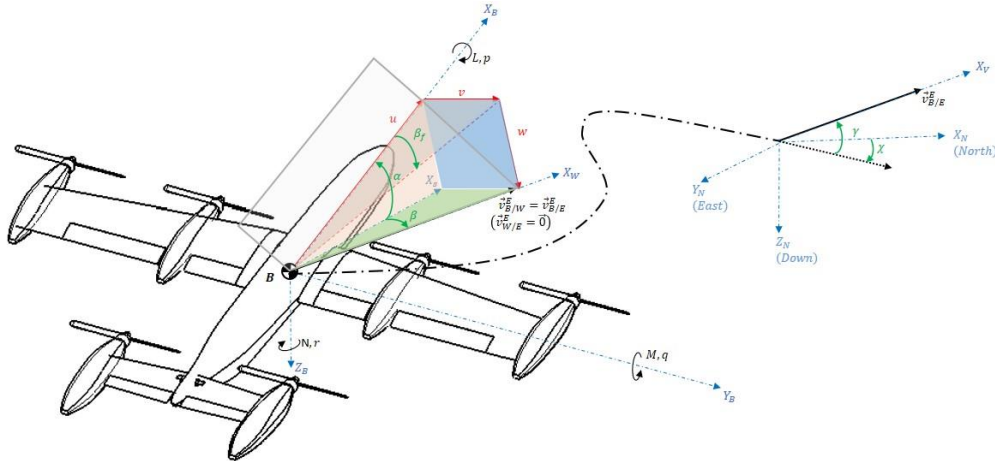


Figure 2.11. Vehicle Body, Wind and Velocity Frames, and Coordinate Systems

For VTOL and Transition mode, there will be an additional airspeed that is coming from the propeller slipstream. The propeller slipstream velocity in forward flight is assumed to be negligible. This extra airspeed should be added to total airspeed for related flight phases. Since the additional speed will be in the only the opposite direction of the engine, we can add it in the propulsion coordinates (wing coordinates) as;

$$\{\vec{v}_{B/W}^E\}^{(P(F))} = \begin{bmatrix} -V_{Prop} \\ 0 \\ 0 \end{bmatrix} \quad (10)$$

We can transform it into the body coordinates as;

$$\{\vec{v}_{Wing/W}^E\}^{(B)} = \begin{bmatrix} u_W \\ v_W \\ w_W \end{bmatrix} + \begin{bmatrix} c(\delta_{T(F)}) & 0 & s(\delta_{T(F)}) \\ 0 & 1 & 0 \\ -s(\delta_{T(F)}) & 0 & c(\delta_{T(F)}) \end{bmatrix} \begin{bmatrix} -V_{Prop} \\ 0 \\ 0 \end{bmatrix} = \begin{bmatrix} u_W - c(\delta_{T(F)})V_{Prop} \\ v_W \\ w_W + s(\delta_{T(F)})V_{Prop} \end{bmatrix} \quad (11)$$

Dynamic pressure, denoted by \bar{q} , is defined as a function of true airspeed V_T and atmospheric air density ρ , as follows:

$$\bar{q} = \frac{1}{2} \rho V_T^2 \quad (12)$$

Using the two coordinate transformation matrices for $\check{T}^{(B,W)}$ derived separately in terms of angle of attack and sideslip angles (α and β), substitution in Eq. 9 yields the components of $\vec{v}_{B/W}^E$ in body coordinates as;

$$V_T c(\alpha) c(\beta) = u - u_W + c(\delta_{T(FR)}) V_{Prop} \quad (13)$$

$$V_T s(\beta) = v - v_W \quad (14)$$

$$V_T s(\alpha) c(\beta) = w - w_W - s(\delta_{T(FR)}) V_{Prop} \quad (15)$$

The respective definitions for Cartesian (wind) incidence angles are now derived from these two sets of relations, in terms of the body-axes components of $\vec{v}_{B/E}^E$ and $\vec{v}_{W/E}^E$, together with the relative wind-axis component (true airspeed V_T) of $\vec{v}_{B/W}^E$, obtaining the trigonometric relationships;

$$\alpha = \tan^{-1} \left(\frac{w - w_W}{u - u_W} \right) \quad \alpha_{wing} = \tan^{-1} \left(\frac{w - w_W - s(\delta_{T(FR)})V_{Prop}}{u - u_W + c(\delta_{T(FR)})V_{Prop}} \right) \quad (16)$$

$$\beta = \sin^{-1} \left(\frac{v - v_W}{V_T} \right) \quad (17)$$

$$\beta_f = \tan^{-1} \left(\frac{v - v_W}{u - u_W + c(\delta_{T(FR)})V_{Prop}} \right) \quad (18)$$

Here, β_f is the so-called flank angle, which is the projection of the sideslip angle β onto the body coordinates. Note that there is virtually no difference between β and β_f at low α , but the correct definition of β must be applied for very high α .

Mathematical manipulations can be performed on these expressions to derive the following trigonometric relationships for converting between all incidence/wind angles,

$$\alpha = \tan^{-1}(c_\varphi t_{\alpha_T}) \quad (19)$$

$$\beta = \sin^{-1}(s_\varphi s_{\alpha_T}) = \tan^{-1}(c_\alpha t_{\beta_f}) \quad (20)$$

$$\beta_f = \tan^{-1}(s_\varphi t_{\alpha_T}) \quad (21)$$

Lift and drag are defined to be the components of the aerodynamic force in the perpendicular and parallel to flow directions, respectively. Therefore, lift (L), drag (D) and crosswind force (C) are directly measured in the wind coordinate system. Using body-axes components of the aerodynamic force vector $\{\vec{f}_\alpha\}^{(B)} = [\vec{f}_{\alpha_{X_B}} \quad \vec{f}_{\alpha_{Y_B}} \quad \vec{f}_{\alpha_{Z_B}}]^T$, together with the transformation matrix $\check{T}^{(B,W)}$ of wind with respect to vehicle body coordinates, yields the wind-axes components of the aerodynamic force vector $\{\vec{f}_\alpha\}^{(W)} = [-D \quad -C \quad -L]^T$ as follows:

$$\{\vec{f}_\alpha\}^{(W)} = \check{T}^{(W,B)} \{\vec{f}_\alpha\}^{(B)} \quad (22)$$

$$\begin{bmatrix} -D \\ -C \\ -L \end{bmatrix} = \begin{bmatrix} c(\beta)c(\alpha) & s(\beta) & c(\beta)s(\alpha) \\ -s(\beta)c(\alpha) & c(\beta) & -s(\beta)s(\alpha) \\ -s(\alpha) & 0 & c(\alpha) \end{bmatrix} \begin{bmatrix} \vec{f}_{\alpha_{X_B}} \\ \vec{f}_{\alpha_{Y_B}} \\ \vec{f}_{\alpha_{Z_B}} \end{bmatrix} \quad (23)$$

where c represents cosine and s represents sine functions.

Note that the negative directions of aerodynamic force components relative to the positive directions of the wind axes, which is a universally used convention in the definition of positive lift and drag. In non-dimensional form, using non-dimensionalized aerodynamic force coefficients C_X, C_Y, C_Z for body axes and $-C_D, -C_C, -C_L$ for wind axes:

$$\begin{bmatrix} -C_D \\ -C_C \\ -C_L \end{bmatrix} = \begin{bmatrix} c_{(\beta)}c_{(\alpha)} & s_{(\beta)} & c_{(\beta)}s_{(\alpha)} \\ -s_{(\beta)}c_{(\alpha)} & c_{(\beta)} & -s_{(\beta)}s_{(\alpha)} \\ -s_{(\alpha)} & 0 & c_{(\alpha)} \end{bmatrix} \begin{bmatrix} C_X \\ C_Y \\ C_Z \end{bmatrix} \quad (24)$$

we can write it in the equation form as,

$$C_D = -c_{(\alpha)}c_{(\beta)}C_X - s_{(\beta)}C_Y - s_{(\alpha)}c_{(\beta)}C_Z \quad (25)$$

$$C_C = c_{(\alpha)}s_{(\beta)}C_X - c_{(\beta)}C_Y + s_{(\alpha)}s_{(\beta)}C_Z \quad (26)$$

$$C_L = s_{(\alpha)}C_X - c_{(\alpha)}C_Z \quad (27)$$

conversely,

$$\{\vec{f}_\alpha\}^{(B)} = \check{T}^{(B,W)}\{\vec{f}_\alpha\}^{(W)} = [\check{T}^{(W,B)}]^T\{\vec{f}_\alpha\}^{(W)} \quad (28)$$

$$\begin{bmatrix} C_X \\ C_Y \\ C_Z \end{bmatrix} = \begin{bmatrix} c_{(\beta)}c_{(\alpha)} & -s_{(\beta)}c_{(\alpha)} & -s_{(\alpha)} \\ s_{(\beta)} & c_{(\beta)} & 0 \\ c_{(\beta)}s_{(\alpha)} & -s_{(\beta)}s_{(\alpha)} & c_{(\alpha)} \end{bmatrix} \begin{bmatrix} -C_D \\ -C_C \\ -C_L \end{bmatrix} \quad (29)$$

giving;

$$C_X = -c_{(\alpha)}c_{(\beta)}C_D + c_{(\alpha)}s_{(\beta)}C_C + s_{(\alpha)}C_L \quad (30)$$

$$C_Y = -s_{(\beta)}C_D - c_{(\beta)}C_C \quad (31)$$

$$C_Z = -s_{(\alpha)}c_{(\beta)}C_D + s_{(\alpha)}s_{(\beta)}C_C - c_{(\alpha)}C_L \quad (32)$$

The incidence angle of the effective velocity vector over the body is changing during the transition, as can be seen in Figure 2.12. The wing axis will be rotating during the transition, while the body axis will be stationary during that period. The effective velocity vector is a vector summation of propeller slipstream velocity and body velocity. This issue is explained previously in Eq. 10 and 11. In hover mode, since body velocity is zero, the velocity vector is formed by propeller slipstream velocity. As wing tilts, the contribution of the propeller velocity vector to effective velocity decreases, and the contribution of the body velocity vector increases. The change of α of the body is shown in the last column of Table 2.11, and it can be clearly seen that α_{body} will always be negative and useless for aerodynamic analysis. Therefore

α_{wing} should be used as the angle of attack during transition flight analysis. While generating the CFD database wing coordinate system will be used as a base coordinate system. By the way, aerodynamic coefficients have been taken from CFD in the body coordinate system.

Table 2.11 Transition Flight Mode Power Requirements for One Motor

$\delta_{TW} (deg)$	RPM	$V_{prop}(m/s)$	$u_{body}(m/s)$	$u_{wing}(m/s)$	$w_{wing}(m/s)$	$V_{wing}(m/s)$	$\alpha_{wing}(deg)$	$\alpha_{body}(deg)$
90	488	7.559	0	7.559	0	7.559	0	-90
75	478	7.401	1.21	7.714	1.168	7.8	8.609	-66.391
60	444	6.855	3.19	8.445	2.762	8.884	18.1	-41.9
45	399	6.123	5.41	9.95	3.7	10.655	20.3	-24.7
30	333	5.022	6.82	10.93	3.41	11.449	17.27	-12.73
15	270	3.832	9.79	13.28	2.533	13.519	10.798	-4.202
0	244	2.594	16.47	19.06	0	19.06	0	0

The propeller velocity given in Table 2.11 is calculated using Eq. 33, which is given in [35]. The equation assumes that as thrust generated by propellers increases, induced velocity through propeller disc also increases.

$$V_{prop} = \sqrt{\frac{T}{2\rho A}} \quad (33)$$

where T is thrust, ρ is the air density, and A is the propeller disc area, respectively. Another study showed that propeller slipstream caused additional airspeed of 7-10 m/s on the wings [49]. It can be said that propeller velocity dominates the body velocity vector from tilt angles of 90° to 45°, while the opposite condition occurs between tilt angles of 45° and 0°. It should be noted that effective velocity is the V_{wing} for all flight conditions.

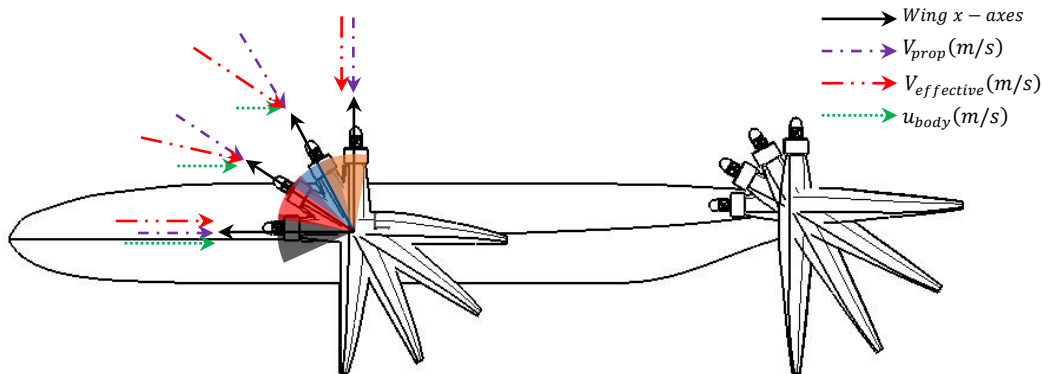


Figure 2.12. Effective Velocity and Angle of Attack changes during the transition

CFD analysis velocity vector coverage has been shown in Figure 2.12 with black, red, blue, and orange arcs. These arcs show where the velocity comes from during CFD analysis. For instance, at 45° tilt angle, the velocity vector spectrum changes from -59° to -25° with respect to the body. Resolving the vector in any coordinates is not essential for the accuracy of the analysis. It is essential to analyze the velocity spectrum, which represents the real flight conditions. Resolving the velocity vector in the wing coordinate does not affect the results; it only makes the velocity spectrum understandable.

2.4.1 Aerodynamic Database Generation

Aerodynamic forces and moments are modeled directly in wing coordinates, using non-dimensionalized body-axes aerodynamic force coefficients C_X, C_Y, C_Z and nondimensionalized body-axes aerodynamic moment coefficients (about vehicle CoM) C_l, C_m, C_n . The sign convention for a positive sense of the non-dimensional aerodynamic force and moment coefficients follow the positive direction (respectively, along with and about) the vehicle body coordinate axes.

The general functional form of aerodynamic force and moment coefficients can be represented as;

$$C_i = C_i(Re, \alpha, \beta, \dot{\alpha}^*, \dot{\beta}^*, p^*, q^*, r^*, \delta_a, \delta_e, \delta_{TW}, h, x_{CM}) \quad (34)$$

$$i = X, Y, Z, l, m, n \quad (\cdot)^* = \frac{d}{2V_T}(\cdot) \quad (35)$$

where $(\cdot)^*$ represents non-dimensionalized motion-related variables for angular rates, with reference length d representing wingspan b for lateral-directional parameters ($i = Y, l, n$), and wing MAC \bar{c} for longitudinal parameters ($i = X, Z, M$).

$$C_X = \bar{C}_X + C_{X_q} q^* \quad (36)$$

$$C_Y = \bar{C}_Y + C_{Y_r} r^* + C_{Y_p} p^* \quad (37)$$

$$C_Z = \bar{C}_Z + C_{Z_q} q^* + C_{Z_{\dot{\alpha}}} \dot{\alpha}^* \quad (38)$$

$$C_l = \bar{C}_l + C_{l_p} p^* + C_{l_r} r^* \quad (39)$$

$$C_m = \bar{C}_m + C_{m_q} q^* + C_{m_{\dot{\alpha}}} \dot{\alpha}^* \quad (40)$$

$$C_n = \bar{C}_n + C_{n_r} r^* + C_{n_p} p^* \quad (41)$$

For simulation (6-DoF Air Vehicle Simulation Model) and autopilot synthesis of VTOL UAV, the complicated functional form of aerodynamic coefficients are simplified using component buildup, where each “total” coefficient is modeled as the sum of static coefficients (that are, individually, functions of fewer variables), plus dynamic damping derivatives that correspond to the linear terms of the Taylor-series expansions (partial derivatives of the total coefficients) with respect to angular-rate variables $(\dot{\alpha}, \dot{\beta}, p, q, r)$. Component buildups of the “total” nondimensional aerodynamic coefficients for VTOL UAV, in their most general form, are then expressed in Eq. 36-41. Static coefficients, designated by an overhead bar, are the first terms on the right-hand side of the equations. These are followed by incremental terms, in the order of importance, consisting of the product of dynamic damping derivatives (indicated by an additional level of subscripts) with non-dimensionalized angular-rate variables, where $(\cdot)^* = \frac{b}{2V_T}$ for (p, r) -parameters and $(\cdot)^* = \frac{\bar{c}}{2V_T}$ for $(q, \dot{\alpha})$ -parameters. Body-rate (p, q, r) derivatives are the source of the critical damping effects on the natural modes of the vehicle.

Damping derivatives can be found using the Eq. 42-55, which are taken from[50]. While finding C_{Xq} and C_{Zq} , it has been assumed that $C_{Dq} = 0$ since we are in the subsonic Mach number regime. In the Eq. 42, x_w represents the distance between wing MAC and CoM, $C_{L\alpha_w}$ and $C_{L\alpha_H}$ are the lift curve slope of the wing and tail, η_H is the ratio of dynamic pressure at the tail to that of the free stream, and , C_{HT} is the tail volume coefficient, respectively.

$$C_{Xq} = s_{(\alpha)} C_{Lq} = s_{(\alpha)} \left(\left(\frac{1}{2} + \frac{2x_w}{\bar{c}} \right) C_{L\alpha_w} + 2C_{L\alpha_H} \eta_H C_{HT} \right) \quad (42)$$

$$C_{Zq} = -c_{(\alpha)} C_{Lq} = -c_{(\alpha)} \left(\left(\frac{1}{2} + \frac{2x_w}{\bar{c}} \right) C_{L\alpha_w} + 2C_{L\alpha_H} \eta_H C_{HT} \right) \quad (43)$$

Variation of pitching moment coefficient with pitch rate may be considered to be the sum of the wing and the tail contribution and be found by the Eq. (44). K is the

correction constant for wing contribution to C_{m_q} , where $K = 0.7$ for a wing with an aspect ratio (AR) of 6.95. For the current design, $\Lambda_{c/4} = 5^\circ$ and \bar{c} is the mean aerodynamic chord of the wing.

$$C_{m_q} = -KC_{L\alpha_w} \cos(\Lambda_{c/4}) \left[\frac{AR \left[2 \left(\frac{x_w}{\bar{c}} \right)^2 + \frac{1}{2} \left(\frac{x_w}{\bar{c}} \right) \right]}{AR + 2 \cos(\Lambda_{c/4})} + \frac{1}{24} \frac{AR^3 \tan^2(\Lambda_{c/4})}{AR + 6 \cos(\Lambda_{c/4})} + \frac{1}{8} \right] - 2C_{L\alpha_H} \eta_H C_{HT} \left(\frac{x_H}{\bar{c}} \right) \quad (44)$$

The equations for the angle of attack derivatives are given in Eq. 45 and 46;

$$C_{Z_{\dot{\alpha}}} = -c_{(\alpha)} C_{L_{\dot{\alpha}}} = -c_{(\alpha)} \left(1.5 \left(\frac{x_{acw}}{\bar{c}} \right) C_{L\alpha_w} + 3C_L(g) + 2C_{L\alpha_H} \eta_H C_{HT} \frac{d\epsilon}{d\alpha} \right) = -c_{(\alpha)} 0.53 \quad (45)$$

$$C_{m_{\dot{\alpha}}} = -C_{L\alpha_H} \eta_H C_{HT} \left(\frac{x_H}{\bar{c}} \right) \frac{d\epsilon}{d\alpha} = -3.72 * 0.61 * \left(\frac{x_H}{\bar{c}} \right) * 0.4 = -2.4 \quad (46)$$

The roll rate derivative of the side force can be assumed as zero. The roll rate derivative of the roll moment equation is Eq. (47). In this equation; $\kappa = \frac{C_{L\alpha}}{2\pi}$ and S and b reference area and wingspan, respectively.

$$C_{l_p} = C_{l_p W} + C_{l_p H} \quad (47)$$

$$C_{l_p W} = \left[\left(\frac{\sqrt{1-M^2} C_{l_p}}{\kappa} \right) \frac{\kappa}{\sqrt{1-M^2}} \right]_W + 0.5 \left[\left(\frac{\sqrt{1-M^2} C_{l_p}}{\kappa} \right) \frac{\kappa}{\sqrt{1-M^2}} \right]_H \frac{S_H}{S} \left(\frac{b_H}{b} \right)^2 = -0.28 \quad (48)$$

Variation of yawing moment coefficient with roll rate may be approximated from,

$$C_{n_p} = C_{n_p W} \quad (49)$$

$$C_{n_p} = \left(\frac{C_{n_p}}{C_L} \right)_{C_L=0, M=0} C_{L\alpha} \alpha = -\frac{1}{6} \frac{AR + 6 \left(AR + \cos(\Lambda_{c/4}) \right) \left(\frac{\bar{x}}{\bar{c}} \frac{\tan(\Lambda_{c/4})}{AR} + \frac{\tan^2(\Lambda_{c/4})}{12} \right)}{AR + 4 \cos(\Lambda_{c/4})} C_{L\alpha} \alpha \quad (50)$$

Variation of side force coefficient with yaw rate can be approximated as $C_{Y_r} = 0$. An approximation can be made that the variation of the rolling moment with yaw rate is equal to wing yawing derivative and be found from;

$$C_{l_r} = C_{l_{rW}} \quad (51)$$

$$C_{l_{rW}} = \left(\frac{C_{l_r}}{C_L} \right)_{C_L=0} C_L + \left(\frac{\Delta C_{l_r}}{\Gamma} \right) \Gamma + \left(\frac{\Delta C_{l_r}}{\theta} \right) \theta + \left(\frac{\Delta C_{l_r}}{\alpha_{\delta_f} \delta_f} \right) \alpha_{\delta_f} \delta_f \quad (52)$$

$$C_{l_{rW}} = \left(\frac{C_{l_r}}{C_L} \right)_{C_L=0} C_L = \left(1 + \frac{AR}{2(AR + 2\cos(\Lambda_{c/4}))} \right) \left(\frac{C_{l_r}}{C_L} \right)_{C_L=0} C_L + \left(\frac{\Delta C_{l_r}}{\alpha_{\delta_f} \delta_f} \right) \alpha_{\delta_f} \delta_f \quad (53)$$

$$C_{l_r} = C_{l_{rW}} = \left(1 + \frac{AR}{2(AR + 2\cos(\Lambda_{c/4}))} \right) * 0.26 * C_{L\alpha} \alpha - 0.0055 * \delta_f \quad (54)$$

Finally, the variation of yawing moment coefficient with yaw rate can be found using the following equation;

$$C_{n_r} = C_{n_{rW}} = \left(\frac{C_{n_r}}{C_L^2} \right) C_L^2 + \left(\frac{C_{n_r}}{\bar{C}_{D0}} \right) \bar{C}_{D0} = -0.03 * (C_{L\alpha} \alpha)^2 - 0.006 \quad (55)$$

Computational aerodynamic data (or “Aerodynamic Database”) consists of the entire static coefficients and dynamic damping derivatives discussed in the previous section. Data is compiled in the “Aerodynamic Database” in the form of multi-dimensional look-up tables as functions of the indicated variables. The functional dependency of all coefficients on geometric altitude h is ignored.

To give an example of creating aerodynamic database methodology, consider the minimum requirement for a simplified “Aerodynamic Database” of the static pitching moment coefficient \bar{C}_m , by ignoring secondary effects caused by the angle of attack (α), based on the following breakpoints of the independent variables:

$$\alpha = [-14^\circ, 20^\circ] \text{ with } 2^\circ \text{ increments}$$

$$\delta_e = [-20^\circ, 0^\circ, 20^\circ]$$

$$\delta_{TW} = [0^\circ, 90^\circ] \text{ with } 15^\circ \text{ increments}$$

$$\beta_f = [-30^\circ, 30^\circ] \text{ with } 15^\circ \text{ increments}$$

$$\delta_a = [-20^\circ, 0^\circ, 20^\circ]$$

Breakpoints indicate the values of independent variables ($\alpha, \delta_e, \delta_{TW}, \beta_f, \delta_a$) at which the value of its dependent variable (in this case: \bar{C}_m) is specified. They are given in

monotonically increasing form, starting with the minimum and ending with the maximum value. The resulting \bar{C}_m database, at these breakpoints, would then contain 5670 data points ($18 \times 3 \times 7 \times 5 \times 3$). Note that secondary effects caused by the angle of attack have been ignored. Also, note the sweep sequence of independent variables, starting with the breakpoints (from minimum to maximum) of the innermost independent variable, and proceeding outward towards the outermost independent variable.

2.4.2 Aerodynamic Analysis Results

The aerodynamic database has been generated using ANSYS/Fluent considering the methodology given above. 63 CAD geometries, (the combination of seven tilt angles position, three elevator deflections, and three aileron deflections) have been produced to generate the CFD data. CFD results are obtained, assuming that airspeed is equal to 20 m/s. This assumption is valid since, during the flight, airspeed is varying between 10 and 20 m/s, which means that Reynolds number is not changing very much and can be assumed to be equal for each tilt angle position. For Reynolds number calculation Eq. 56 can be used;

$$Re = \frac{\rho V l}{\mu} \quad (56)$$

The flight envelope is very close to sea level. Therefore, air density and viscosity can be assumed as constant. The reference length is also not changing during the flight. The only variable is airspeed to cover the whole flight envelope for the aerodynamic analysis. It has been calculated that for the level flight, the Reynolds number will be 500000, while for the vertical flight, it will be 250000. Assuming that, for all flight conditions, airspeed is constant, caused only %3 error in lift coefficient and 2.5% error in the drag coefficient.

Data gathered from CFD has been used to investigate the aircraft stability and augmentation of stability by designing a controller. In the following steps, the generated aerodynamic database will be presented.

Grid refinement study has been performed to obtain the optimal grid number, which gives an accurate solution by minimizing the grid number. Since CFD geometry of the study is not very simple and 44-core workstation, which reduces the run time of the analysis, has been employed for CFD runs, four million mesh number is acceptable for the study. Grid refinement study showed that after four million element number results became constant (Figure 2.13), which concludes that between four and five million elements will be sufficient for this study. Both drag and lift coefficients showed the same convergence characteristics. The CAD geometry, which is prepared for $\delta_{TW} = 0^\circ$, $\delta_a = 0^\circ$ and $\delta_e = 0^\circ$, has been used to conduct the grid refinement study. In addition to the grid refinement study, the results of the CFD have been compared with XFLR5 panel code results. They have complied with each other.

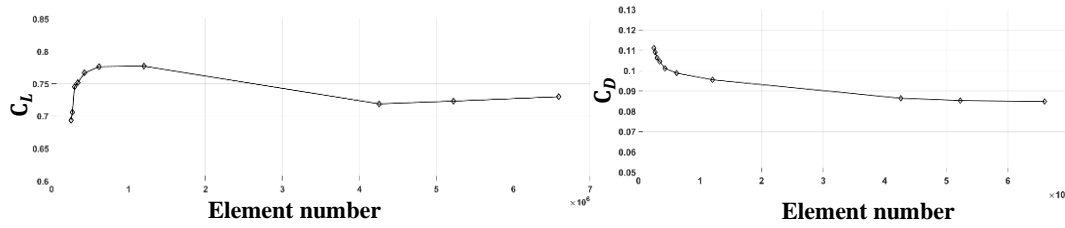


Figure 2.13. Grid Refinement Results for C_L and C_D

During the CFD analysis period, 5670 runs have been performed. Spalart Allmaras Turbulence model (1 Eq.) has been selected since this model is adequate to be used for low Reynolds number region. Typical y^+ value, which is one for Spalart Allmaras Turbulence Model, has been used for calculation of first layer thickness of the boundary layer. The first layer thickness of the boundary layer has been calculated as 0.03 mm. Element size has been calculated around between 4 and 5 million in accordance with the grid refinement study. There may be small differences in element size due to 63 different CAD geometries. It has been assumed that the flight level will be close to the sea level; therefore, air pressure is assumed to be 101325 Pa.

The propeller slipstream causes additional airspeed of 7-10 m/s on the wings during the transition [49]. Moreover, the body velocity increases from 0 to 16.1 m/s during the transition flight. We can say that total airspeed over the aircraft is varying from 10 to 20 m/s during the whole flight envelope. Therefore, for all flight conditions, airspeed is assumed to be 20 m/s. This assumption caused only %3 error in the lift coefficient and 2.5% error in the drag coefficient.

An example of the grid domain can be seen in Figure 2.14, which shows the zero-tilt angle, aileron, and elevator deflection geometry. The grid domain has a hemisphere that has a 25 m radius in front of the aircraft and a cylinder having 50 m length.

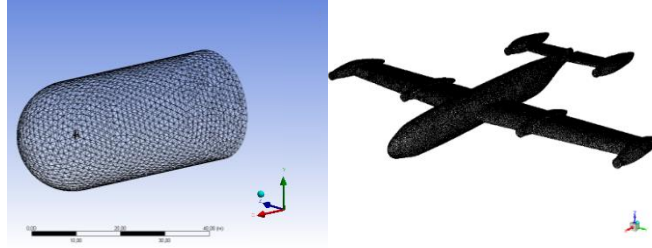


Figure 2.14. Grid Domain of the study

Lift coefficient variation for the whole aircraft shows that there will not be significant C_L change in conversion mode; as expected, the maximum lift coefficient has been observed in forward flight conditions. Note that the CFD analysis is done in wing coordinates, which means that zero α means the wing and airspeed are aligned with each other.

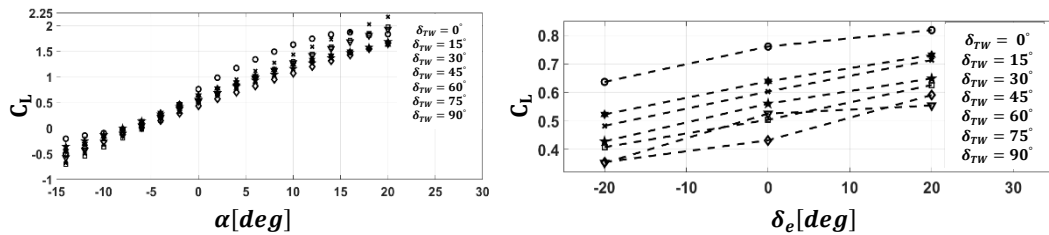


Figure 2.15. C_L Variation for Different Flight Conditions

It has been observed that for all tilt-wing angles, the minimum drag coefficient is placed at zero α . The drag coefficient decreases dramatically by the tilt angle

decrease. The drag coefficient changes will affect the control allocation, which will be presented in the next section, directly.

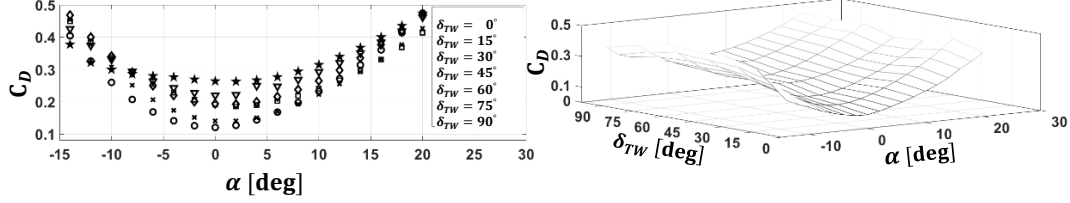


Figure 2.16. C_D Variation for Different Flight Conditions

C_m variation with respect to the CoM gives us feedback about aircraft stability in the longitudinal axis. Our aircraft is statically stable in every tilt angle except for vertical flight. We observed an adequate increase in pitch moment by increasing the elevator deflection. Pitch non-linearity and pitch up behavior of the aircraft are acceptable.

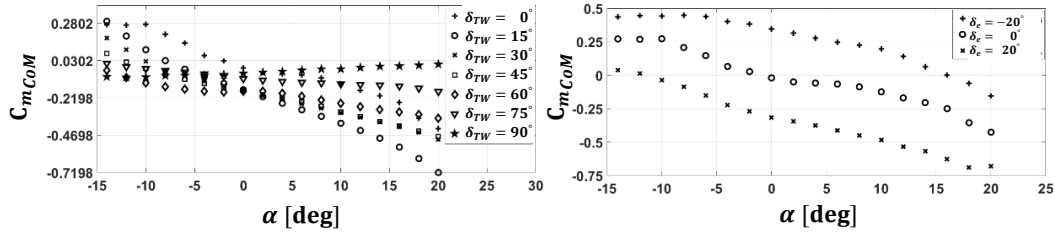


Figure 2.17. C_m Variation for Different Flight Conditions

Figure 2.18.a shows the roll moment variation with respect to α for $\delta_a = 20^\circ$, all tilt angles and $\beta = 0^\circ$ and while Figure 2.18.b shows the roll moment variation with respect to α for $\delta_{TW} = 0^\circ$, all aileron deflections and $\beta = -15^\circ$. The rolling moment for all tilt angles seems to be constant except for $\delta_{TW} = 0^\circ$ with respect to α . Roll moment is calculated as zero for $\delta_{TW} = 90^\circ$ since there is no aileron deflection in that tilt angle. Instead of ailerons, flaps are used at $\delta_{TW} = 90^\circ$.

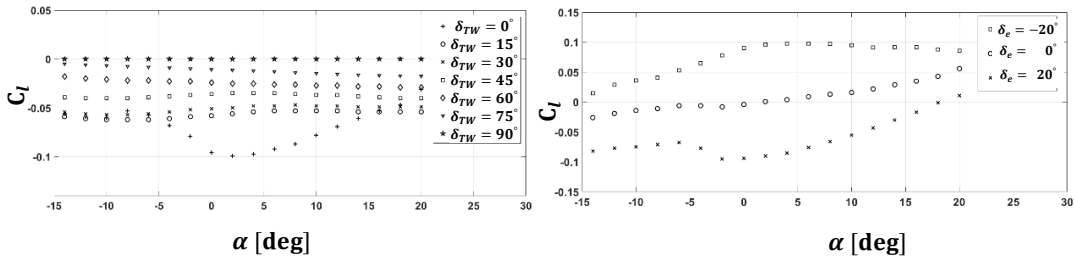


Figure 2.18. C_l Variation for Different Flight Conditions

Aircraft is directionally unstable since there is no vertical tail to stabilize the directional axis. It can be inferred from Figure 2.19.a that yaw moment decreases as α increases for all tilt angles. Figure 2.19.a is calculated for $\beta = -15^\circ$ and $\delta_a = 20^\circ$, while Figure 2.19.b for $\delta_{TW} = 0^\circ$. Directional axis stability will be augmented by employing the differential thrust of front motors.

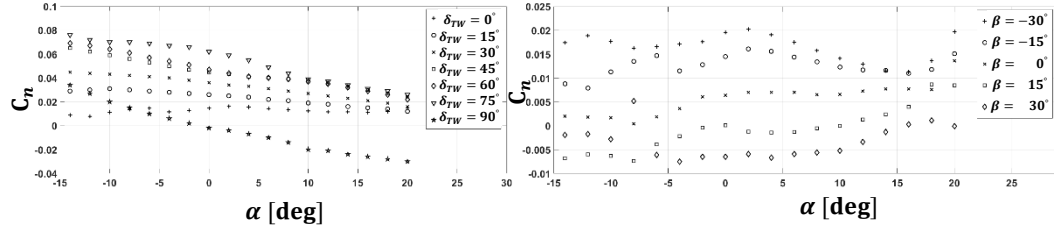


Figure 2.19. C_n Variation for Different Flight Conditions

The pressure coefficient and vorticity contours have been gathered using Fluent and CFD Post Features. The pressure coefficient is a dimensionless number that describes the relative pressures throughout a flow field in fluid dynamics. The baseline case is flight condition where TWA, aileron, elevator deflections, α , and sideslip angles are equal to zero. Each flight condition is compared with respect to baseline case via using pressure and vorticity contours.

Figure 2.20 shows that as α increases, pressure on the bottom of the wing increases. This condition increases C_L value, which can be seen in Figure 2.15. From pressure distribution in Figure 2.20, we can also say that the center of pressure goes forward which leads C_m to decrease.

Figure 2.21 shows that there is an asymmetric pressure distribution on aircraft, which results in a decrease in C_n and an increase in C_l values. Additionally, it can also clearly be seen from Figure 2.21 that the pressure coefficient is slightly decreasing as sideslip increases. That condition leads C_L to decrease. Note that, sideslip angle is in a positive direction, which means that airflow is coming from the right side of the aircraft. The stagnation point moves to the right side of the fuselage.

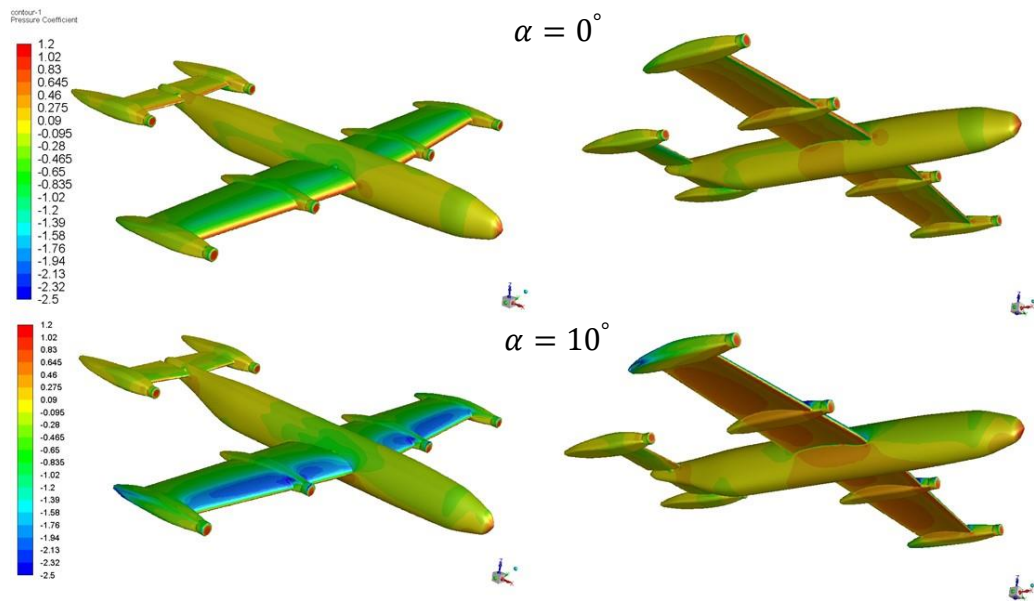


Figure 2.20. Pressure Contours at Different Angles of Attack

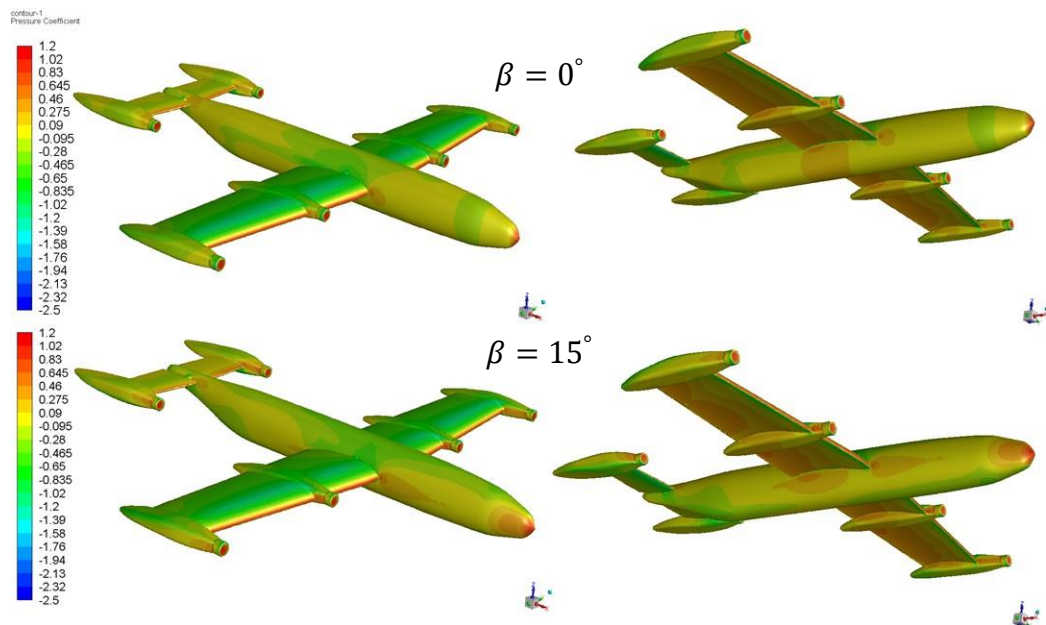


Figure 2.21. Pressure Contours at Different Sideslip Angles

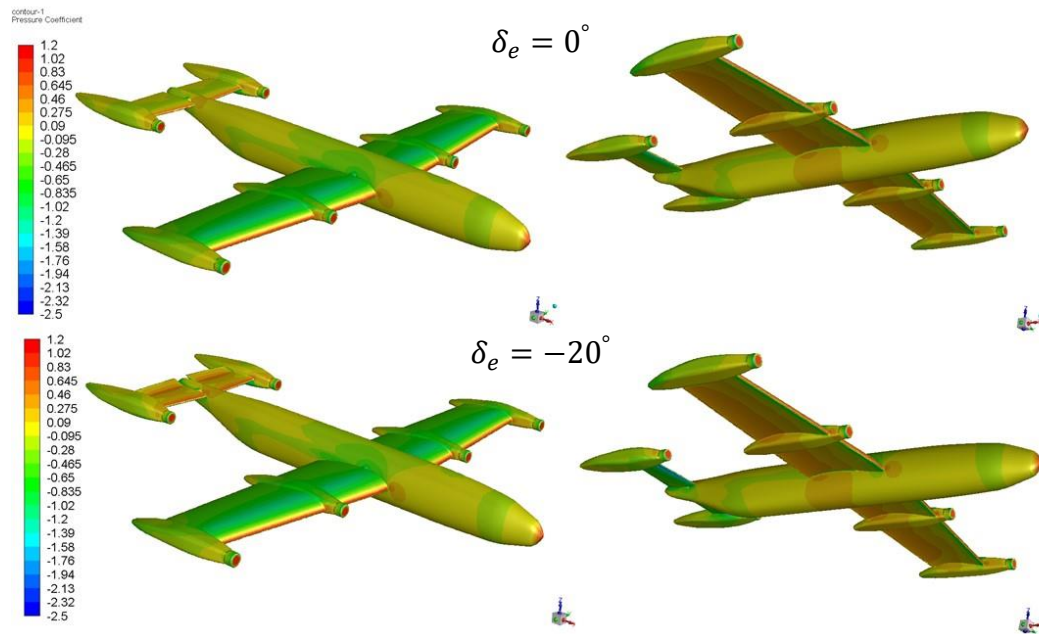


Figure 2.22. Pressure Contours at Different Elevator Angles

It can be readily seen from Figure 2.22 that pressure on the upper side of the horizontal stabilizer is increased as the elevator is negatively deflected. This condition causes the center of pressure to go backward, and a positive moment on aircraft is obtained, as can be seen from Figure 2.17. Pressure increase on the upper side of the elevator has an effect on C_L as well. Since the pressure on the upper side of the aircraft increases, the total lift decreases accordingly.

Roll moment is obtained by aileron deflection in most parts of the mission. There is a pressure distribution difference between aileron deflected and no deflection case. The pressure increase on the bottom side of the right-wing is remarkable (Figure 2.23). This pressure difference generates an additional lift on the right side and creates a roll moment. The left side is also active on roll moment; however, most of the contribution comes from the right-wing.

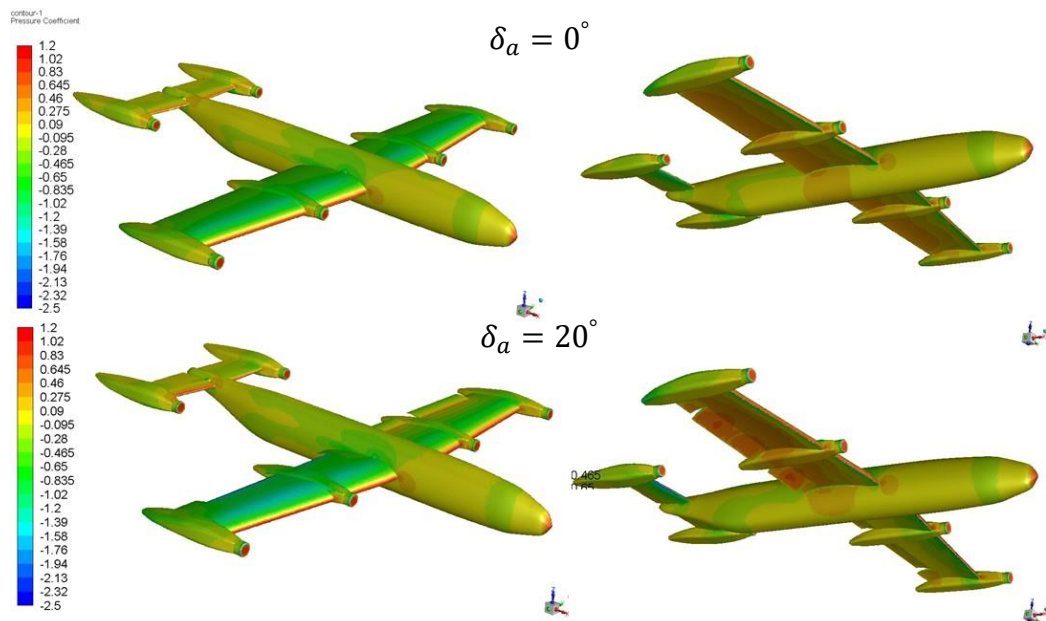


Figure 2.23. Pressure Contours at Different Aileron Angles

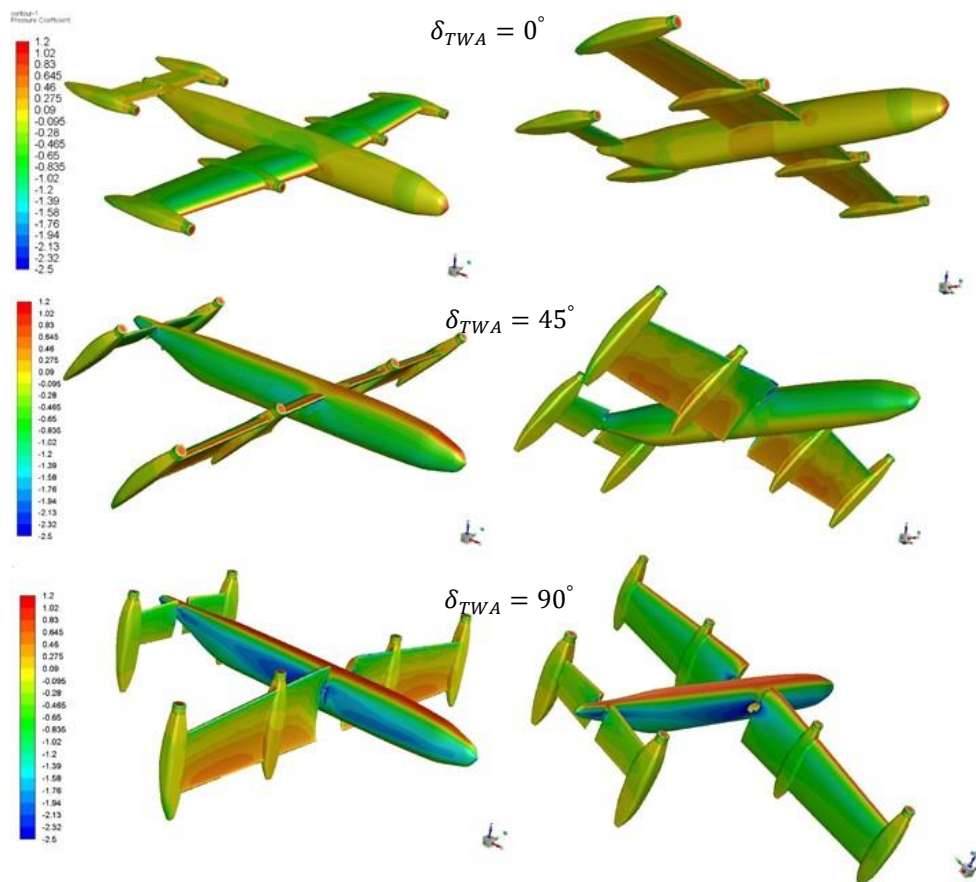


Figure 2.24. Pressure Contours at Different Tilt Angles

Figure 2.24 shows the effect of Tilt Wing Angle on pressure distribution. Note that each distribution is obtained at 0° α of the wing. Pressure on the wing root is affected from the fuselage at $\delta_{TWA} = 45^\circ$. Force, which is used in longitudinal control, is generated on body x-axis at $\delta_{TWA} = 90^\circ$ due to the lift on the wing. Pressure increases at the upper side of the fuselage as the tilt angle increases. This condition decreases the lift generated by the aircraft.

The vorticity magnitude increases as the α increases as expected. Behind the engine nacelles, there are strong vorticities which could be optimized according to these results.

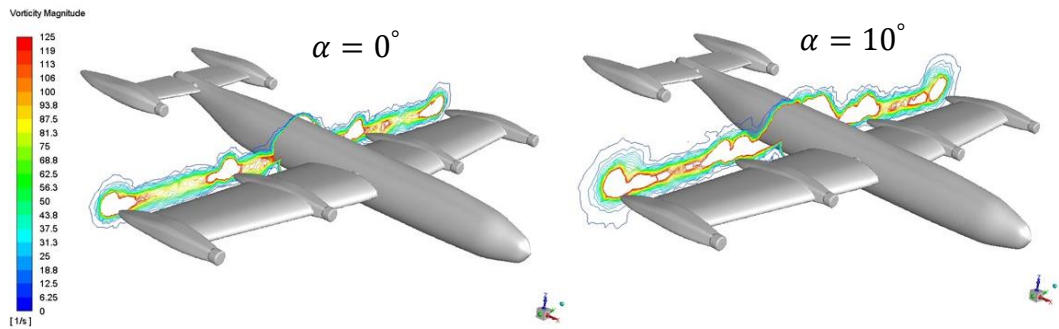


Figure 2.25. Vorticity Contours at Different Angles of Attack

Asymmetric Vorticity contours stand out in Figure 2.26 as expected. It can also be said that vorticity increases as the sideslip angle increases. Note that, the vorticity contours have been plotted in a plane which is 10 centimeters far from wingtip engine nacelles. Different vorticity contours can be obtained when the distance from engine nacelles is changed.

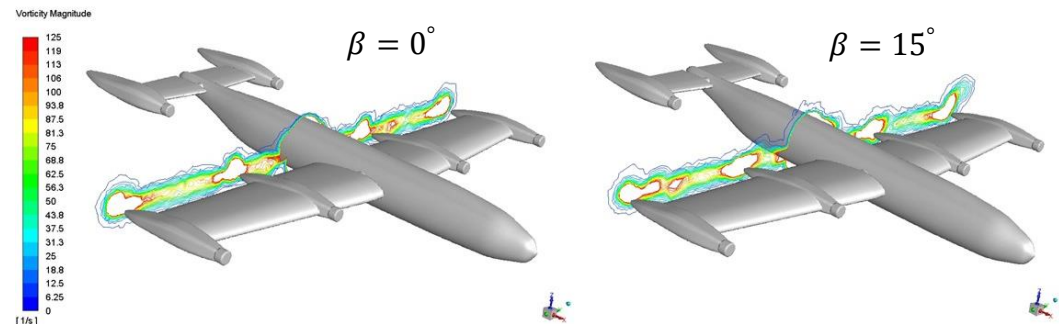


Figure 2.26. Vorticity Contours at Different Sideslip Angles

Figure 2.27 shows the elevator deflection effect on the vorticity contours. It can be readily said that vorticity contours have almost the same trend in two conditions, with only slight differences. The backside of the root engine nacelles is changed slightly due to wing and elevator interaction. Since the pressure is changed on the elevator, vorticity is affected.

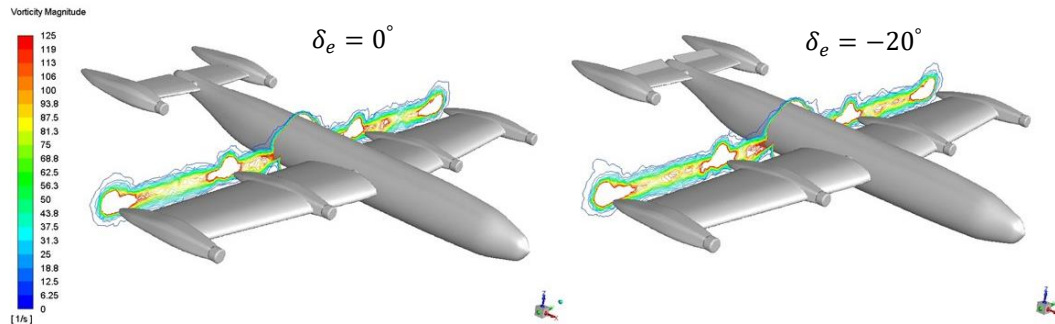


Figure 2.27. Vorticity Contours at Different Elevator Angles

Aileron deflection creates additional singularities on vorticity contours due to the affected flow behind the ailerons. Additionally, vorticity contours around the fuselage are also being affected by the aileron deflection, as can be seen from Figure 2.28. Note that negative aileron deflection creates more vorticity contours than positive aileron deflection, which means that the flow is negatively affected behind left-wing.

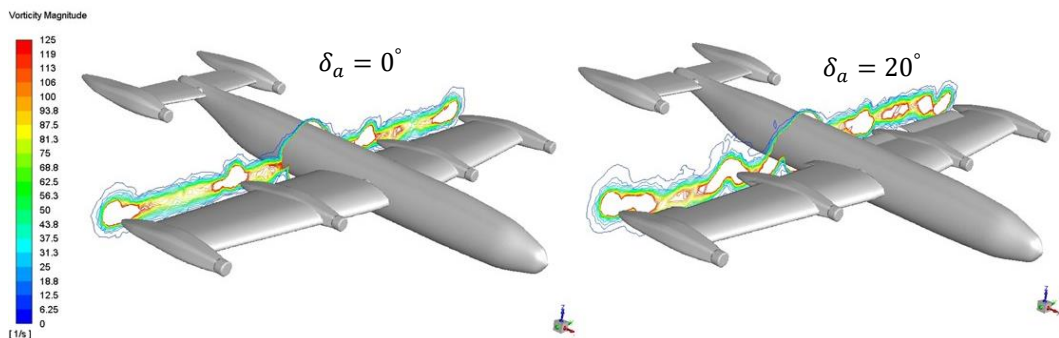


Figure 2.28. Vorticity Contours at Different Aileron Angles

Tilt wing deflection is also influential in vorticity creation. As the tilt angle closes 45° , vorticity increases exponentially. Nevertheless, 0° and 90° tilt angles show similar behaviors.

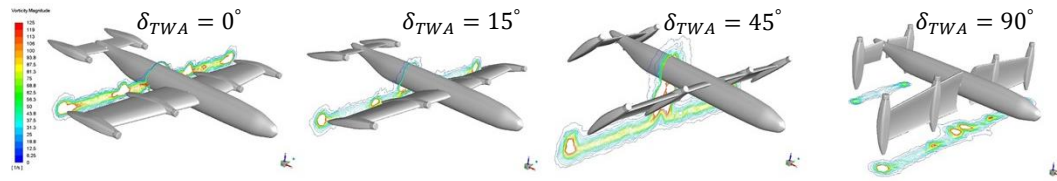


Figure 2.29. Vorticity Contours at Different Tilt Angles

2.4.3 Motor and Battery Database Generation

Front and rear motors are different from each other. More powerful motors are used for wing, which is the main thrust generator for the aircraft. As airspeed increases, thrust levels of the motors are decreasing. Thrust increases exponentially when the motor RPM increases. Thrust levels for a specific flight condition have been calculated using Neu-Motors e-Calc motor and battery package selection tool. This program takes motor, battery and propeller package, airspeed, and RPM level as input and generates the thrust level at the related condition. The thrust database is embedded into the non-linear Simulink model by using look-up tables. The look-up tables accept RPM and airspeed as inputs and produce thrust as an output, instantaneously. There are separate look-up tables for each motor since their RPMs could be different from each other.

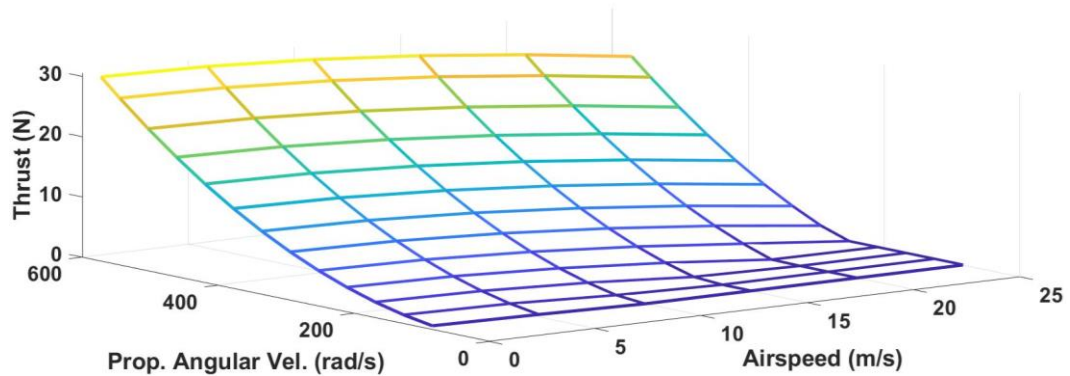


Figure 2.30. Front Motors Database

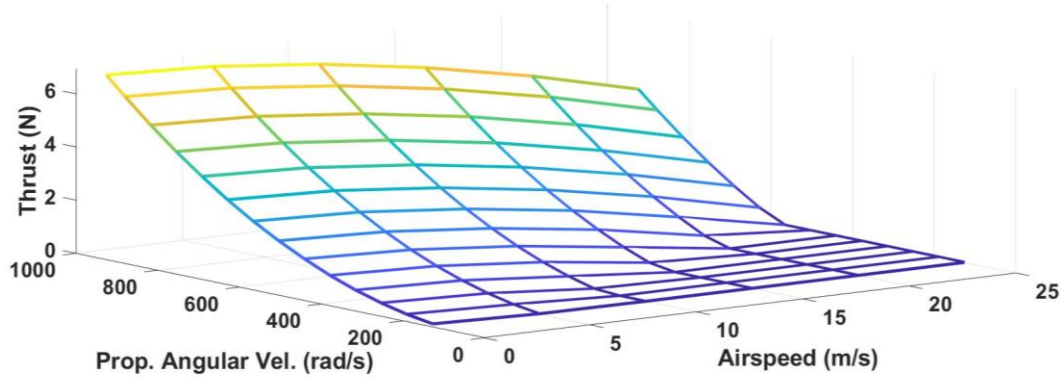


Figure 2.31. Rear Motors Database

Since the front motors are powerful than rear motors, their energy consumption is also higher than the rear motors. Therefore, for front and rear batteries, separate lookup tables are used. The non-linear dynamic model calculates the energy consumption for each iteration and counts down the charge level cumulatively. When the battery energy level drops to zero, the non-linear model will not produce a motor thrust for the related motor. Figure 2.32 and 2.33 shows the discharge trends of the front and rear motors.

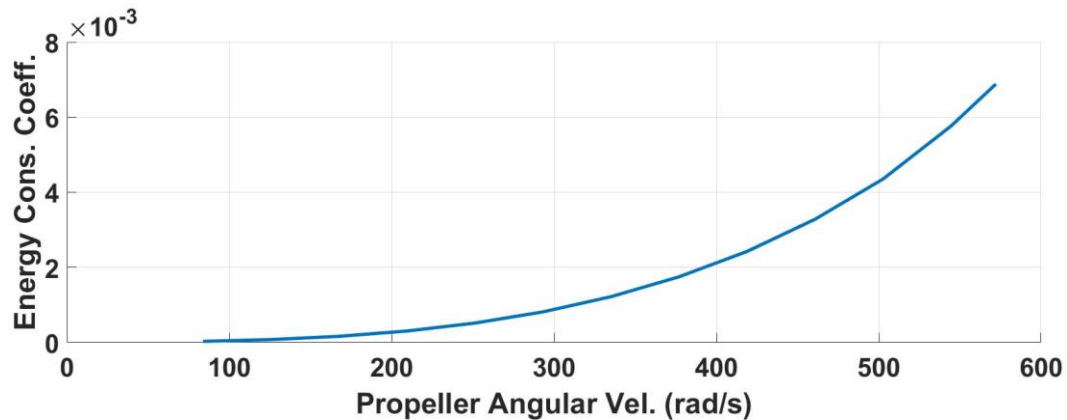


Figure 2.32. Front Batteries Discharge Database

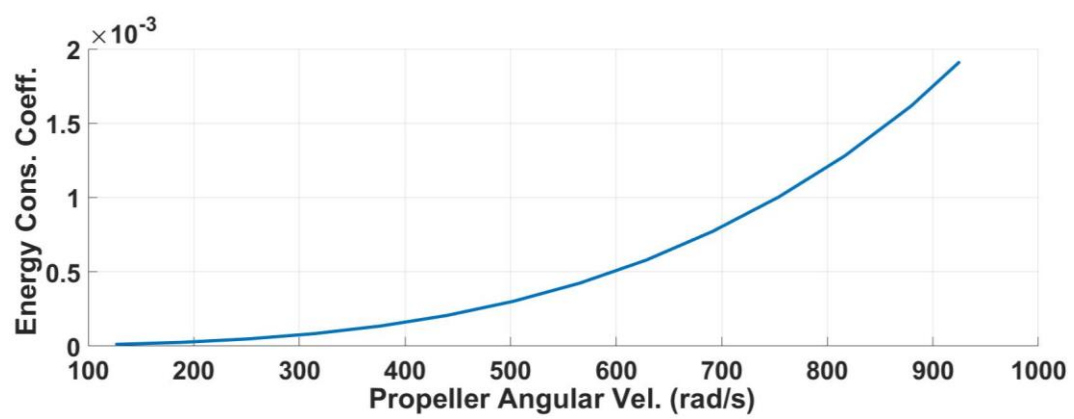


Figure 2.33. Rear Batteries Discharge Database

CHAPTER 3

NONLINEAR DYNAMIC MODEL

The air vehicles have very complex dynamics, therefore making an accurate model is a challenging problem for a full flight envelope. Flight envelope has been divided into several parts in order to solve the complexity of the aircraft dynamics. The mathematical model of the UAV has been developed in MATLAB/Simscape, which enables us to represent real air vehicle dynamics at an adequate level. Following assumptions has been made in developing the Simscape Model:

- There is no IGE (In-Ground Effect).
- There is sufficient slipstream coming from propellers, which is covering all over the wing.
- The propeller, control, and inflow dynamics are considered to be faster than the aircraft's dynamics.
- The blades of the propellers and aerodynamical surfaces assumed to be rigid.
- Mass and inertia tensor of the aircraft is constant during the flight.
- Sea level conditions are valid for atmospheric variables.

3.1 Reference Frames and Coordinate Systems

For modeling the endo-atmospheric motion of rigid-body air vehicles, three frames must be introduced. They are:

- Earth-centered inertial (ECI) frame $\mathcal{F}_I\{\hat{i}_I, \hat{j}_I, \hat{k}_I\}$,
- Earth-centered-Earth-fixed (ECEF) frame $\mathcal{F}_E\{\hat{i}_E, \hat{j}_E, \hat{k}_E\}$,
- Vehicle body-fixed frame $\mathcal{F}_B\{\hat{i}_B, \hat{j}_B, \hat{k}_B\}$,

These are described in the following sections, along with some other frames and coordinate systems that will be additionally required in Modeling and Simulation activities (such as vehicle aerodynamics) of the 6-DoF Air Vehicle Simulation Model.

3.1.1 Earth-Centered Inertial (ECI) and Earth-Centered-Earth-Fixed (ECEF) frames

ECI and ECEF frames have coinciding origins I and E , respectively, located at the center of the Earth (which almost coincides with its CoM), as shown in Figure 3.1. ECI frame \mathcal{F}_I has its base vector \hat{i}_I aligned with the vernal equinox, \hat{k}_I has direction and sense with the Earth's axis of rotation, and \hat{j}_I completes the right-handed triad. It is defined as an inertial (Newtonian) frame, thus neglecting the motion of Earth's orbit around the sun and the wobbling of Earth's (mean) rotation axis. ECEF frame \mathcal{F}_E , on the other hand, is fixed to the Earth and rotates with the Earth. Its base vector \hat{i}_E points at the intersection of the Prime (Greenwich) meridian with the Equator, \hat{k}_E corresponds to the Earth's rotation axis (same as \hat{k}_I) and points at the North Pole, and \hat{j}_E completes the right-handed triad.

ECI and ECEF coordinate systems are the preferred coordinate system of ECI and ECEF frames, which have their coordinate axes aligned with the respective base vectors of these frames. The Z_E -axis intersects with the Earth's surface at the North and South poles, with the surface representing the global mean sea level (MSL). The $X_E Y_E$ plane lies midway between the poles, orthogonal to the axis of rotation, and bisects the Earth into North and South hemispheres. On the surface, the line at which the hemispheres meet is the Equator. The so-called sidereal day is a full 360° rotation of the Earth relative to the stars and corresponds to the time elapsed since the X_E -axis coincides with the X_I -axis. This is about 4 minutes shorter than 24 hours, with the extra time only required for the Earth to present the same face to the sun (due to the Earth's movement on the ecliptic), the so-called solar day. The resultant sidereal rate of rotation ω_E corresponds to the angular speed of the Earth about

[illegible]

point on or above the surface of the Earth (such

For a round Earth Model, local geographic coordinates (of longitude and latitude) are named geocentric; for a spherical Earth, then, geocentric latitude, denoted by ϕ_c , represents the angle that the equatorial plane makes with the radial line from the center of the Earth to a point on or above the spheroid surface; this angle is depicted in Figure 3.1. The first rotation then represents terrestrial longitude l about the Z_E -axis starting at the prime meridian, defined with a range of $\pm 180^\circ$ and positive clockwise (easterly) direction, (the celestial longitude λ , measured about the Z_I -axis starting at the vernal equinox, is related to the terrestrial longitude l through the hour angle Ξ , via the relation $\lambda = \Xi + l$) and then the geocentric latitude ϕ_c about the new Y_E' -axis, defined with a range of $\pm 90^\circ$ from the Equator and positive North direction, as shown in Figure 3.1. A final -90° rotation is additionally required about the same axis in order to align the Up-East-North coordinates to North-East-Down, with “down” meaning along the local normal at Earth’s surface. The resultant geocentric coordinates in Figure 3.1 have $X_N Y_N$ plane tangential to the Earth’s surface at the vehicle’s latitude and longitude and point North and East, respectively, whereas Z_N -axis acts normal to the surface and points downward, in the direction of the local gravity vector (which intersects with the center of the Earth if a spherical Earth model is used). For obvious reasons, these local geographic coordinates are also called local (geocentric) North-East-Down (NED) coordinates. The local geodetic NED coordinate system is also used for navigation purposes, and often named the local navigation coordinate system, which is the reason for using subscript N .

3.1.2 Vehicle Body-Fixed Frame

The vehicle body-fixed frame \mathcal{F}_B has its origin B located at the instantaneous CoM of the air vehicle, as shown in Figure 3.1 and 3.2, with the corresponding preferred body coordinate system having its X_B -axis parallel with the longitudinal body centerline and pointing toward the nose of the vehicle, the Y_B -axis directed to the right (starboard) when viewed from the rear, and the Z_B -axis pointing in a direction below the horizon.

Table 3.1 Nomenclature for Vector Components Resolved in Vehicle Body Coordinates

Vector Symbol	Description	Vehicle Body-Axes Components			
		Notation	$X_B - axis$	$Y_B - axis$	$Z_B - axis$
$\vec{v}_{B/E}^E$	Translational velocity vector of vehicle CoM (point B) w.r.t. Earth (point E) observed in \mathcal{F}_E .	$\{\vec{v}_{B/E}^E\}^{(B)}$	u	v	w
$\vec{v}_{w/E}^E$	The translational velocity vector of the wind (coinciding with point B) w.r.t. Earth (point E) observed in \mathcal{F}_E .	$\{\vec{v}_{w/E}^E\}^{(B)}$	u_w	v_w	w_w
$\vec{\omega}^{B/E}$	The angular velocity vector of the vehicle body frame \mathcal{F}_B w.r.t. ECEF frame \mathcal{F}_E .	$\{\vec{\omega}^{B/E}\}^{(B)}$	p	q	r
$\vec{a}_{B/E}^E$	Translational acceleration vector of vehicle CoM (point B) w.r.t. Earth (point E) observed in \mathcal{F}_E .	$\{\vec{a}_{B/E}^E\}^{(B)}$	a_{X_B}	a_{Y_B}	a_{Z_B}
\vec{f}	The vector summation of all external forces.	$\{\vec{f}\}^{(B)}$	f_{X_B}	f_{Y_B}	f_{Z_B}
\vec{m}_B	The vector sum of all external moments referred to the vehicle CoM (point B).	$\{\vec{m}_B\}^{(B)}$	L	M	N

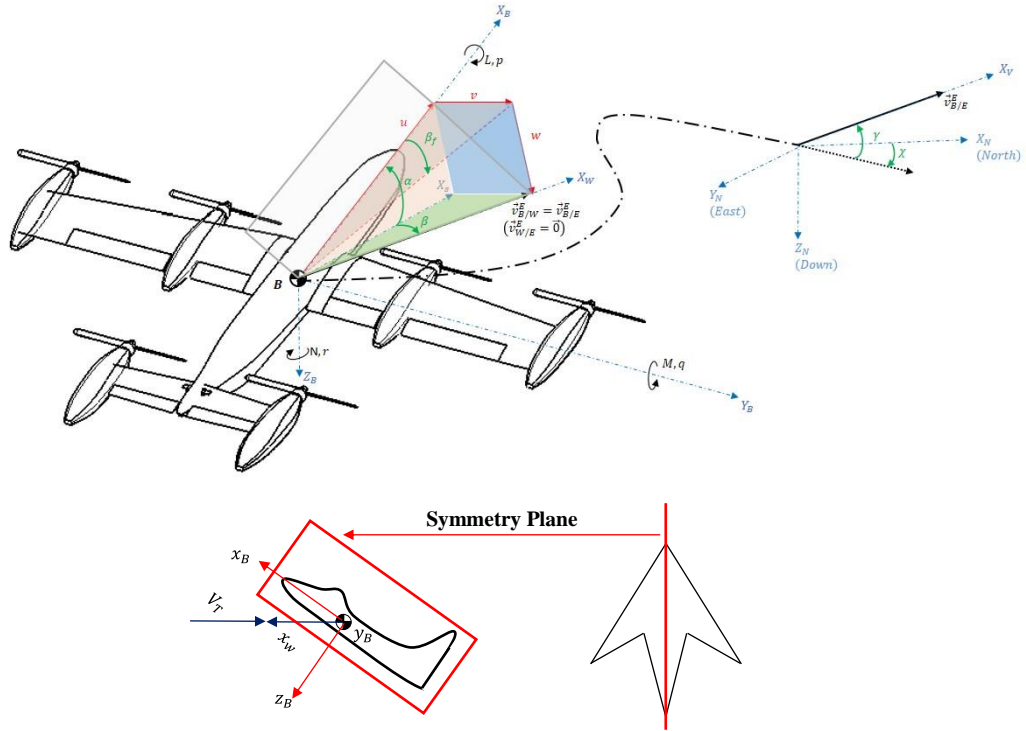


Figure 3.2. Vehicle Body, Wind and Velocity Frames, and Coordinate Systems

Figure 3.4 also shows the conventions used for positive directions of vector components in the body coordinate system. The nomenclature adopted here is presented in Table 3.1. The six projections of the linear (translational) and angular (rotational) velocity vectors ($\vec{v}_{B/I}^I$ and $\vec{\omega}^{B/I}$) on the moving body coordinate axes are the six degrees of freedom that will be simulated by the 6-DoF Air Vehicle

Simulation Model. By definition, body coordinates are related to local geocentric NED (navigation) coordinates through a 3-2-1 (yaw-pitch-roll) Euler angle sequence $\psi - \theta - \phi$, respectively.

Corresponding to origin B of the vehicle body-fixed reference frame \mathcal{F}_B and its associated preferred body coordinate system, a vehicle reference coordinate system is often additionally introduced associated with \mathcal{F}_B in order to locate items in/on the vehicle (such as accelerometer location, aerodynamic moment reference center, CoM location). This right-handed coordinate system has precisely the same orientation as the vehicle body coordinate system, and its origin R is defined to be at CoM of the vehicle since CoM is not changing during the flight.

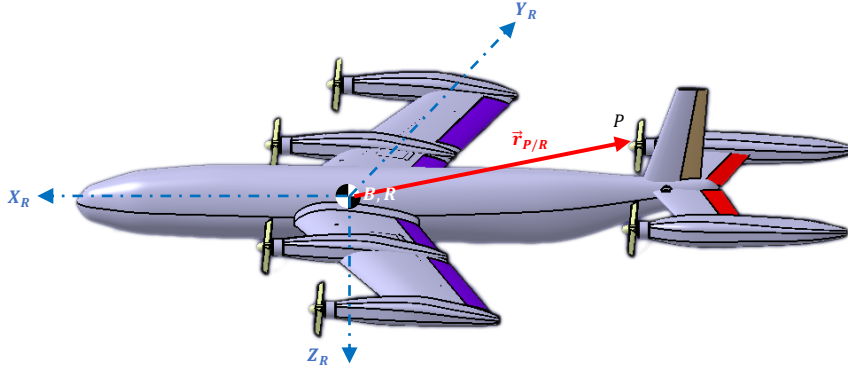


Figure 3.3. Vehicle Reference Coordinate System

The vehicle reference coordinate system is illustrated in Figure 3.3, together with the position vector $\vec{r}_{P/R}$ of an arbitrary point P on the vehicle. Note that any such location on the vehicle (such as accelerometers, gyroscopes, air data sensors, CoM location, CoM offsets, point of application of thrust, moment reference center) must always be given with respect to point R in vehicle reference coordinates. In doing so, the position vector $\{\vec{r}_{P/R}\}^{(R)}$ in vehicle reference coordinates will only hold negative values along X_R , Y_R and Z_R coordinates if point P happens to be located on the rear, left (port), and above the CoM of the vehicle, respectively.

3.1.3 Wind Frame

As the vehicle moves through the air mass, it experiences a relative wind over its body, which gives rise to aerodynamic forces. Introducing the wind frame $\mathcal{F}_W\{W; \hat{i}_W, \hat{j}_W, \hat{k}_W\}$, having its origin W coinciding with point B (vehicle CoM), the X_W -axis of its preferred wind coordinate system, depicted in Figure 3.2, lies along the velocity vector $\vec{v}_{B/W}^E$ of the vehicle CoM w.r.t. the air mass (observed in \mathcal{F}_E). This gives rise to the Cartesian incidence/wind angles of the pitch-plane angle of attack α and yaw-plane sideslip angle β , as shown in Figure 3.2. The orientation of vehicle body coordinates relative to wind coordinates is thus related through the Cartesian wind angles α and β . By Convention, Cartesian wind angles are defined as positive relative to the so-called (intermediate) stability coordinates (X_S -axis) depicted in Figure 3.2, so that body coordinates are the orientation of wind coordinates using negative β and positive α rotation sequence. The so-called geographic velocity vector $\vec{v}_{B/E}^E$ of the CoM w.r.t. the Earth is then expressed in terms of $\vec{v}_{B/W}^E$ (velocity of the CoM w.r.t. the air mass) and $\vec{v}_{W/E}^E$ (velocity of the wind w.r.t. Earth) as;

$$\vec{v}_{B/E}^E = \vec{v}_{B/W}^E + \vec{v}_{W/E}^E \quad (57)$$

Note that wind has been omitted ($\vec{v}_{W/E}^E = 0$) in Figure 3.2, so that $\vec{v}_{B/E}^E$ and $\vec{v}_{B/W}^E$ represent the same vector for ease of illustrating the aerodynamic wind angles.

3.1.4 Velocity (Flight Path)

The wind frame \mathcal{F}_W , having origin W coinciding with B , relates $\vec{v}_{B/W}^E$ to the body frame \mathcal{F}_B . In order to relate $\vec{v}_{B/E}^E$ to the ECEF frame \mathcal{F}_E , an additional frame is introduced called the velocity frame $\mathcal{F}_V\{V; \hat{i}_V, \hat{j}_V, \hat{k}_V\}$ (also known as the flight path frame), having origin V coinciding with B , and the X_V the coordinate axis of its preferred velocity coordinate system lies along the geographic velocity vector $\vec{v}_{B/E}^E$.

Two angles γ and χ then describe the instantaneous angular orientation of velocity coordinates relative to local geocentric coordinates, as shown in Figure 3.2, the latter related to ECEF coordinates through longitude and geocentric latitude. The horizontal flight path angle (or heading angle) χ is measured from North to the projection of $\vec{v}_{B/E}^E$ into the local tangent plane $X_N Y_N$ (positive clockwise about downward vertical Z_N), such that North and East are expressed by 0° and 90° , respectively. The vertical flight path angle γ takes this projection vertically up to $\vec{v}_{B/E}^E$. Note that only X_W -axis of the wind coordinates has been defined without ambiguity, and so the orientation is now described relative to the velocity coordinates through the bank (roll) angle μ . The wind and velocity coordinates are then related through μ about the velocity vector such that, in the absence of wind ($\vec{v}_{W/E}^E = 0$) the velocity coordinates are obtained by rotating about X_W , so that X_V always acts parallel to the horizontal plane $X_N Y_N$ of local geocentric coordinates.

3.1.5 Propulsion or Wing Coordinate Systems

If the main thrust from the engine (or propulsion system) of an air vehicle is either intentionally vectored (by design), the resulting propulsive thrust vector $\vec{f}_{P(\cdot)}$ in propulsion (engine) coordinates, where (\cdot) signifies “FL”, “FR”, “RL” and “RR” for front-left, front-right, rear-left and rear-right engine of the air vehicle, is defined relative to the vehicle body coordinates as shown in Figure 3.3, where point $P(\cdot)$ represents the point of application of thrust. $X_{P(\cdot)}$ -axis of propulsion coordinates have been defined in Figure 3.3 along the thrust force vector $\vec{f}_{P(\cdot)}$ so that, in propulsion coordinates, it can be expressed as;

$$\{\vec{f}_{P(\cdot)}\}^{(P(\cdot))} = [T_{(\cdot)} \quad 0 \quad 0]^T \quad (58)$$

where $T_{(\cdot)}$ represents the magnitude of the axial thrust from the primary propulsion system. Figure 3.4 also shows that the resulting propulsion coordinates are a

transformation of body coordinates using pitch rotation only, represented by the respective angles δ_{TW} and δ_{TT} .

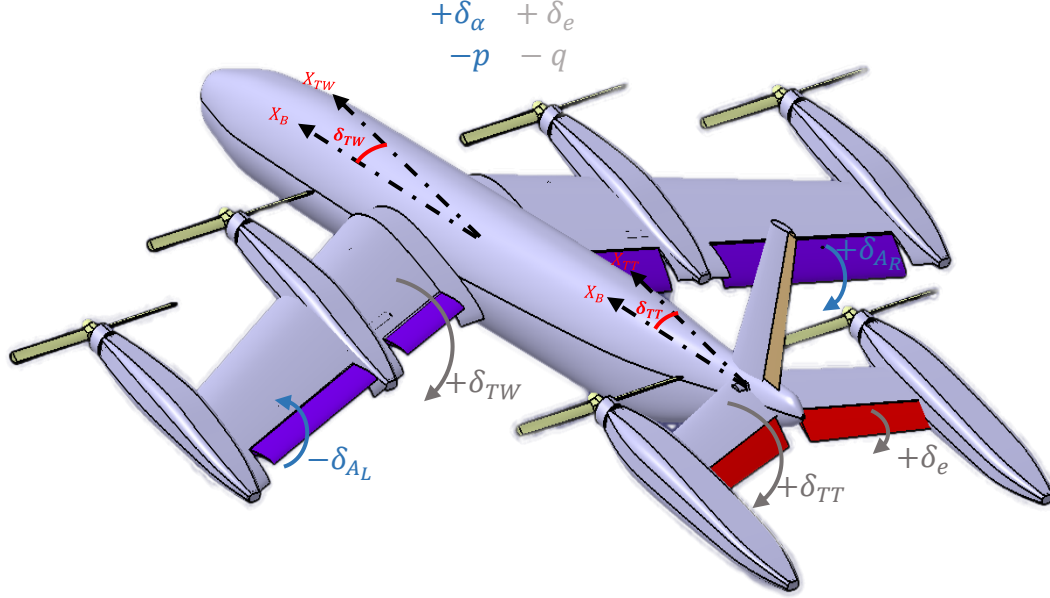


Figure 3.4. Sign Convention for Aerodynamic Control Inputs

Recall that the location of point $P(\cdot)$ must be supplied relative to point R in vehicle reference coordinates (Figure 3.3) as;

$$\{\vec{r}_{P(\cdot)/R}\}^{(R)} = [X_{P(\cdot)} \quad Y_{P(\cdot)} \quad Z_{P(\cdot)}]^T \quad (59)$$

where R represents the CoM, according to the definition of the vehicle reference coordinate system, note that:

$$\begin{aligned} X_{P(\cdot)} &> 0 \text{ for positions front of the CoM} \\ Y_{P(\cdot)} &> 0 \text{ for positions located right (starboard) of the CoM (point R)} \\ Z_{P(\cdot)} &> 0 \text{ for positions located below of the CoM (point R)} \end{aligned}$$

3.2 Kinematic Relationships

It is essential to recall the distinguishing feature between a rotation tensor and a coordinate transformation. While a coordinate transformation relates to two coordinate systems, a rotation tensor describes the orientation of two frames. A rotation tensor is constructed from the angle and unit-vector of rotation (using the

Euler-Rodrigues formula), and, when expressed in one of the two preferred coordinate systems, it yields the transpose of the coordinate transformation matrix.

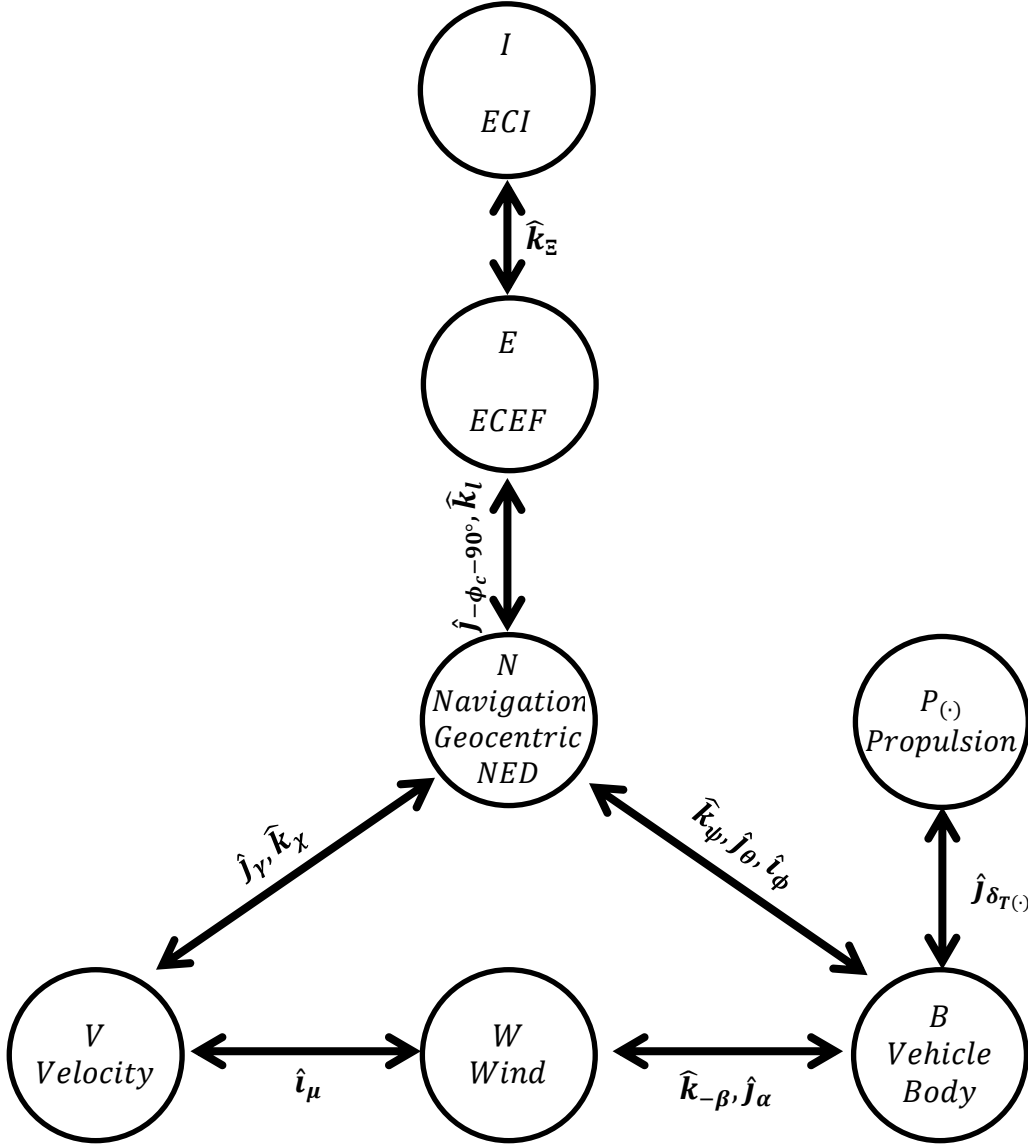


Figure 3.5. Orientation Angles Connecting All Frames and Coordinate Systems

Figure 3.5 summarizes the different frames and coordinate systems introduced earlier and depicts in the correct (defined) sequence, the orientation angles, and unit basis vectors of rotation that relate them to each other. General expressions for orthogonal rotation tensors, related to positive rotations (right-handed by Convention) in roll, pitch, yaw about each of the respective right-handed triad of

orthonormal basis vectors $\hat{i}, \hat{j}, \hat{k}$ of any frame through an arbitrary angle, are represented in a preferred coordinate system as;

$$\check{R}_{\hat{i}}(\cdot) = \begin{bmatrix} 1 & 0 & 0 \\ 0 & c_{(\cdot)} & -s_{(\cdot)} \\ 0 & s_{(\cdot)} & c_{(\cdot)} \end{bmatrix}, \check{R}_{\hat{j}}(\cdot) = \begin{bmatrix} c_{(\cdot)} & 0 & s_{(\cdot)} \\ 0 & 1 & 0 \\ -s_{(\cdot)} & 0 & c_{(\cdot)} \end{bmatrix}, \check{R}_{\hat{k}}(\cdot) = \begin{bmatrix} c_{(\cdot)} & -s_{(\cdot)} & 0 \\ s_{(\cdot)} & c_{(\cdot)} & 0 \\ 0 & 0 & 1 \end{bmatrix} \quad (60)$$

where $s_{(\cdot)}$ and $c_{(\cdot)}$ are shorthand notations for $\sin(\cdot)$ and $\cos(\cdot)$, respectively. Orthogonal transformations that connect all the coordinate systems associated with the frames in Figure 3.5 can now be derived from these expressions.

3.3 Coordinate Transformations

The transposed coordinate transformation matrices are obtained using the kinematic relationships, giving:

$$[\check{T}^{(E,I)}]^T = \check{T}^{(I,E)} = \check{R}_{\hat{k}}(\Xi) \quad (61)$$

$$[\check{T}^{(N,E)}]^T = \check{T}^{(E,N)} = \check{T}^{(E,E_1)}\check{T}^{(E_1,E_2)}\check{T}^{(E_2,N)} = \check{R}_{\hat{k}}(l)\check{R}_{\hat{j}}(-\phi_c)\check{R}_{\hat{j}}(-90^\circ) \quad (62)$$

$$[\check{T}^{(B,N)}]^T = \check{T}^{(N,B)} = \check{T}^{(N,N_1)}\check{T}^{(N_1,N_2)}\check{T}^{(N_2,B)} = \check{R}_{\hat{k}}(\psi)\check{R}_{\hat{j}}(\theta)\check{R}_{\hat{i}}(\phi) \quad (63)$$

$$[\check{T}^{(B,W)}]^T = \check{T}^{(W,B)} = \check{T}^{(W,S)}\check{T}^{(S,B)} = \check{R}_{\hat{k}}(-\beta)\check{R}_{\hat{j}}(\alpha) \quad (64)$$

$$[\check{T}^{(V,N)}]^T = \check{T}^{(N,V)} = \check{T}^{(N,X)}\check{T}^{(X,V)} = \check{R}_{\hat{k}}(\chi)\check{R}_{\hat{j}}(\gamma) \quad (65)$$

$$[\check{T}^{(W,V)}]^T = \check{T}^{(V,W)} = \check{R}_{\hat{i}}(\mu) \quad (66)$$

$$[\check{T}^{(P_{(\cdot)},B)}]^T = \check{T}^{(B,P_{(\cdot)})} = \check{R}_{\hat{j}}(\delta_{T_{(\cdot)}}) \quad (67)$$

Then we can obtain the matrices in the matrix form,

$$\check{T}^{(I,E)} = \check{R}_{\hat{k}}(\Xi) = \begin{bmatrix} c_{(\Xi)} & -s_{(\Xi)} & 0 \\ s_{(\Xi)} & c_{(\Xi)} & 0 \\ 0 & 0 & 1 \end{bmatrix} \quad (68)$$

$$\check{T}^{(E,N)} = \check{R}_{\hat{k}}(l)\check{R}_{\hat{j}}(-\phi_c)\check{R}_{\hat{j}}(-90^\circ) = \begin{bmatrix} -c_{(l)}s_{(\phi_c)} & -s_{(l)} & -c_{(l)}c_{(\phi_c)} \\ -s_{(l)}s_{(\phi_c)} & c_{(l)} & -s_{(l)}c_{(\phi_c)} \\ c_{(\phi_c)} & 0 & -s_{(\phi_c)} \end{bmatrix} \quad (69)$$

$$\check{T}^{(N,B)} = \check{R}_{\hat{k}}(\psi)\check{R}_{\hat{j}}(\theta)\check{R}_{\hat{i}}(\phi) = \begin{bmatrix} c_{(\psi)}c_{(\theta)} & -s_{(\psi)}c_{(\phi)} + c_{(\psi)}s_{(\theta)}s_{(\phi)} & s_{(\psi)}s_{(\phi)} + c_{(\psi)}s_{(\theta)}c_{(\phi)} \\ s_{(\psi)}c_{(\theta)} & c_{(\psi)}c_{(\phi)} + s_{(\psi)}s_{(\theta)}s_{(\phi)} & -c_{(\psi)}s_{(\phi)} + s_{(\psi)}s_{(\theta)}c_{(\phi)} \\ -s_{(\theta)} & c_{(\theta)}s_{(\phi)} & c_{(\theta)}c_{(\phi)} \end{bmatrix} \quad (70)$$

$$\check{T}^{(W,B)} = \check{R}_{\hat{k}}(-\beta)\check{R}_{\hat{j}}(\alpha) = \begin{bmatrix} c_{(\beta)}c_{(\alpha)} & s_{(\beta)} & c_{(\beta)}s_{(\alpha)} \\ -s_{(\beta)}c_{(\alpha)} & c_{(\beta)} & -s_{(\beta)}s_{(\alpha)} \\ -s_{(\alpha)} & 0 & c_{(\alpha)} \end{bmatrix} \quad (71)$$

$$\check{T}^{(N,V)} = \check{R}_{\hat{k}}(\chi)\check{R}_{\hat{j}}(\gamma) = \begin{bmatrix} c_{(\chi)}c_{(\gamma)} & -s_{(\chi)} & c_{(\chi)}s_{(\gamma)} \\ s_{(\chi)}c_{(\gamma)} & c_{(\chi)} & s_{(\chi)}s_{(\gamma)} \\ -s_{(\gamma)} & 0 & c_{(\gamma)} \end{bmatrix} \quad (72)$$

$$\check{T}^{(V,W)} = \check{R}_{\hat{i}}(\mu) = \begin{bmatrix} 1 & 0 & 0 \\ 0 & c_{(\mu)} & -s_{(\mu)} \\ 0 & s_{(\mu)} & c_{(\mu)} \end{bmatrix} \quad (73)$$

$$\check{T}^{(B,P_{(\cdot)})} = \check{R}_{\hat{j}}(\delta_{T(\cdot)}) = \begin{bmatrix} c_{(\delta_{T(\cdot)})} & 0 & s_{(\delta_{T(\cdot)})} \\ 0 & 1 & 0 \\ -s_{(\delta_{T(\cdot)})} & 0 & c_{(\delta_{T(\cdot)})} \end{bmatrix} \quad (74)$$

3.4 Angular Velocities and Angular Rates

Noting that angular velocity vectors relating one frame to another, consists of the vector addition of the angular rates times their respective unit vectors, the following equations are obtained using the previous kinematic relationships. These expressions can now be resolved in any desired coordinate system to derive useful relationships

$$\vec{\omega}^{E/I} = \dot{\hat{k}}_E \quad (75)$$

$$\vec{\omega}^{N/E} = \vec{\omega}^{N/E_2} + \vec{\omega}^{E_2/E_1} + \vec{\omega}^{E_1/E} = -\dot{\phi}_c \hat{j}_{E_2} + \dot{l} \hat{k}_{E_1} \quad (76)$$

$$\vec{\omega}^{B/N} = \vec{\omega}^{B/N_2} + \vec{\omega}^{N_2/N_1} + \vec{\omega}^{N_1/N} = \dot{\phi} \hat{i}_B + \dot{\theta} \hat{j}_{N_2} + \dot{\psi} \hat{k}_{N_1} \quad (77)$$

$$\vec{\omega}^{B/W} = \vec{\omega}^{B/S} + \vec{\omega}^{S/W} = \dot{\alpha} \hat{j}_B - \dot{\beta} \hat{k}_S \quad (78)$$

$$\vec{\omega}^{V/N} = \vec{\omega}^{V/X} + \vec{\omega}^{X/N} = \dot{\gamma} \hat{j}_V + \dot{\chi} \hat{k}_X \quad (79)$$

$$\vec{\omega}^{W/V} = \dot{\mu} \hat{i}_W \quad (80)$$

$$\vec{\omega}^{P_{(\cdot)}/B} = \dot{\delta}_{T(\cdot)} \hat{j}_{P_{(\cdot)}} \quad (81)$$

3.5 Equations of motion

The position and linear velocity of the vehicle's center of mass with respect to the earth-fixed frame are expressed as;

$$P_V^E = [P_{x_V}, P_{y_V}, P_{z_V}]^T, \quad \vec{V}_V^E = \dot{P}_{cg} = [V_{x_V}, V_{y_V}, V_{z_V}]^T \quad (82)$$

Euler angles and their time derivative in earth-fixed frame with respect to the earth-fixed frame are defined as;

$$\vec{\alpha}_E^E = [\phi, \theta, \psi]^T, \quad \vec{\omega}_E^E = \dot{\vec{\alpha}}_E^E = [\dot{\phi}, \dot{\theta}, \dot{\psi}]^T \quad (83)$$

The orientation of the body frame with respect to the vehicle carried frame (same as earth-fixed frame) is expressed by the rotation matrix;

$$L_{VB} = L_{BV}^T = \begin{bmatrix} C_\psi C_\theta & S_\phi S_\theta C_\psi - C_\phi S_\psi & C_\phi S_\theta C_\psi + S_\phi S_\psi \\ S_\psi C_\theta & S_\phi S_\theta S_\psi + C_\phi C_\psi & C_\phi S_\theta S_\psi - S_\phi C_\psi \\ -S_\theta & S_\phi C_\theta & C_\phi C_\theta \end{bmatrix} \quad (84)$$

Transformation of the linear velocities between the earth and the body frames is given as;

$$\vec{V}_V^E = \begin{bmatrix} V_{x_V} \\ V_{y_V} \\ V_{z_V} \end{bmatrix} = \begin{bmatrix} \dot{P}_{x_V} \\ \dot{P}_{y_V} \\ \dot{P}_{z_V} \end{bmatrix} = L_{VB} \vec{V}_B^E = L_{VB} \begin{bmatrix} V_{x_B} \\ V_{y_B} \\ V_{z_B} \end{bmatrix} = L_{VB} \begin{bmatrix} u \\ v \\ w \end{bmatrix} \quad (85)$$

The relation between the angular velocity of the vehicle and the time derivative of the Euler angles is given by the following relation;

$$\vec{\omega}_B^E = \begin{bmatrix} p \\ q \\ r \end{bmatrix} = R(\theta, \phi) \vec{\omega}_E^E = \begin{bmatrix} 1 & 0 & -S_\theta \\ 0 & C_\phi & S_\phi C_\theta \\ 0 & -S_\phi & C_\phi C_\theta \end{bmatrix} \begin{bmatrix} \dot{\phi} \\ \dot{\theta} \\ \dot{\psi} \end{bmatrix} \quad (86)$$

Since $R(\theta, \phi)$ is not a transformation matrix, inverse velocity calculations should be done using the inverse of the $R(\theta, \phi)$.

$$\vec{\omega}_V^E = R^{-1}(\theta, \phi) \vec{\omega}_B^E \quad (87)$$

Since the aerial vehicle is assumed as a rigid body, its dynamic can be written as;

$$\begin{bmatrix} F_t \\ M_t \end{bmatrix} \Big|_E = \begin{bmatrix} mI & 0 \\ 0 & I_B \end{bmatrix} \begin{bmatrix} \vec{V}_V^E \\ \vec{\omega}_B^E \end{bmatrix} + \begin{bmatrix} 0 \\ \vec{\omega}_B^E \end{bmatrix} \quad (88)$$

If we try to resolve the above equation into body coordinates,

$$\begin{bmatrix} F_t \\ M_t \end{bmatrix} \Big|_B = \vec{\omega}_B^E \times \begin{bmatrix} m\vec{V}_B^E & 0 \\ 0 & \vec{H}_B^E \end{bmatrix} + \begin{bmatrix} m\vec{V}_B^E \\ \vec{H}_B^E \end{bmatrix} \quad (89)$$

We can divide the equation into two equations. One should be the force; the other one will be moment equation,

$$\begin{bmatrix} X \\ Y \\ Z \end{bmatrix} + L_{BV} \begin{bmatrix} 0 \\ 0 \\ mg \end{bmatrix} = m. \left[\begin{bmatrix} \dot{u} \\ \dot{v} \\ \dot{w} \end{bmatrix} + \begin{bmatrix} p \\ q \\ r \end{bmatrix} \times \begin{bmatrix} u \\ v \\ w \end{bmatrix} \right] \quad (90)$$

$$\begin{bmatrix} L \\ M \\ N \end{bmatrix} = I_B \begin{bmatrix} \dot{p} \\ \dot{q} \\ \dot{r} \end{bmatrix} + \left[\begin{bmatrix} p \\ q \\ r \end{bmatrix} \times \begin{bmatrix} p \\ q \\ r \end{bmatrix} \right] \quad (91)$$

If we arrange two equations given above and put them together with the two equations found in the first part,

$$\begin{bmatrix} \dot{u} \\ \dot{v} \\ \dot{w} \end{bmatrix} = \begin{bmatrix} p \\ q \\ r \end{bmatrix} \times \begin{bmatrix} u \\ v \\ w \end{bmatrix} + \begin{bmatrix} -gS_\theta \\ gS_\phi C_\theta \\ gC_\phi C_\theta \end{bmatrix} + \frac{1}{m} \begin{bmatrix} X \\ Y \\ Z \end{bmatrix} \quad (92)$$

$$\begin{bmatrix} \dot{p} \\ \dot{q} \\ \dot{r} \end{bmatrix} = -I_B^{-1} \left[\begin{bmatrix} p \\ q \\ r \end{bmatrix} \times \begin{bmatrix} p \\ q \\ r \end{bmatrix} \right] + I_B^{-1} \begin{bmatrix} L \\ M \\ N \end{bmatrix} \quad (93)$$

$$\begin{bmatrix} \dot{\phi} \\ \dot{\theta} \\ \dot{\psi} \end{bmatrix} = \begin{bmatrix} 1 & S_\phi T_\theta & C_\phi T_\theta \\ 0 & C_\phi & -S_\phi \\ 0 & S_\phi Sec_\theta & C_\phi Sec_\theta \end{bmatrix} \begin{bmatrix} p \\ q \\ r \end{bmatrix} \quad (94)$$

$$\begin{bmatrix} \dot{P}_{x_V} \\ \dot{P}_{y_V} \\ \dot{P}_{z_V} \end{bmatrix} = \begin{bmatrix} C_\psi C_\theta & S_\phi S_\theta C_\psi - C_\phi S_\psi & C_\phi S_\theta C_\psi + S_\phi S_\psi \\ S_\psi C_\theta & S_\phi S_\theta S_\psi + C_\phi C_\psi & C_\phi S_\theta S_\psi - S_\phi C_\psi \\ -S_\theta & S_\phi C_\theta & C_\phi C_\theta \end{bmatrix} \begin{bmatrix} u \\ v \\ w \end{bmatrix} \quad (95)$$

Now we have twelve equations and twelve states written in the state space format. These equations will be used in the state space model.

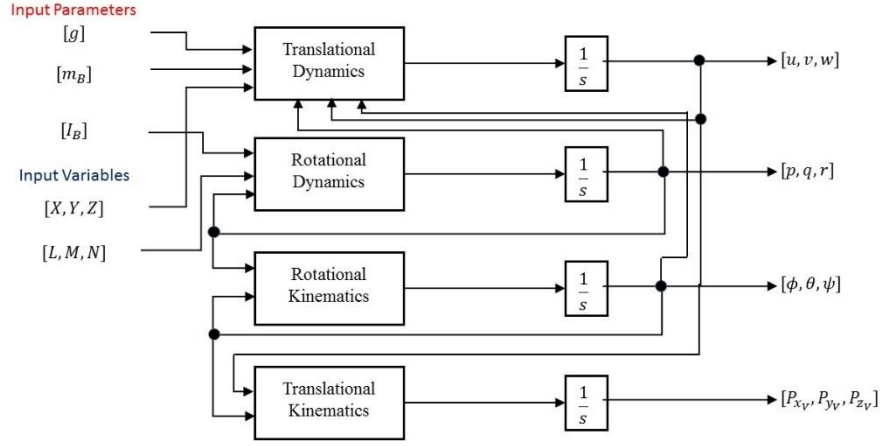


Figure 3.6. Dynamic and Kinematic Relations between inputs and states

3.6 Equations of motion

Mass, the center of gravity, and inertia tensor are taken from the CATIA model. The tilt-wing mechanism tilts the wing from the centerline of the wing spar. The center of gravity of the wing is also placed in the same position. Since the rotation line and center of gravity of the wing fall into the same line, the inertia of the whole body will not change during the transition phase. This feature will help us to eliminate the risk of having a time-variant system.

$$m = 9.464 \text{ kg} \quad (96)$$

$$G = \begin{bmatrix} -0.00013 \\ -0.07 \\ 0.00022 \end{bmatrix} \text{ mm} \quad (97)$$

$$I_B = \begin{bmatrix} 2.34 & 0 & 0 \\ 0 & 1.4 & 0 \\ 0 & 0 & 3.7 \end{bmatrix} \text{ kg.m}^2 \quad (98)$$

3.7 Forces and Moments

We can separate forces and moments as aerodynamics and thrust generated. We have already transformed the aerodynamic forces into body coordinates in Chapter 2. We should also transform the thrust forces and moments into body coordinates using a related transformation matrix for VTOL and transition mode.

$$F_{net} = \begin{bmatrix} X \\ Y \\ Z \end{bmatrix} + \tilde{T}^{(B,P)} \begin{bmatrix} F_{Prop} \\ 0 \\ 0 \end{bmatrix} \quad (99)$$

$$M_{net} = \begin{bmatrix} L \\ M \\ N \end{bmatrix} + \tilde{T}^{(B,P)} \begin{bmatrix} L_{Prop} \\ M_{Prop} \\ N_{Prop} \end{bmatrix} \quad (100)$$

There are three flight modes, which are VTOL, Transition, and Forward Flight. We should write the thrust forces and moments which are valid for all modes.

$$\begin{bmatrix} X \\ Y \\ Z \end{bmatrix} = \begin{bmatrix} \bar{q} S C_X \\ \bar{q} S C_Y \\ \bar{q} S C_Z \end{bmatrix} \quad (101)$$

$$\begin{bmatrix} L \\ M \\ N \end{bmatrix} = \begin{bmatrix} \bar{q} S b C_l \\ \bar{q} S \bar{c} C_m \\ \bar{q} S b C_n \end{bmatrix} \quad (102)$$

$$C_X = -c_{(\alpha)} c_{(\beta)} C_D + c_{(\alpha)} s_{(\beta)} C_C + s_{(\alpha)} C_L \quad (103)$$

$$C_Y = -s_{(\beta)} C_D - c_{(\beta)} C_C \quad (104)$$

$$C_Z = -s_{(\alpha)} c_{(\beta)} C_D + s_{(\alpha)} s_{(\beta)} C_C - c_{(\alpha)} C_L \quad (105)$$

To ensure the commonality for all flight modes, we will take the Angle of Attack of the wing as the baseline since the primary lift provider is the wing.

During the forward flight, the angle between the wing and the body will be zero. Then forward flight equation can be arranged as;

$$F_{net} = \begin{bmatrix} X \\ Y \\ Z \end{bmatrix} + \begin{bmatrix} F_{Prop} \\ 0 \\ 0 \end{bmatrix} \quad (106)$$

$$M_{net} = \begin{bmatrix} L \\ M \\ N \end{bmatrix} + \begin{bmatrix} 0 \\ 0 \\ N_{Prop} \end{bmatrix} \quad (107)$$

Aerodynamic forces and moments in the forward flight can be approximated as;

$$\begin{bmatrix} X \\ Y \\ Z \end{bmatrix} = \begin{bmatrix} \bar{q}S \left(\bar{C}_X + C_{X_q}q + C_{X_{d_e}}d_e + C_{X_{d_a}}d_a \right) \\ \bar{q}S \left(\bar{C}_Y + C_{Y_r}r + C_{Y_p}p + C_{Y_{d_e}}d_e + C_{Y_{d_a}}d_a \right) \\ \bar{q}S \left(\bar{C}_Z + C_{Z_q}q + C_{Z_{\dot{\alpha}}}\dot{\alpha} + C_{Z_{d_e}}d_e + C_{Z_{d_a}}d_a \right) \end{bmatrix} \quad (108)$$

$$\begin{bmatrix} L \\ M \\ N \end{bmatrix} = \begin{bmatrix} \bar{q}Sb \left(\bar{C}_l + C_{l_p}p + C_{l_r}r + C_{l_{d_e}}d_e + C_{l_{d_a}}d_a \right) \\ \bar{q}S\bar{c} \left(\bar{C}_m + C_{m_q}q + C_{m_{\dot{\alpha}}}\dot{\alpha} + C_{m_{d_e}}d_e + C_{m_{d_a}}d_a \right) \\ \bar{q}Sb \left(\bar{C}_n + C_{n_r}r + C_{n_p}p + C_{n_{d_e}}d_e + C_{n_{d_a}}d_a \right) \end{bmatrix} \quad (109)$$

We have found the damping derivatives in Chapter 2. Control Surfaces force and moment coefficients can be seen on the following table;

Table 3.2 Aerodynamic Damping Derivatives

$C_{X_{d_a}}$	$-0.3s(\alpha)$	$C_{X_{d_e}}$	$0.33s(\alpha)$
$C_{Y_{d_a}}$	0	$C_{Y_{d_e}}$	0
$C_{Z_{d_a}}$	$0.3c(\alpha)$	$C_{Z_{d_e}}$	$-0.33c(\alpha)$
$C_{l_{d_a}}$	0.2	$C_{l_{d_e}}$	0
$C_{m_{d_a}}$	0.137	$C_{m_{d_e}}$	-0.93
$C_{n_{d_a}}$	0	$C_{n_{d_e}}$	0

We can write down damping derivatives in the forces and moment equations;

$$\begin{bmatrix} X \\ Y \\ Z \end{bmatrix} = \begin{bmatrix} \bar{q}S(\bar{C}_X) \\ \bar{q}S(\bar{C}_Y) \\ \bar{q}S(\bar{C}_Z - 9.93 * a * q - 0.53 * a * \dot{\alpha} - 0.33d_e + 0.3d_a) \end{bmatrix} \quad (110)$$

$$\begin{bmatrix} L \\ M \\ N \end{bmatrix} = \begin{bmatrix} \bar{q}Sb(\bar{C}_l - 0.28p + 1.48 * a * r + 0.2d_a) \\ \bar{q}S\bar{c}(\bar{C}_m - 17q - 2.4\dot{\alpha} - 0.93d_e + 0.137d_a) \\ \bar{q}Sb(\bar{C}_n - 0.50 * a^2r - 0.4p) \end{bmatrix} \quad (111)$$

We can simplify the above equations by approximating some variables as zero;

$$\begin{bmatrix} X \\ Y \\ Z \end{bmatrix} = \begin{bmatrix} \bar{q}S(\bar{C}_X) \\ \bar{q}S(\bar{C}_Y) \\ \bar{q}S(\bar{C}_Z - 0.33d_e + 0.3d_a) \end{bmatrix} \quad (112)$$

$$\begin{bmatrix} L \\ M \\ N \end{bmatrix} = \begin{bmatrix} \bar{q}Sb(\bar{C}_l - 0.28p + 0.2d_a) \\ \bar{q}S\bar{c}(\bar{C}_m - 17q - 2.4\dot{\alpha} - 0.93d_e + 0.137d_a) \\ \bar{q}Sb(\bar{C}_n - 0.4p) \end{bmatrix} \quad (113)$$

3.8 Non-Linear Model

The non-linear model, which has been created in the MATLAB/Simulink environment, includes the pilot block, controller, plant model, sensor block, and disturbance model. On the other hand, the plant model has been created in MATLAB/Simulink/Simscape. The sensor data has been obtained from the related Simscape blocks. However, raw data sent from Simscape blocks are processed in the sensor block using related transformation functions.

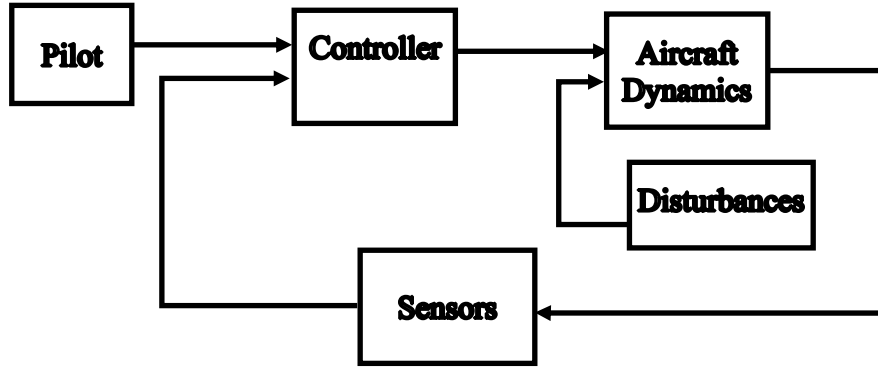


Figure 3.7. Nonlinear Model

3.8.1 Pilot Model

The pilot model has mainly two parts; in the first block, the pilot gives commands to aircraft while in the second one, he can monitor the critical indicators such as states, motor RPMs, control surface deflections.

In this block, four commands can be given by the pilot. The pilot can give mode command from one to five. Mode 1 means that aircraft will climb in VTOL mode. Mode 2 means there will be a transition from vertical flight to forward flight. Mode 3 represents the forward flight, where Mode 4 represents the transition from forward flight to hover. Finally, Mode 5 means that the aircraft will descend in VTOL mode.

The second command, which the pilot can give from this block, is the Roll Command. Roll command should be given in the Mode 3. When the pilot gives the roll command, the aircraft will start a coordinated turn. Until the aircraft is achieved the desired yaw angle, aircraft will turn.

The third command is the Yaw Command. Small Yaw Commands can be directly given by this block, while the high Yaw Angle Commands should be given using the Roll Command. If the pilot uses the roll command, he should enter the desired yaw angle to yaw command block, too. When the aircraft achieved the desired yaw angle, the pilot should turn the roll command into zero. Aircraft will make small adjustments to go to the desired yaw angle.

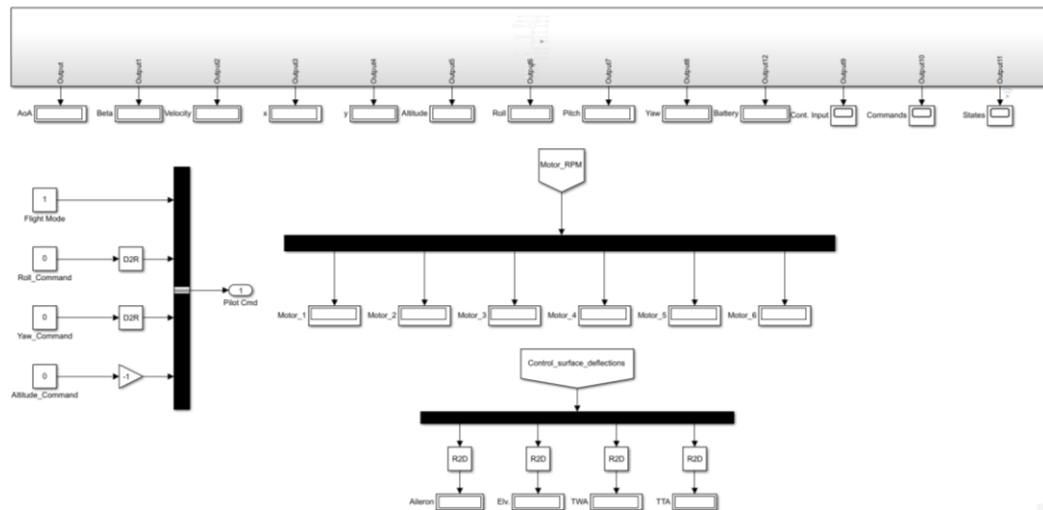


Figure 3.8. Pilot Block

3.8.2 Controller

The controller accepts pilot commands and sensor outputs as inputs and sends control commands as the outputs. There are two kinds of approaches for the controller; in one type, controller outputs go directly to control surfaces. In contrast, the other type includes the mixer, which connects the controller outputs and the control surfaces inputs.

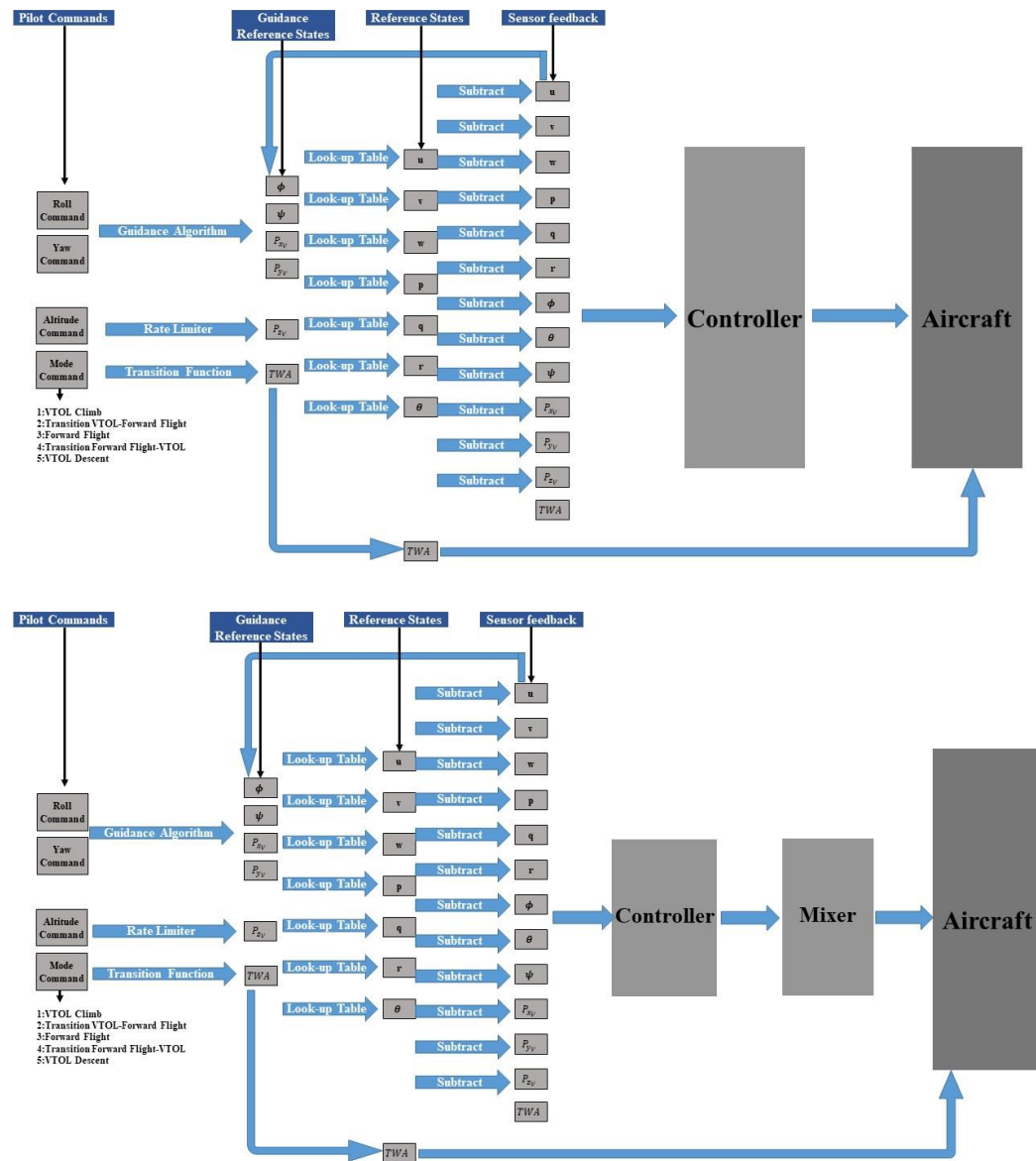


Figure 3.9. Controller Block

3.8.3 Plant Model

The plant model has four main parts. These are the world block, 6 DoF Joint, 3D CAD model of the aircraft, and the forces and moments generated by the aircraft.

The world is represented by a Simscape block, which can simulate gravitational acceleration. The aircraft 3D CAD model is connected to the world block by using a 6 DoF Joint, which is also a function of the Simscape. The 3D CAD model has its own degrees of freedom, such as rotors, control surface deflections. Forces and moments blocks are generating force and moments according to the control surface deflection, motor RPMs, dynamic pressure. The Plant Model blocks have a connection with the Mechanics Explorer, which enables us to see the aircraft movements in a 3D environment.

There are Lookup Tables that are embedded in the force and moment blocks. These look-up tables are generated using the CFD Database. CFD database gives us the static coefficients while the dynamic coefficients are calculated using the related equations in Roskam.

Thrust forces and moments are also included in the forces and moments block. They are also calculated using the Look-up tables. The manufacturer provides the values used in the look-up tables.

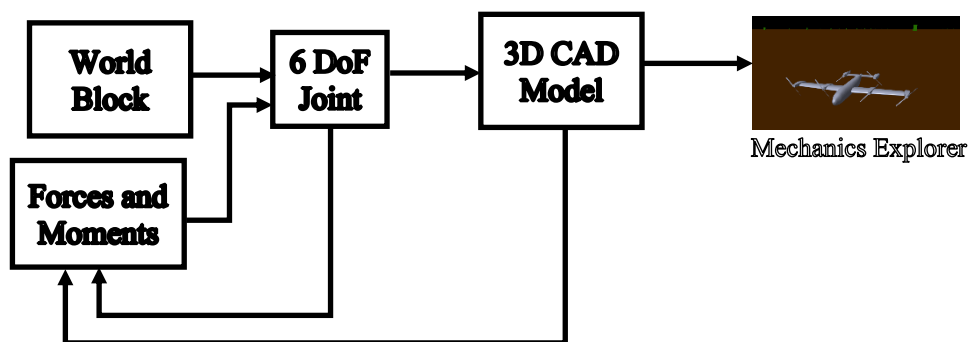


Figure 3.10. Plant Model

3D CAD model of the aircraft includes six motor actuators, one aileron actuator, and one elevator actuator. The upper and lower limits of these actuators and tilting mechanisms are tabulated in Table 3.3.

Table 3.3 Upper and Lower Limits of the Actuators

Actuator	Lower Limit	Upper Limit
Front Right Tip Motor	0 RPM	5462 RPM
Front Right Root Motor	0 RPM	5462 RPM
Front Left Root Motor	0 RPM	5462 RPM
Front Left Tip Motor	0 RPM	5462 RPM
Rear Right Motor	0 RPM	8842 RPM
Rear Left Motor	0 RPM	8842 RPM
Aileron	-30 deg	+30 deg
Elevator	-30 deg	+30 deg
Tilt-Wing	0 deg	90 deg
Tilt-Tail	0 deg	90 deg

Actuator dynamics is a crucial factor for a non-linear model to be a good representative of the real plant. Therefore, typical actuator transient responses have been implemented for the non-linear model. This response is represented using a transfer function given in Eq. 114, note that the transient response of the actuators is normalized. Normalized transient responses are amplified with the related coefficients before sending them to the sensor model. The step input response of the transfer function can be seen in Figure 3.11.

$$G(s) = \frac{1}{0.02s + 1} \quad (114)$$

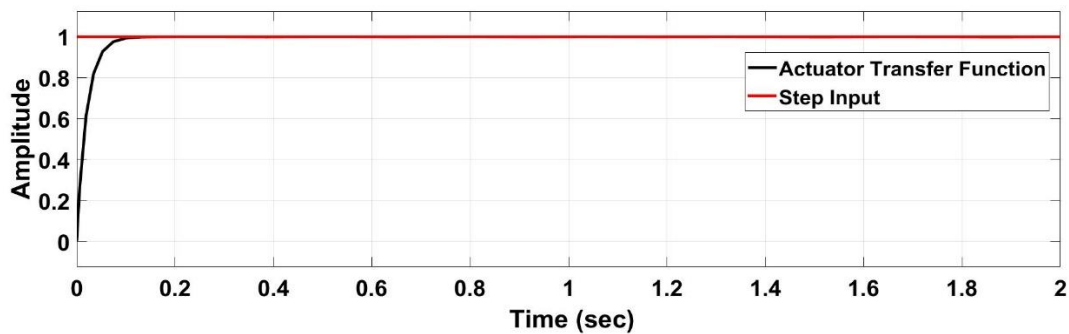


Figure 3.11. Transient Response of the Actuators

For tilt-wing and tilt-tail dynamics, non-linear second order actuator models have been employed, which has 10 rad/s natural frequency and 0.3 damping ratio. Step input responses of the tilting mechanisms can be seen in Figure 3.12.

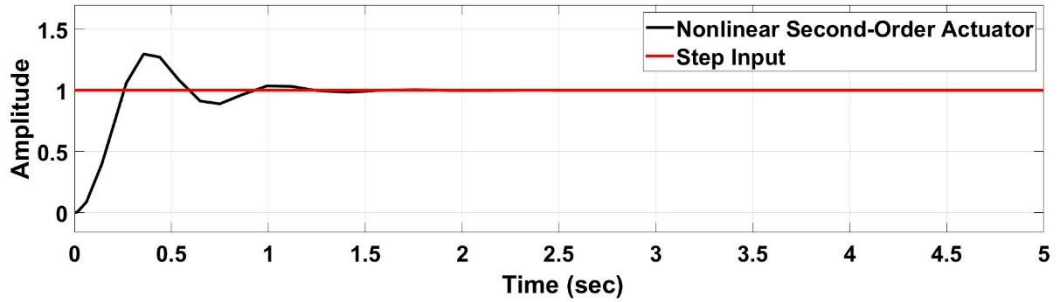


Figure 3.12. Transient Response of the Tilting Mechanisms

3.8.4 Disturbance Model

The disturbance model accepts altitude, airspeed, and direction cosine matrix as inputs and generates random wind gusts in three axes using the Dryden Wind Turbulence Model. The wind gusts generated in this block are sent to the sensor block, and sensor block changes angle of attack and sideslip angle using the gusts. When the angle of attack and sideslip angle changes, related forces and moments which affect the aircraft dynamics are generated in the plant model.

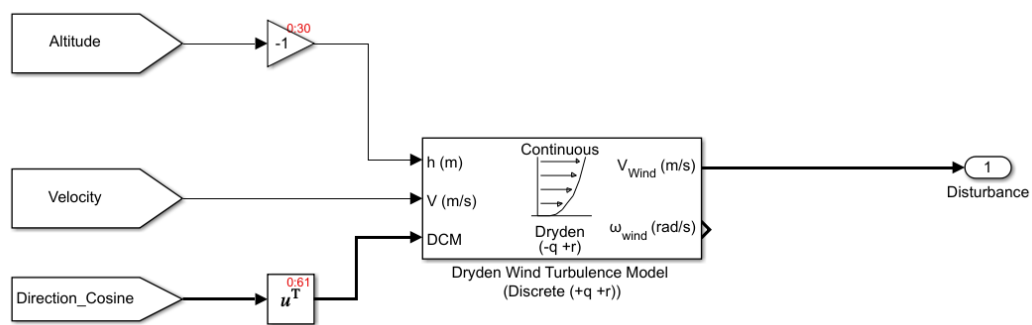


Figure 3.13. Disturbance Model

The disturbance sent by this block can be manipulated by changing the wind speed and wind direction. As the wind speed increases, the gusts' amplitudes also increase.

If the wind direction is changed, the intensity of the gust for different axis will be changed.

3.8.5 Sensor Model

The sensor model accepts the position, velocity, Euler angles, Angular velocities in inertial coordinates, control surface deflections, Motor RPMs in body-fixed coordinates. After that, it converts them into the body coordinates using the transformation matrices then sends the states as outputs. Disturbances cause additional forces and moments on aircraft depending on aerodynamic characteristics of the aircraft. In the sensor block, body velocity, propeller slipstream velocity, and the additional velocity coming from the disturbances in three axes are sum up. The velocity vector formed by body velocity, propeller slipstream velocity, and the disturbances is used to calculate the angle of attack, sideslip angle, and the total velocity in this block. Additional forces and moments are generated on aircraft in each step of the simulation if the disturbances are turned on. Because of this reason, the disturbances are applied to sensor block instead of the plant model itself. We can say that disturbance forces and moments are applied to aircraft indirectly.

CHAPTER 4

LINEAR ANALYSIS

In this chapter, the linear analysis process of the system has been discussed. Trimming, linearization, and stability are three aspects that make up the general flight characteristics of an aircraft. Trimming refers to find the equilibrium points about which the linearization of the relevant nonlinear equations is done. The linearization is done to determine the stability characteristics of the system. After the linearization process, controllers are designed by using the stability characteristics of the system, which is found in the linearization process.

Stability analysis requires linearization about a trim point and examination of the eigenvalues and eigenvectors of the system. This is useful when examining the system responses to step inputs or finding the frequency response of the system in case of disturbances. The primary assumption underlying in the stability and trim analysis is that the higher-order rotor and inflow dynamics are much faster than the fuselage motions and have time to reach their steady-state well within the typical time constants of the aircraft's response modes [2]. In this study, linear analysis has been performed based on the body axes since the wind axis or stability axis, losing their importance during hover. Another issue is that the inertial measurement unit gives the output in the body axis. Therefore the body axis will be employed in the linear analysis.

Throughout the chapter, trimming methods are explained, and how the trim points of the system are found will be discussed. The trim points that are found in this chapter are used in linear model analysis and controller design in the next chapter.

4.1 Trimming Methodology

Flight can be defined as the movement in the air with the balance of the aerodynamic, inertial, and gravitational forces and moments about three mutually perpendicular axes at all times. The trim condition is satisfied when this balance is achieved. The trim can be defined as the equilibrium point, where the rates of the aerodynamic state variables are zero.

The trim problem deals with the determination of control commands $u_x, u_y, u_z, u_{roll}, u_{pitch}, u_{yaw}$ which map to control elements' variables $\delta_e, \delta_a, \delta_{th1}, \delta_{th2}, \delta_{th3}, \delta_{th4}$ and the states that are required to hold the aircraft in equilibrium. The controller decides how much forces and moments are needed for the desired flight and a scheduler, which knows how much additional force and moment will be provided when control elements are deflected, decides which control elements should be deflected. Since the trim is an aerodynamical equilibrium, the derivatives of the states are set to zero except for ψ since it is used as a variable in turning flight.

MATLAB/Simulink-Linear Analysis Toolbox has been used for the trimming. "Gradient Descent Method with elimination" optimization method is used with an "active set algorithm." Gradient Descent methods involve an iterative moving in the direction of steepest descent as defined by the negative of the gradient. In the gradient descent method, the sum of the squared errors is reduced by updating the parameters in the direction of the greatest reduction of the least-squares objective. The active set algorithm strategy is related to the Karush-Kuhn-Tucker (KKT) equations. The KKT equations are necessary conditions for optimality for a constrained optimization problem. The strategy includes these steps; Updating Hessian Matrix, Quadratic Program Solution, initialization, line search, and merit function. The number of iterations, function evaluations, parameters, and function tolerances are all selectable to reach the required equilibrium states, inputs, and outputs.

In trimmed flight, the following rates are defined to be zero, and control elements are defined as constant. The trim methodology may be defined as an optimization problem given below:

$$\begin{aligned} & \underset{x, u}{\text{minimize}} \quad \|\dot{x}\| \end{aligned} \quad (115)$$

$$\begin{aligned} & \text{subject to } \dot{x} = f(x, u) \\ & \quad -1 \leq \delta_e, \delta_a \leq 1 \\ & \quad 0 \leq \delta_{th1}, \delta_{th2} \leq 1 \\ & \quad 0 \leq \delta_{th3}, \delta_{th4} \leq 1 \end{aligned} \quad (116)$$

$$\begin{aligned} & \text{where } x = [u, v, w, p, q, r, \phi, \theta, \psi, P_{z_v}] \text{ for hover, transition and cruise} \\ & \quad x = [u, v, w, p, q, r, \phi, \theta, P_{z_v}] \text{ for coordinated turn} \\ & \quad u = [\delta_e, \delta_a, \delta_{th1}, \delta_{th2}, \delta_{th3}, \delta_{th4}] \\ & \quad f(x, u) \text{ is the equations of motion} \end{aligned} \quad (117)$$

Seven Linear Models are generated for trimming. These models include the aircraft plant model and sensor block (Figure 4.1). In linear models, aerodynamic surfaces and propellers do not have a degree of freedom to have a stick fixed open loop system. Connections of these surfaces are cut from the Aerodynamic and Thrust forces and moments block. Instead of a degree of freedom, an input block has been placed (Figure 4.1). The linear analysis toolbox has the capability to make small adjustments on these input blocks to find the equilibrium points. States are defined as output blocks, which means that in every iteration linear analysis toolbox will give a small increment to the input and look to the outputs if they fit the target values or not.

The dynamics of the actuators are not included in the linear models. It is assumed that the position of the aileron and elevator actuators' and the angular velocity of the propellers at a certain tilt angle is always constant for the linear models. Therefore, there is no need to add a transient response for actuators for linear models. This assumption is valid for stick fixed open-loop system analysis. However, in the non-linear model, the actuator transient responses are included.

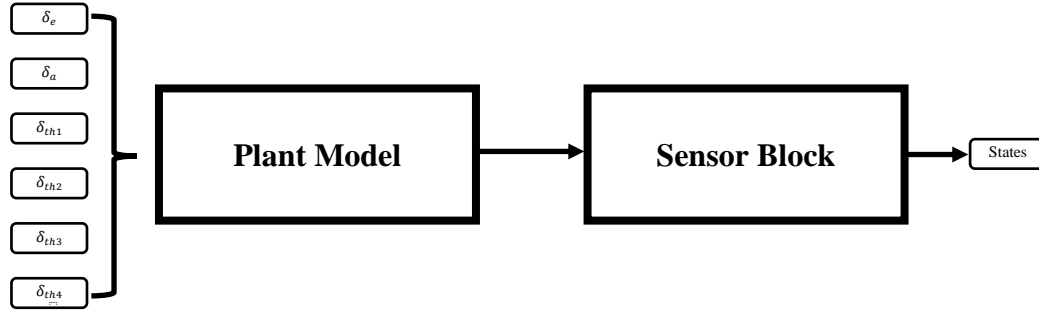


Figure 4.1. Linear Model for Trimming

Each linear model has its boundaries and initial conditions. In VTOL flight, aircraft vertical velocity can be changed from -5 to 5 m/s, while horizontal velocity is limited between -0.05 to 0.05 m/s, which means that linear analysis toolbox will try to fit vertical and horizontal velocities in these values. In forward flight horizontal velocity is approximated as between 15-25 m/s, and in vertical flight can be between -1 m/s and 1 m/s. Note that these values are in body coordinates.

There may be more than one trim condition for each linear model. However, the linear analysis toolbox will give us the first trim point where it finds a feasible solution that satisfies all constraints.

4.1.1 Trim Results

After the iterative process, the trimming results are obtained with maximum error in the order of 10^{-6} . There are eight trimmed conditions in total, of which one is for hover, five are for transition, one is for level flight, one is for the coordinated turn. For hover, the aircraft has a zero velocity in trim, whereas for forward flight and transition, the trim results are presented for different velocities. The results are shown in Table 4.1.

Trim results show that during hover, there is sufficient excess power for throttle inputs; however, there is no excess power of the elevator, which leads us to use flaps as body x-axes control input. During the transition, at high tilt angles, thrust forces

dominate the control authority, while aerodynamic forces are dominating the authority at low tilt angles.

Table 4.1 Inputs Variation During Transition

Tilt Angle (deg)	δ_{th-f} (%)	δ_{th-r} (%)	δ_{alrn} (deg)	δ_{elv} (deg)	u (m/s)	v (m/s)	w (m/s)	θ (deg)	ϕ (deg)	r (deg/s)
90	0.854	0.781	-17	-26.47	0	0	0	0	0	0
75	0.814	0.714	0	-9.56	2.17	0	-0.218	-5.72	0	0
60	0.776	0.572	0	-10.88	3.22	0	0.0007	0	0	0
45	0.692	0.323	0	-27.73	5.42	0	-0.008	-0.093	0	0
30	0.543	0	0	-25.32	7.82	0	-0.78	-5.72	0	0
15	0.472	0	0	-20.85	9.79	0	0	0	0	0
0	0.4265	0	0	-0.47	16.1	0	0	0	0	0
0(Turn)	0.47/0.467	0	1.97	-30	14.8	5	-0.105	3.52	12	5.15

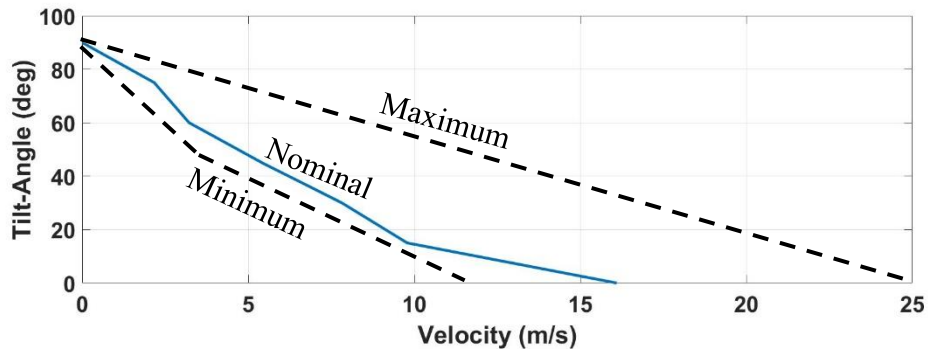


Figure 4.2. Velocity Changes with respect to Tilt-Angle

The trimming results are highly dependent on the target states' values that we have entered the optimization program. For instance, since we have selected yaw rate as 5 deg/s during the coordinated turn, trim results converged on a point that can be seen in Table 4.1. However, if another yaw rate had been chosen, roll angle and body velocities would have converged on different values. All trim points aim to have a smooth transition between vertical flight to horizontal flight or vice versa. Therefore, airspeed should have a smooth transition from zero to cruise speed. Pitch angle can be selected whatever optimization gives unless it is in the stall region. It should be noted that actuator inputs should have a smooth transition as well to hinder the transient response while passing from one trim point to another.

4.2 Linearization

In general, the equations of motions are nonlinear. Since linear controllers will be designed under this study, non-linear equations of motions should be linearized around trim points. While linearizing the nonlinear model, MATLAB/Simulink Linear Analyses Toolbox has been used. As part of this study, nine models, of which eight are linear, and one is nonlinear, has been prepared in Simulink.

The inputs presented in Table 4.1 and the outputs determined as states of the models are used for the analysis. Numerical perturbation has been employed as a linearization algorithm. After defining the algorithm type, ‘linearize’ command is used to linearize the system around the trim points. The classical Taylor series approach has been used by the toolbox. A continuous-time linearized state-space model has been obtained after linearizing the 6 DoF equations of motion.

$$\dot{x} = f(x, u) \quad (118)$$

$$y = g(x, u) \quad (119)$$

$$A = \frac{\partial f}{\partial x} \Big|_{(x_0, u_0)} = \begin{bmatrix} \frac{\partial f_1}{\partial x_1} \Big|_{(x_0, u_0)} & \dots & \frac{\partial f_1}{\partial x_n} \Big|_{(x_0, u_0)} \\ \vdots & \ddots & \vdots \\ \frac{\partial f_n}{\partial x_1} \Big|_{(x_0, u_0)} & \dots & \frac{\partial f_n}{\partial x_n} \Big|_{(x_0, u_0)} \end{bmatrix} \quad (120)$$

$$B = \frac{\partial f}{\partial u} \Big|_{(x_0, u_0)} = \begin{bmatrix} \frac{\partial f_1}{\partial u_1} \Big|_{(x_0, u_0)} & \dots & \frac{\partial f_1}{\partial u_m} \Big|_{(x_0, u_0)} \\ \vdots & \ddots & \vdots \\ \frac{\partial f_m}{\partial u_1} \Big|_{(x_0, u_0)} & \dots & \frac{\partial f_m}{\partial u_m} \Big|_{(x_0, u_0)} \end{bmatrix} \quad (121)$$

$$C = \frac{\partial g}{\partial x} \Big|_{(x_0, u_0)} = \begin{bmatrix} \frac{\partial g_1}{\partial x_1} \Big|_{(x_0, u_0)} & \dots & \frac{\partial g_1}{\partial x_n} \Big|_{(x_0, u_0)} \\ \vdots & \ddots & \vdots \\ \frac{\partial g_n}{\partial x_1} \Big|_{(x_0, u_0)} & \dots & \frac{\partial g_n}{\partial x_n} \Big|_{(x_0, u_0)} \end{bmatrix} \quad (122)$$

$$D = \frac{\partial g}{\partial u} \Big|_{(x_0, u_0)} = \begin{bmatrix} \frac{\partial g_1}{\partial u_1} \Big|_{(x_0, u_0)} & \dots & \frac{\partial g_1}{\partial u_m} \Big|_{(x_0, u_0)} \\ \vdots & \ddots & \vdots \\ \frac{\partial g_m}{\partial u_1} \Big|_{(x_0, u_0)} & \dots & \frac{\partial g_m}{\partial u_m} \Big|_{(x_0, u_0)} \end{bmatrix} \quad (123)$$

$$\Delta \dot{\mathbf{x}} = \mathbf{A} \Delta \mathbf{x} + \mathbf{B} \Delta \mathbf{u} \quad (124)$$

$$\Delta \mathbf{y} = \mathbf{C} \Delta \mathbf{x} + \mathbf{D} \Delta \mathbf{u} \quad (125)$$

State-space matrices of the system obtained from the Simulink Linear Analysis Toolbox can be found in Appendix B.

4.3 Open Loop Stability

In the sense of Lyapunov, stability assessment of the system has been performed. A Lyapunov approach is a general approach that can be employed for linear time-invariant dynamical systems for stability assessment. According to this approach:

- The system is stable if and only if all of the eigenvalues of A matrix have non-positive real parts, and those with zero real parts are distinct roots of the minimal polynomial of A .
- Asymptotically stable, if and only if all of the eigenvalues of A matrix have negative real parts.

For each trim condition, eigenvalues are found and represented in Eq. 126. For the hover case, open-loop aircraft is unstable. For level flight aircraft is stable in the longitudinal axis; however, for the lateral-directional axes, aircraft is unstable due to not having a vertical stabilizer. This instability will be tried to overcome with active asymmetric thrust control.

$$\begin{aligned}
eig(A_{TWA=0^\circ}) &= \begin{bmatrix} -417 \\ -29.65 \\ -5.57 \\ -1.29 \\ -0.32 \\ -0.0042 \\ -0.0139 \\ 1.2278 \\ 0.0036 \\ 0 \\ 0 \\ 0 \end{bmatrix} & eig(A_{Turn}) &= \begin{bmatrix} -379 \\ -32.03 \\ -4.98 \\ -0.92 \\ -0.4 \\ -0.01 + 0.04i \\ -0.01 - 0.04i \\ -0.003 \\ 1.29 \\ 0 \\ 0 \\ 0 \end{bmatrix} \\
eig(A_{TWA=15^\circ}) &= \begin{bmatrix} -219.91 \\ -15.31 \\ -2.04 \\ -0.43 + 0.42i \\ -0.43 - 0.42i \\ -0.42 \\ -0.05 \\ 0.14 \\ 0 \\ 0 \\ 0 \\ 0 \end{bmatrix} & eig(A_{TWA=30^\circ}) &= \begin{bmatrix} -176.09 \\ -9.44 \\ -1.83 \\ -0.71 + 0.80i \\ -0.71 - 0.80i \\ -0.36 \\ -0.05 \\ 0.19 \\ 0 \\ 0 \\ 0 \\ 0 \end{bmatrix} \\
eig(A_{TWA=45^\circ}) &= \begin{bmatrix} -133.65 \\ -9.19 \\ -0.95 + 0.67i \\ -0.95 - 0.67i \\ -1.09 \\ -0.27 \\ -0.13 \\ 0.30 \\ 0 \\ 0 \\ 0 \\ 0 \end{bmatrix} & eig(A_{TWA=60^\circ}) &= \begin{bmatrix} -93.75 \\ -6.4978 \\ -0.73 + 1.1i \\ -0.73 - 1.1i \\ -1.08 \\ -0.021 \\ -0.32 \\ 0.64 \\ 0.0007 \\ 0 \\ 0 \\ 0 \end{bmatrix} \\
eig(A_{TWA=75^\circ}) &= \begin{bmatrix} -79.6928 \\ -4.57 \\ -0.65 + 1.48i \\ -0.65 - 1.48i \\ -0.93 \\ -0.003 \\ -0.35 \\ 0.94 \\ 0.001 \\ 0 \\ 0 \\ 0 \end{bmatrix} & eig(A_{TWA=90^\circ}) &= \begin{bmatrix} -67.9 \\ -1.40 \\ -0.28 \\ -0.16 \\ -0.0035 \\ -0.035 \\ 0.108 + 0.22i \\ 0.108 - 0.22i \\ 0.0035 \\ 0 \\ 0 \\ 0 \end{bmatrix}
\end{aligned} \tag{126}$$

The impulse response of the system during hover and the forward flight has been illustrated in Figures 4.3 and 4.4. Only, the longitudinal axis in forward flight rejects the disturbance, while others diverge. The lateral-directional axes are always unstable since the aircraft does not have a vertical stabilizer. However, the closed-loop system should be stable during the whole flight envelope.

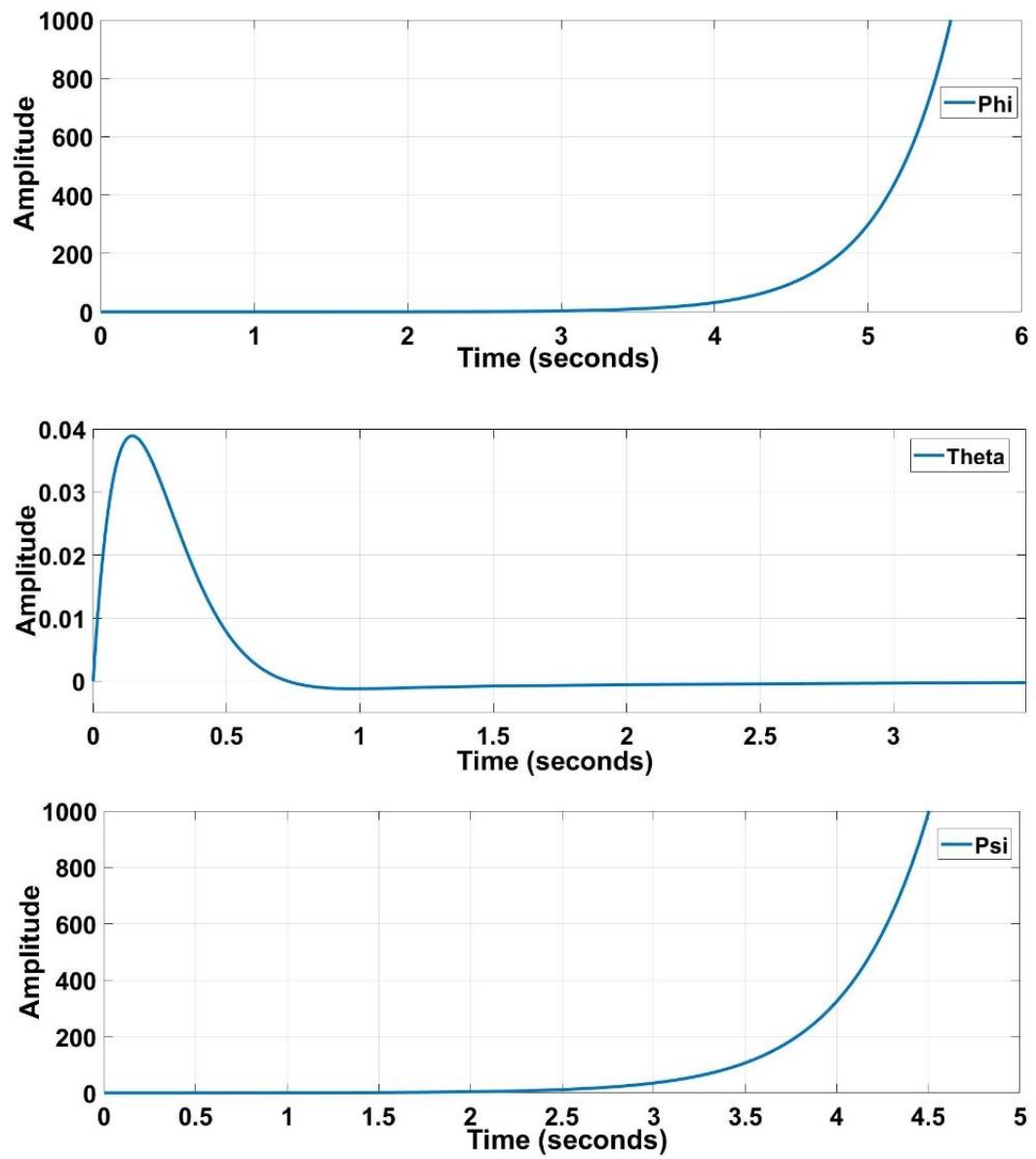


Figure 4.3. Impulse Responses of the Aircraft for Forward Flight

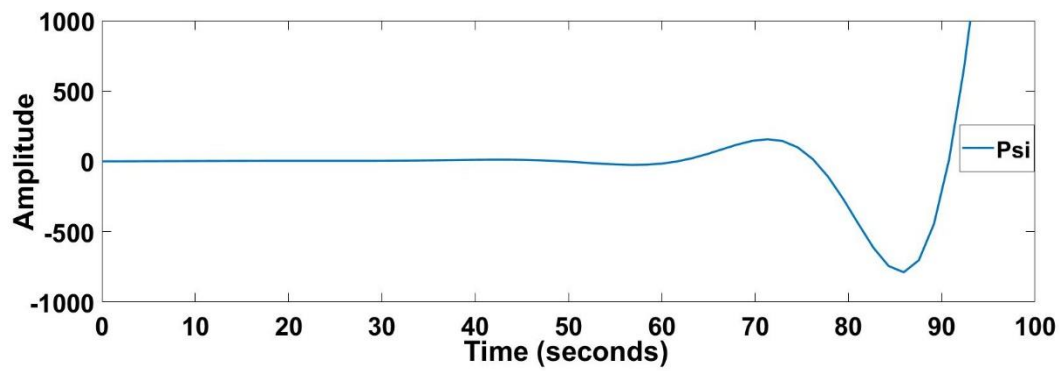
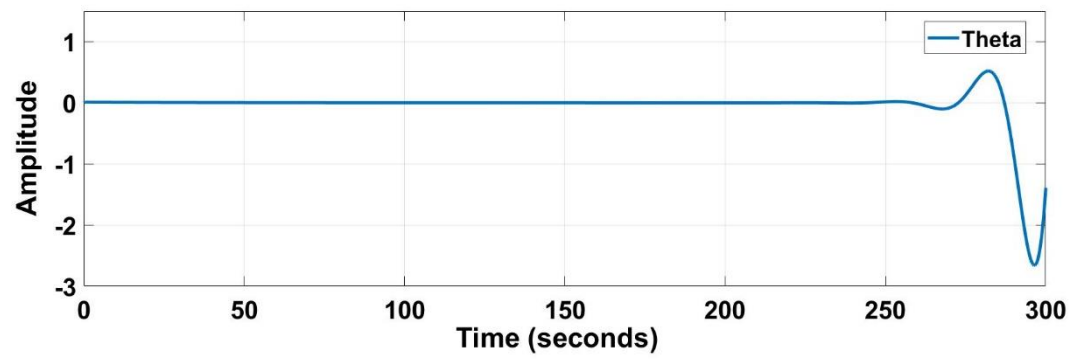
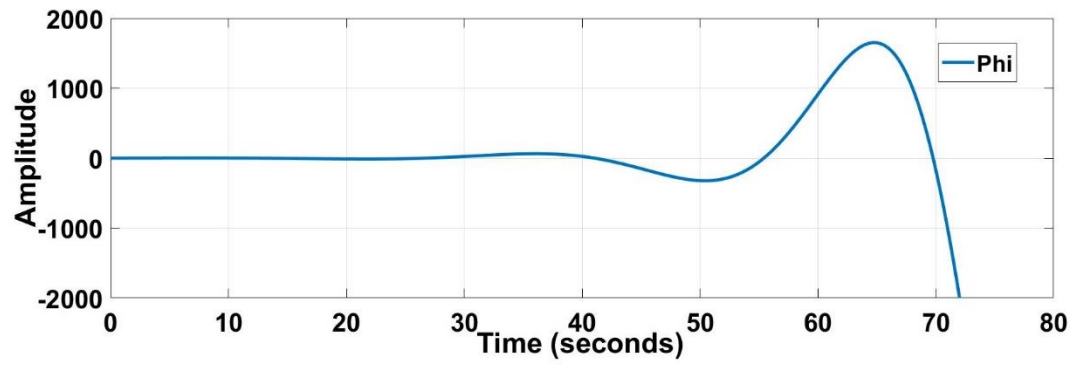


Figure 4.4. Impulse Responses of the Aircraft During Hover

4.4 Controllability

A system is said to be controllable if any initial state $\underline{x}(t_0)$ can be transferred or changed to any final state $\underline{x}(t_f)$, by applying a suitable control $\underline{u}(t)$ over this finite interval of time ($t_0 < t < t_f$). Testing controllability is done by checking if the controllability matrix has full row rank or not. A and B matrices are defined in Eq. 124.

$$\text{rank}([B \ AB \ A^2B \ \dots \ A^{n-1}B]) = n \quad (127)$$

Controllability matrix has been found using the MATLAB function “*ctrb*” which takes the system and input matrices as inputs and gives the controllability matrix as an output. After getting the controllability matrix, the rank of the matrix has been calculated by using the “*rank*” function, which is also a function of MATLAB. Nine linearized points are calculated as fully controllable by using the “*ctrb*” and “*rank*” commands in MATLAB.

CHAPTER 5

CONTROLLER DESIGN

A controller should augment the stability of the system, reject disturbances, reduce the sensitivity to parameter variations, track reference, be robust to uncertainties. A VTOL UAV should be able to fly in different flight modes; therefore, the controller should be designed for different flight modes and the transition between them. The controller should eliminate the transient response of the aircraft, which means that transition between two flight modes should be smooth. Additionally, when the aircraft is commanded to increase the horizontal and vertical velocity at the same time, the controller should decide on how to fulfill that objective. Available control methods are tailored to suit VTOL-UAV's characteristics to obtain non-conflicting results for the same objectives.

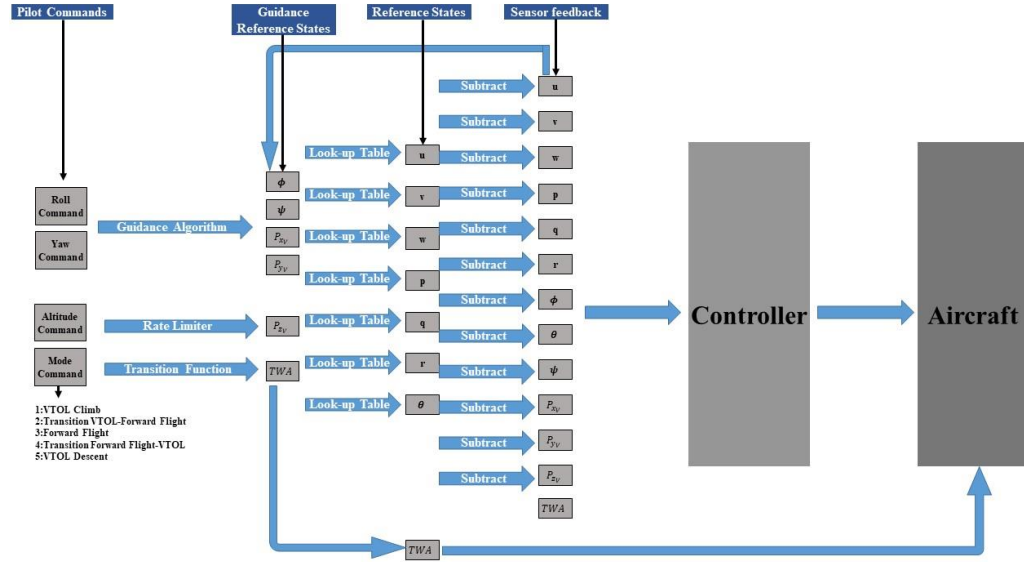


Figure 5.1. Controller Architecture without Mixer

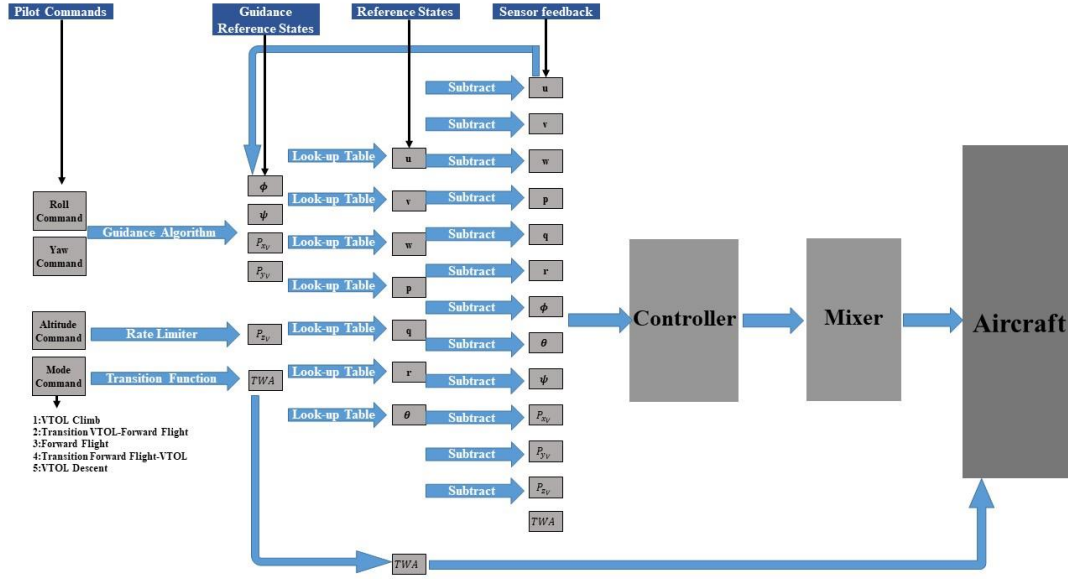


Figure 5.2. Controller Architectures with Mixer

Figure 5.1 and 5.2 illustrate the controller architectures. The only difference between the two architectures is that one has a mixer while the other one has not. In the first method, the input is the state vector, and the output of the controller is the elevator and aileron deflections, and the six motor angular velocities. However, for the second one, control outputs are desired forces in three axes and the desired moments in three axes. The desired forces and moments go directly to the mixer, which determines how much deflection or angular velocity is needed from the actuators.

The pilot has four command buttons in the pilot block. These are mode, roll, yaw, and altitude commands. The mode command determines in which mode aircraft will fly, which can be VTOL, transition, or forward flight. If the pilot gives roll command, aircraft will automatically start a coordinated turn maneuver. Aircraft will track a circle until roll command turns into zero. Before giving zero roll command, the pilot should determine which yaw command should aircraft should track. Otherwise, the aircraft will start turn maneuver opposite direction till the old yaw command is achieved. Small yaw command should be given directly by yaw command, while high yaw commands should be performed by roll command. If there will be any difference between altitude command and the current altitude, the aircraft will start to descent or climb until the desired altitude is achieved. However, the

altitude command will be given with a rate limiter since huge altitude differences will result in an unstable climb or descent. Tilt wing angle command will not go to the controller will directly go to the actuator, since it has a small controller itself. However, the sensor will be fed back with Tilt-Wing angle, since controller gains and reference states will change by Tilt-Angle feedback and roll command feedback.

Mission profile given in Chapter 2 dictates that aircraft should provide performance vertical climb, transition to forward flight, climb, a coordinated turn, a descent, and a vertical descent. Different controllers and schedulers are designed in accordance with the mission profile. Tilt-wing angle changes with a schedule given by guidance commands. Coordinated turn has a unique controller gain set. The transition phase has five gain sets, while each VTOL and forward flight have one gain set. For the first architecture, actuator movements determined by the controller directly, however in the second one controller determines the force and moment needed in each axis, then the mixer decides the actuator movement by using the control allocation strategy.

5.1 Transition Mode Problem Statement

Transition mode is a finite time period, in which system and input matrices are changing as the wing is tilted. We have specified seven trim conditions for transition, which is enough to cover the region where linearized points are valid. However, in transition mode, while the system is being transferred from one state set to another state set, the wing tilt angle and instantaneous state values should be compatible with each other. For instance, if wing tilts very fast from 15° to 0° , x-axis body velocity will not have time to go from 11.6 m/s to 18.6 m/s, since the desired input value for corresponding trim points will increase linearly. This problem may cause the aircraft to become unstable since the aircraft will be far away from the trim point when the wing tilt angle reaches 0° . Therefore, two approaches named minimum time and minimum energy problems are introduced to overcome this problem.

In Minimum Time Problem, the task is to transfer the system from an arbitrary initial state to a specified “target set” in minimum time. The target set can be constant states, a set of relations between final states, or free states.

$$\dot{\underline{x}} = f(\underline{x}, \underline{u}, t) \quad (128)$$

$$P.I = \int_{t_i}^{t_f} dt = t_f - t_i \quad (129)$$

subject to a typical set of control constraints in the form of;

$$|\underline{u}| = \underline{\mathbb{U}} \quad (130)$$

where $t \in [t_i, t_f]$. If the desired input values are calculated with a minimum time algorithm, the controller will try to pass through transition mode as fast as possible. It will not take into account the battery charge level. Nevertheless, there could be an optimization technique that prioritizes energy instead of time. Then we can introduce time minimum energy problem as;

$$P.I = \int_{t_i}^{t_f} [\beta_i u_i^2(t)] dt \quad (131)$$

where β_i represents the weighting factors of each input variable.

For both of the problems, we should determine the prioritized states and input variables. In transition mode, the critical state is the body x-axis velocity, and the critical input variables are front rotor angular velocities. By changing front rotors' desired values in transition, we will try to minimize the performance index. However, as we discussed previous chapters, we have already determined the trim conditions, which include front rotors values as well. We should try to focus on between trim conditions. Since we have two transition types during the flight, we should analyze both transitions from 90° to 0° and 0° to 90°.

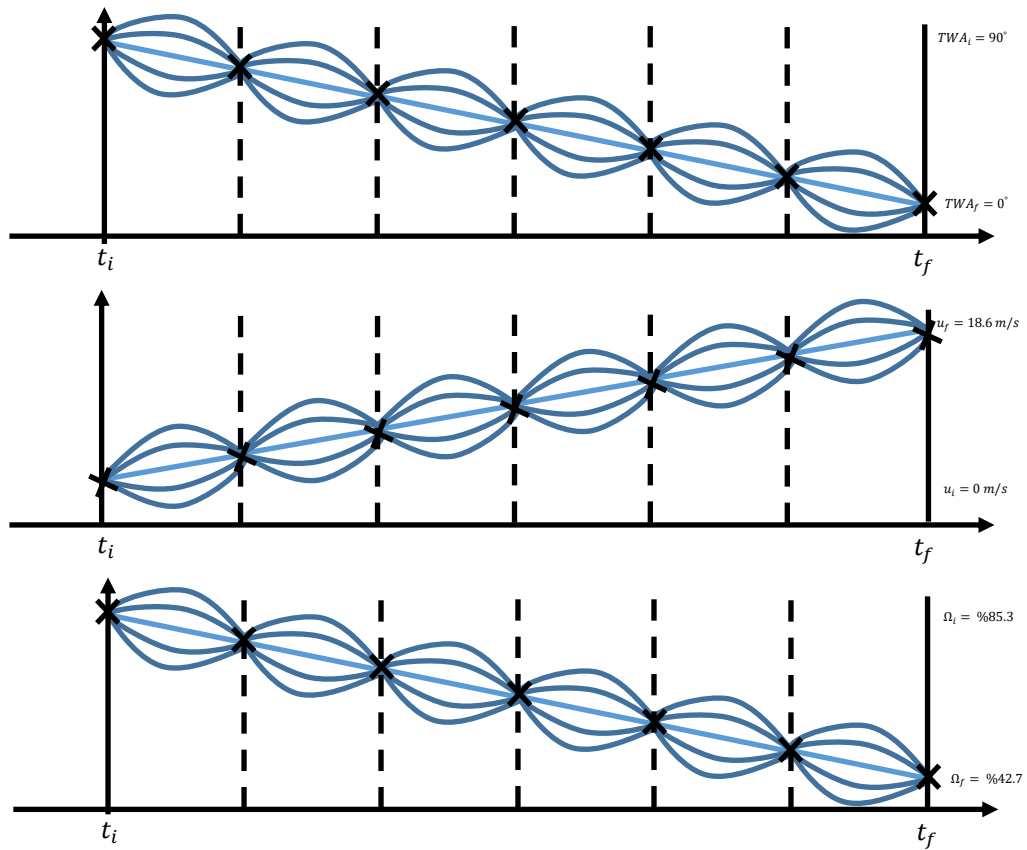


Figure 5.3. Possible Ways of Going from One State to Another

There are infinite ways of going from 90° to 0° as you can see from Figure 5.3. Optimal control input will let us go from one state to another state in minimum time or by using minimum energy without stability loss. Figure 6.120 showed us that energy consumptions during the transition from 0° to 90° or from 90° to 0° are incredibly high since we did not optimize the control strategy. We had to wait until aircraft slows down; however, in VTOL and transition mode, each second has importance due to high energy consumption.

In transition mode, the main target has a stable transition without altitude loss. However, if the throttle level changes linearly, horizontal velocity might not track the target velocity as the wing is tilted. Therefore, a set of equations of motion has been introduced, which sets a schedule for engine throttle level, w , and tilt angle. Equations of motion for altitude and body velocity u can be written in a reduced form as;

$$\begin{aligned}\dot{h} &= -\frac{1}{2}\frac{\rho V^2 S C_L}{m} + 9.81 - \frac{26u_{th} \sin(\delta_{TWA})}{m} \\ \dot{u} &= -\frac{1}{2}\frac{\rho V^2 S C_D}{m} + \frac{26u_{th} \cos(\delta_{TWA})}{m}\end{aligned}\tag{132}$$

We can represent this set of equations in state-space representation;

$$\begin{aligned}\dot{x}_1 &= -0.0372x_2^2(0.76 + 4.97\alpha) + 9.81 - 6.34u_3^2u_2 \\ \dot{x}_2 &= -0.0033x_2^2 + 6.34u_3^2\end{aligned}\tag{133}$$

We can arrange Eq. 133 as;

$$\begin{aligned}\dot{x}_1 &= -0.0282x_2^2 - 0.184x_2u_1 + 9.81 - 6.34u_3^2u_2 \\ \dot{x}_2 &= -0.0033x_2^2 + 6.34u_3^2\end{aligned}\tag{134}$$

Eq. 134 can be linearized around trim conditions;

$$\begin{aligned}\dot{x}_1 &= -1.049x_2 - 3.42u_1 - 1.155u_2 - 0.66u_3 \\ \dot{x}_2 &= -0.122x_2 + 5.41u_3\end{aligned}\tag{135}$$

Linearized system and input matrices are;

$$\begin{aligned}A &= \begin{bmatrix} 0 & -1.049 \\ 0 & -0.122 \end{bmatrix} \\ B &= \begin{bmatrix} -3.42 & -1.155 & -0.66 \\ 0 & 0 & 5.41 \end{bmatrix}\end{aligned}\tag{136}$$

$u_3(t)$ can be assumed as a second-order polynomial and can be represented as;

$$u_3(t) = at^2 + bt + c\tag{137}$$

We know the initial and final values of the throttle levels from the trim conditions,

$$\begin{aligned}u_3(t_i) &= 0.47 \\ u_3(t_f) &= 0.427 \\ u_3(t) &= at^2 + bt + 0.47\end{aligned}\tag{138}$$

We should find a and b constants which minimize total time with constraints

$0 \leq u_3 \leq 1$;

$$T = \frac{-b \mp \sqrt{b^2 - 1.88a}}{2a}\tag{139}$$

MATLAB *fmesh*(*T*) function has been used to see the *a* and *b* constants, which minimizes the total time.

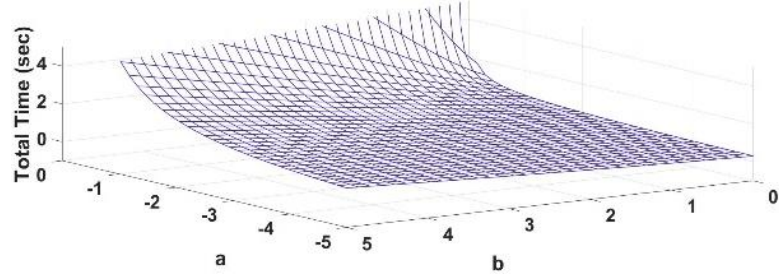


Figure 5.4. Total Time change with respect to *a* and *b* constants

The throttle level schedule is selected from Figure 5.4. Note that this selection directly affects the change of *u* during the transition from 15° to 0°, which is represented in Figure 5.5. Having selected the throttle level schedule, now we can calculate the change of *u*;

$$\begin{aligned}\dot{x}_2 &= -0.122x_2 + 5.41(at^2 + bt + 0.47) \\ x_2 &= 1872.2e^{-0.122t} - 11.97t^2 + 229.53t + -1860.6\end{aligned}\quad (140)$$

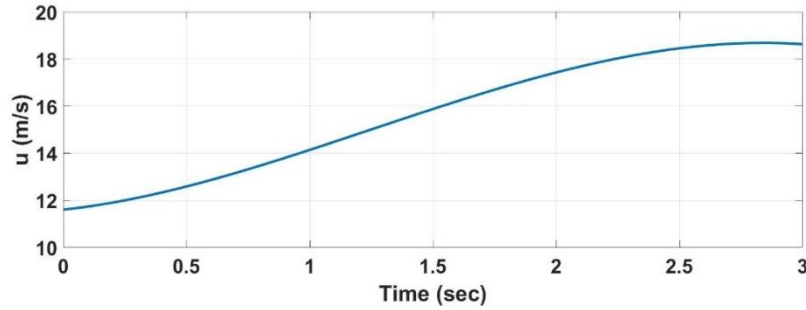


Figure 5.5. Body Velocity *u* change during transition from 15° to 0°

It should be kept in mind that the main target in transition is altitude hold; therefore, we should make sure that altitude is not changing during the transition.

$$\dot{x}_1 = -1.049x_2 - 3.42u_1 - 1.155u_2 - 0.66u_3 = 0 \quad (141)$$

In Equation 141, *x*₂ and *u*₃ are known, and *u*₂, which represents tilt angle changes, is assumed to change linearly. With this assumption *u*₁ which represents *α*, can be calculated. Note that this scheduling is not directly related to the controller. Instead,

it decides the desired states and input values, which will be used by the controller. The desired states and control inputs are calculated using the above flowchart for each transition period.

5.2 Control Allocation

Control Allocation has been done to accomplish a balance between performance and energy consumption. Control allocation logic has been constructed in the light of CFD Analysis and Thrust database interpretation. For each potential trim condition, the effectiveness of each control input has been investigated.

Table 5.1 Control Allocation Chart

$\delta_{TW} = 90^\circ$	Elevator	Flap	First Motor	Second Motor	Third Motor	Fourth Motor
δX	0%	100%	0%	0%	0%	0%
δY	0%	0%	0%	0%	0%	0%
δZ	0%	0%	50%	50%	0%	0%
δL	0%	0%	50%	50%	0%	0%
δM	0%	0%	0%	0%	50%	50%
δN	0%	0%	0%	0%	50%	50%
$\delta_{TW} = 60^\circ$	Elevator	Aileron	First Motor	Second Motor	Third Motor	Fourth Motor
δX	0%	0%	50%	50%	0%	0%
δY	0%	0%	0%	0%	0%	0%
δZ	0%	0%	50%	50%	0%	0%
δL	0%	0%	50%	50%	0%	0%
δM	0%	0%	0%	0%	50%	50%
δN	0%	0%	0%	0%	50%	50%
$\delta_{TW} = 30^\circ$	Elevator	Aileron	First Motor	Second Motor	Third Motor	Fourth Motor
δX	0%	0%	50%	50%	0%	0%
δY	0%	0%	0%	0%	0%	0%
δZ	0%	0%	50%	50%	0%	0%
δL	0%	100%	0%	0%	0%	0%
δM	100%	0%	0%	0%	0%	0%
δN	0%	0%	0%	0%	50%	50%
$\delta_{TW} = 75^\circ$	Elevator	Aileron	First Motor	Second Motor	Third Motor	Fourth Motor
δX	0%	0%	50%	50%	0%	0%
δY	0%	0%	0%	0%	0%	0%
δZ	0%	0%	50%	50%	0%	0%
δL	0%	0%	50%	50%	0%	0%
δM	0%	0%	0%	0%	50%	50%
δN	0%	0%	0%	0%	50%	50%
$\delta_{TW} = 45^\circ$	Elevator	Aileron	First Motor	Second Motor	Third Motor	Fourth Motor
δX	0%	0%	50%	50%	0%	0%
δY	0%	0%	0%	0%	0%	0%
δZ	0%	0%	50%	50%	0%	0%
δL	0%	50%	25%	25%	0%	0%
δM	50%	0%	0%	0%	25%	25%
δN	0%	0%	0%	0%	50%	50%
$\delta_{TW} = 15^\circ$	Elevator	Aileron	First Motor	Second Motor	Third Motor	Fourth Motor
δX	0%	0%	50%	50%	0%	0%
δY	0%	0%	0%	0%	0%	0%
δZ	50%	0%	25%	25%	0%	0%
δL	0%	100%	0%	0%	0%	0%
δM	100%	0%	0%	0%	0%	0%
δN	0%	0%	0%	0%	50%	50%
$\delta_{TW} = 0^\circ$	Elevator	Aileron	First Motor	Second Motor	Third Motor	Fourth Motor
δX	0%	0%	0%	50%	50%	0%
δY	0%	0%	0%	0%	0%	0%
δZ	100%	0%	0%	0%	0%	0%
δL	0%	100%	0%	0%	0%	0%
δM	100%	0%	0%	0%	0%	0%
δN	0%	0%	0%	0%	50%	50%

For the vertical flight, candidate control inputs for X-axis were flaps and elevators. Y-axis is not directly controlled in this study. Furthermore, for the Z-axis, roll, pitch,

and yaw control, we were doomed to use thrust forces. Therefore, only X-axes candidates have been assessed using the CFD analysis for vertical flight. There were three options to be selected. The first one was purely flaps, the second one was purely elevators, and the third one was mixed of them. Using purely one actuator was not possible since 20° deflection of the elevator has compensated 18% percent of available X-force, which is caused by the lift generated on the wing, while 20° deflection of flaps have compensated 65% of it. Therefore, both of the surfaces have been deflected to compensate generated X-force in trim conditions. The elevator has been almost fully deflected, which means there is not adequate power on it to use as a control effector. 50% of the flaps are deflected, and the rest of the flaps are reserved for the control power. In other words, only flaps are used as the X-axis control effector. Since only 50% of the flaps are reserved for control power, asymmetric aileron deflection could not be used for yaw axis control. There is not enough power on ailerons to control the yaw axis. Excessive X-axis force generated by the lift on the wing and horizontal tail forces us to use most of the flaps and elevator power to compensate for the X-axis force.

In VTOL mode, the aircraft will be controlled by thrust forces and moments, while aerodynamic forces will be used with secondary importance. In transition mode, the control allocation will depend mainly on thrust. While we get close to the forward flight, the aerodynamic forces and moments will come forward. Table 5.1 shows the control allocation strategy of the study.

In vertical flight as expected, most of the control power comes from thrust forces and moments. In transition flight, since we are almost in the post-stall conditions, we are using thrust forces and moments as primary control power. However, while we are getting closer to the forward flight, aerodynamic forces usage becomes dominant.

During hover and vertical flight, the wing generates aerodynamic force along with body x-axes, we have employed negative flap deflection to compensate for this force. Y-axes forces have not been directly controlled. Thrust forces and moments are stabilizing the roll, pitch, and yaw axis. The differential thrust of forward and rear

propellers controls the pitch axis, while left and right controls the roll axis. During hover, although we do not have a thrust based moment in the yaw axis, we use the torque generated by angular velocities of the propellers. If throttle levels of the left and right propellers are different from each other, torque is generated on the yaw axes. So we change the angular velocities of left and right propellers to control the yaw axis during hover. Cross-coupling of the roll and yaw axes shall be considered in this case, since as we change the angular velocity of the propellers, moment in roll axes will be inevitable.

In the first phase of transition mode, mostly the thrust forces and moments will be in charge. Control allocation logic will be like the one in vertical flight with some small differences, by the way. Between $\delta_{TW} = 90^\circ$ and $\delta_{TW} = 45^\circ$, none of the aerodynamic inputs were used since there was enough power on motors to control the aircraft in 6 DoF. Additionally, since the α is estimated at about 20° , which means that the aircraft is about the stall region, using aerodynamic surfaces to control the aircraft may result in catastrophic conditions. On the other hand, the wing has been chosen due to its high lift characteristics. If additional flaps are used, the wing might enter the stall region. Note that this does not mean that we do not exploit aerodynamic forces. We use aerodynamic forces to trim the aircraft. However, after having trimmed the aircraft, aerodynamic control surfaces like ailerons and elevators are not being used to control it. For roll control, tip rotors are used only to exploit from the long moment arm advantages.

After getting the 30° tilt-angle, α decreases dramatically, which means that aerodynamic surfaces may be used to control the aircraft. 50% of pitch moment can be eliminated by 20° elevator deflection, which gives us enough power to control the pitch axis. Nevertheless, the aircraft should be trimmed by thrust forces in the pitch axis to have excess power in elevators to control the pitch axis. Ailerons give sufficient roll moment to control roll-axes at 30° tilt-angle. Besides the roll and pitch axis, thrust forces and moments should be used.

15° and 0° tilt angle conditions are very similar to each other, except that to trim the aircraft in pitch axis in forward flight, we are deflecting the horizontal stabilizer by -3°, which gives us sufficient excess power to control pitch axis by elevators. At 15° tilt-angle, elevators are compensating 90% of pitch moment, so there is enough power on elevators to purely control the pitch axis. Based on the CFD results and interpretations of the aerodynamic surface control power, the following control allocation logic has been adopted.

Between $\delta_{TW} = 30^\circ$ and $\delta_{TW} = 0^\circ$, rear motors will be shut down since we get enough aerodynamic pitch control power after that point. The yaw axis is controlled by the differential thrust of the rear propellers. Pitch axis is purely controlled by elevators, and roll is purely controlled by ailerons. The velocity of the aircraft is controlled by throttle and altitude is controlled by elevators. Almost the same logic will be employed during forward flight.

A high-level controller determines the force and moment effectors, and a low-level mixer allocates the needs to related actuators by using the operation logic given in Table 5.1. The control allocation logic given in Table 5.1 has been decided by interpreting CFD results and thrust database.

Control allocation logic has been implemented into the non-linear model via using a mixer, which is a MATLAB function embedded into the Simulink model. This MATLAB function accepts the tilt-wing angle, dynamic pressure, and the desired forces and moments in the body axis as inputs. The output of the mixer is a vector that contains an elevator and aileron deflections, and six propeller angular velocities. This function, which has a flowchart given in Figure 5.6, calculates the related actuator deflections using the linearized relation between forces, moments, actuator positions, and propeller angular velocities by using the engine and aerodynamic database that are embedded into the nonlinear model. The relation between desired forces and moments and the control inputs are generally nonlinear. However, for each trim condition, this relation has been linearized. The linearized relation between forces, moments, actuator positions, and propeller velocities are embedded into the

MATLAB function. For instance, the thrust generated by each rotor is directly proportional to the square of the propeller angular velocity. However, during hover, we can linearize it around trim conditions and assume that it is changing linearly. Note that embedded functions in the mixer are linearized versions of each trim condition. For the no mixer method, the linearized input matrices are created, considering that there is no mixer, and the controller gain matrix is obtained accordingly. Therefore when the state error vector is multiplied by gain matrix, we obtain the desired actuator positions and propeller angular velocities directly.

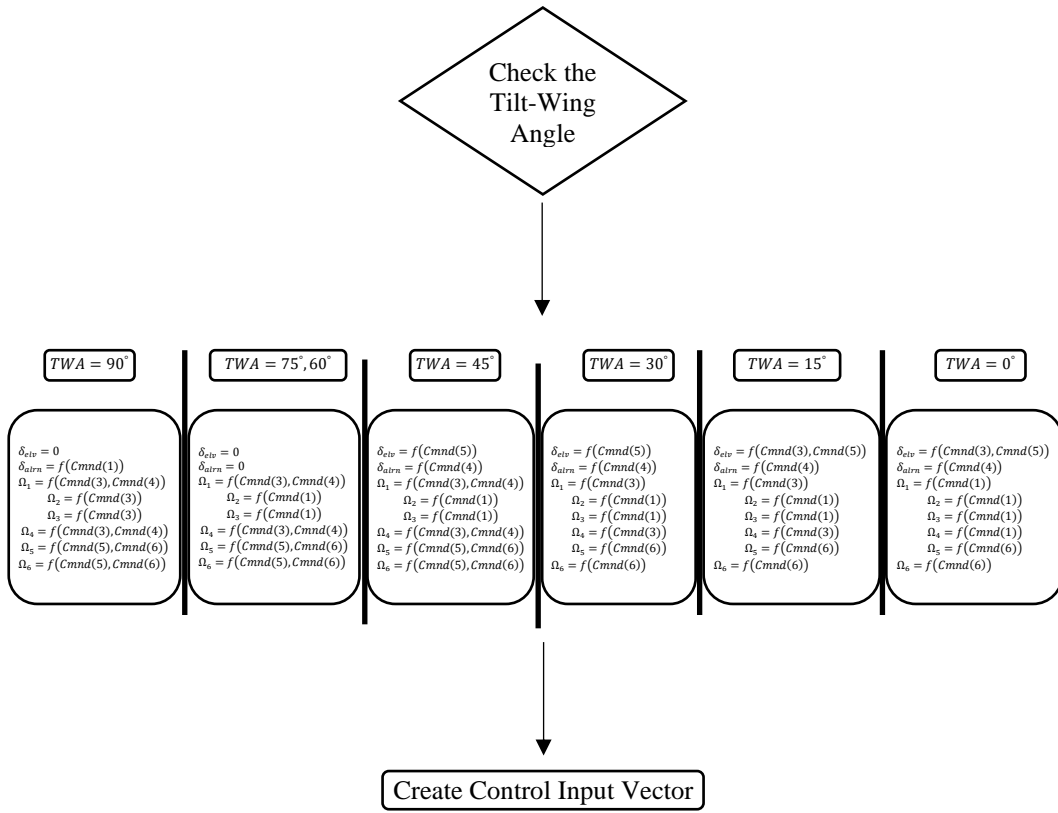


Figure 5.6. The Flowchart of the Mixer

5.3 Linear Quadratic Problem

In control theory, the Linear Quadratic Problem is one of the most fundamental optimal control problems. Optimal control concerns with operating a dynamic system at minimum cost. The case where the system dynamics are described by a set

of linear differential equations, and the cost is described by a quadratic function is called the “LQ problem” [37]. The solution to this problem can be the state feedback controller or output feedback controller with a state observer. One of the main results, in theory, is that the solution is provided by the linear-quadratic regulator (LQR), a feedback controller, which is an essential part of the solution to the LQG (Linear-Quadratic-Gaussian) problem.

For a dynamic system represented in state-space with or without constraints, let the best control strategy be;

$$\underline{u}^0 = -K^0 \underline{x} \quad (142)$$

such that the performance index (cost function);

$$J = \int_0^\infty (\underline{x}^T Q \underline{x} + \underline{u}^T R \underline{u}) dt \quad (143)$$

is minimized, where Q is at least a positive semi-definite state, and R is a positive definite control weighting matrix. By using the solution, Algebraic Riccati equation (Eq. 144) optimal state feedback gain matrix can be calculated as given in Eq. 145.

$$-Q = A^T P + P A - P B R^{-1} B^T P \quad (144)$$

$$K^0 = R^{-1} B^T P \quad (145)$$

Weighting matrices Q and R should be determined according to acceptable error levels of the states and inputs, respectively. Bryson’s approach is used to select the weighting matrices.

$$Q_{ii} = \frac{1}{\text{maximum acceptable value of } x_i^2} \quad (146)$$

$$R_{ii} = \frac{1}{\text{maximum acceptable value of } u_i^2} \quad (147)$$

For LTI systems, it should be kept in mind that states refer to the error between reference states and real states. Therefore, while determining the weighting, matrices error levels should be considered. Selected weighting matrices can be found in Appendix B. With the gain matrices given in Appendix B, the system has closed-loop eigenvalues as;

$$\begin{aligned}
eig(A_{TWA=0^\circ}) &= \begin{bmatrix} -418.15 \\ -33.47 \\ -7.28 \\ -4.72 \\ -2.70 \\ -1.82 \\ -0.83 + 0.88i \\ -0.83 - 0.88i \\ -1.00 \\ -0.44 \\ -0.03 \\ -0.03 \end{bmatrix} & eig(A_{Turn}) &= \begin{bmatrix} -380.27 \\ -33.41 \\ -17.71 \\ -4.25 + 2.68i \\ -4.25 - 2.68i \\ -2.98 \\ -1.2 \\ -0.56 + 0.04i \\ -0.56 - 0.04i \\ -0.23 \\ -0.03 \\ -0.03 \end{bmatrix} \\
eig(A_{TWA=15^\circ}) &= \begin{bmatrix} -220.04 \\ -15.95 \\ -5.57 \\ -2.58 + 2.14i \\ -2.58 - 2.14i \\ -1.09 + 0.97i \\ -1.09 - 0.97i \\ -1.22 \\ -0.68 \\ -0.24 \\ -0.03 \\ -0.03 \end{bmatrix} & eig(A_{TWA=30^\circ}) &= \begin{bmatrix} -176.14 \\ -89 + 3.14i \\ -89 - 3.14i \\ -2.13 + 2.26i \\ -2.13 - 2.26i \\ -1.67 \\ -1.29 + 0.79i \\ -1.29 - 0.79i \\ -0.57 \\ -0.17 \\ -0.02 \\ -0.03 \end{bmatrix} \\
eig(A_{TWA=45^\circ}) &= \begin{bmatrix} -133.67 \\ -8.36 + 1.62i \\ -8.36 - 1.62i \\ -2.32 + 2.31i \\ -2.32 - 2.31i \\ -1.3 + 1.23i \\ -1.3 - 1.23i \\ -0.38 \\ -0.46 \\ -0.13 \\ -0.02 \\ -0.03 \end{bmatrix} & eig(A_{TWA=60^\circ}) &= \begin{bmatrix} -93.7789 \\ -6.3403 + 0.6365i \\ -6.3403 - 0.6365i \\ -2.5962 + 2.5146i \\ -2.5962 - 2.5146i \\ -1.2654 + 1.2703i \\ -1.2654 - 1.2703i \\ -1.2479 \\ -0.6431 \\ -0.1161 \\ -0.022 \\ -0.031 \end{bmatrix} \\
eig(A_{TWA=75^\circ}) &= \begin{bmatrix} -79.6928 \\ -6.8532 \\ -4.7 \\ -2.56 + 2.5i \\ -2.56 - 2.5i \\ -1.26 + 1.33i \\ -1.26 - 1.33i \\ -1.167 \\ -0.8856 \\ -0.0759 \\ -0.0214 \\ -0.0306 \end{bmatrix} & eig(A_{TWA=90^\circ}) &= \begin{bmatrix} -67.9153 \\ -4.2693 \\ -2.4209 + 2.3456i \\ -2.4209 - 2.3456i \\ -1.819 \\ -1.5805 + 1.6782i \\ -1.5805 - 1.6782i \\ -0.0606 + 0.0597i \\ -0.0606 - 0.0597i \\ -0.0263 \\ -0.0331 \\ -0.0311 \end{bmatrix}
\end{aligned} \tag{148}$$

5.4 PID Controller Design

The second controller type is the PID method, which calculates an error value as the difference between the desired setpoint and a variable. The controller adjusts the control variables and tries to minimize the error over time.

$$u(t) = k_p e(t) + k_i \int_0^t e(\tau) d\tau + k_d \frac{de(t)}{dt} \quad (149)$$

where $e(t) = x_d(t) - x(t)$, x_d is desired state variable value and k_p, k_i, k_d are non-negative coefficients.

k_p produces an output that is proportional to the instantaneous error value. A high gain may result in the system becoming unstable. If the gain is too small, then the response will be sluggish.

k_i produces an output that depends on accumulated error for a time interval, which means that the output will be affected by both previous and present errors. This term can be used to eliminate steady-state error since it accelerates the movement towards the desired value. However, as time goes to infinity, there can be an integral windup issue due to error accumulation. Therefore, there should be an integral limit to prevent windup.

k_d produces an output proportional to the derivative of the error over time. This term improves the settling time and stability of the system. Nevertheless, high-frequency noise's adverse effects should be considered when this term is used. There will be a low pass filter in derivative terms to prevent high-frequency noise.

PID Controllers are generally used for SISO Systems. As Tilt-Wing UAV is a non-linear MIMO system, a sequential loop closure technique should be used for PID implementation. Two sequential loops are used for loop closure. The inner loop is responsible for angular rates and axial accelerations (u, w, p, q, r) , while the outer loop is tracking $(v, \phi, \theta, \psi, h)$. There is a separate block that decides the desired states' values and sends them to the controller.

PID Tuning should be done to have a good response to the system. Controller gains are adjusted in this method to have an optimum response of the system. Having a stable system is the first essential requirement. The performance specification of the system can be defined in the frequency domain or time domain. In the frequency domain, typical specifications are damping ratio, natural frequency, damping factor, damped frequency, resonant peak, resonant frequency, bandwidth, phase margin, and gain margin. In the time domain, delay time, rise time, settling time, peak overshoot, percent overshoot, and steady-state error could be used as a performance specification.

Table 5.2 Controller Gains Determination

Controller Type	K_p	K_i	K_d
<i>P</i>	$0.50K_u$		
<i>PI</i>	$0.45K_u$	$0.54K_u/T_u$	
<i>PID</i>	$0.60K_u$	$1.2K_u/T_u$	$3K_uT_u/40$

Ziegler-Nichols Method is employed for PID Tuning. In this method, integral and derivative terms of the gains are set to zero. After that, the proportional term is increased until the system oscillates continuously. The gain at which system oscillates called as ultimate gain (K_u) and the oscillation period is called as T_u . Having determined the ultimate gain and oscillation period, controller gains can be set using the algorithm given in Table 5.2.

CHAPTER 6

SIMULATION RESULTS

Non-linear Simscape model of the aircraft is used to assess the designed LQR and PID controller. This section describes the response of the system to given commands by pilot and response of the system to the external force conditions.

6.1 Mission Definition

The simulation starts on the ground. The aircraft is on VTOL mode when the simulation is started. Under pilot commands, the controller tries to keep the trim conditions. After a while, vertical climb command is given. When the aircraft climbed at the desired altitude, the transition command is given. The pilot can monitor all the critical indicators in the pilot cockpit, instantaneously. The transition takes about 28 seconds. After the transition, the aircraft is automatically beginning to level flight. When the pilot gives the roll command, the aircraft will start a coordinated turn. The command will be given with a rate limiter in order to prevent high overshoots.

Variable step size is chosen as the simulation step size. The ODEs are solved using the 4th order Runge Kutta Method. Simulation results are presented in two parts; with disturbances, effects are included and without any disturbances effect.

6.2 Linear and Non-Linear Closed-Loop Response

6.2.1 VTOL Simulation Results

VTOL simulation results have shown that Linear and Non-Linear Models have complied with each other. Roll stability has sufficient dynamic response, while the

pitch angle settles down too late. Pitch angle and altitude are crossed coupled. Altitude weight was chosen as the most important one while determining the weighting matrix in LQR design. So, the controller is always giving priority to altitude. Therefore, the pitch angle settling takes too much time. This condition does not affect the success of the mission. So it is assumed that the roll and pitch angle response of the aircraft is acceptable.

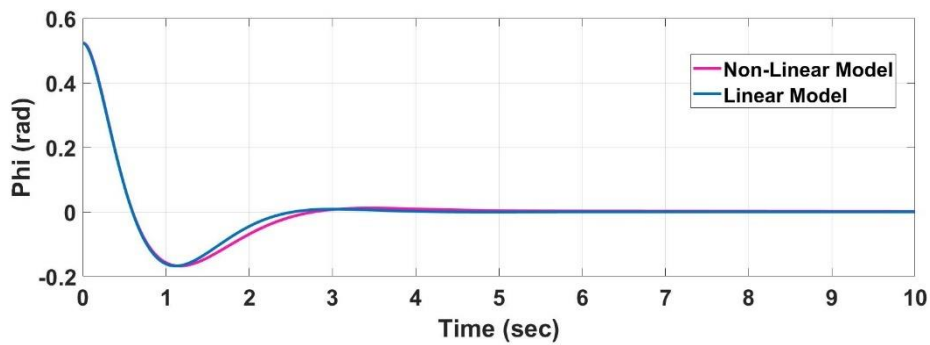


Figure 6.1. Roll Angle Response of the Aircraft in VTOL mode

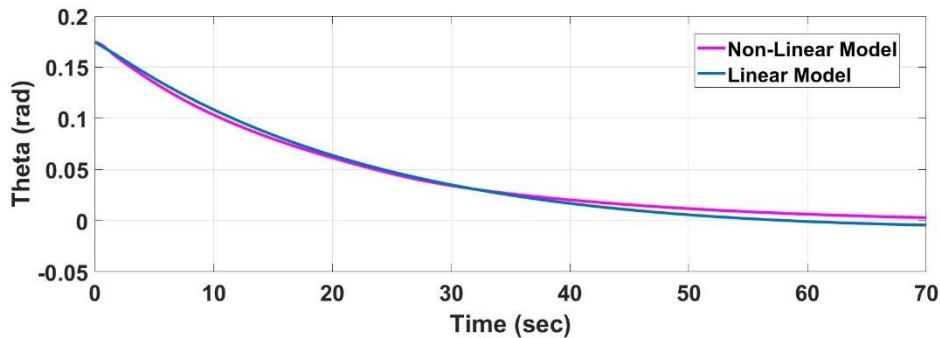


Figure 6.2. Pitch Angle Response of the Aircraft in VTOL mode

Altitude error is quickly compensated by the aircraft in both linear and non-linear models. As aircraft have diverged from the trim point, aircraft dynamics are changing. The difference between linear and non-linear models stem from the aircraft dynamics change. While the linear model assumes that aircraft dynamics are not changing during compensation, the non-linear model takes into consideration the aircraft dynamics change. The altitude error penalty creates a small difference between linear and non-linear responses. Since the penalty given to altitude error is a very high, non-linear model diverges from the trim point to compensate for the error quickly. However, a rate limiter has been used to prevent possible unstable

behavior. This condition creates a difference between linear and non-linear responses.

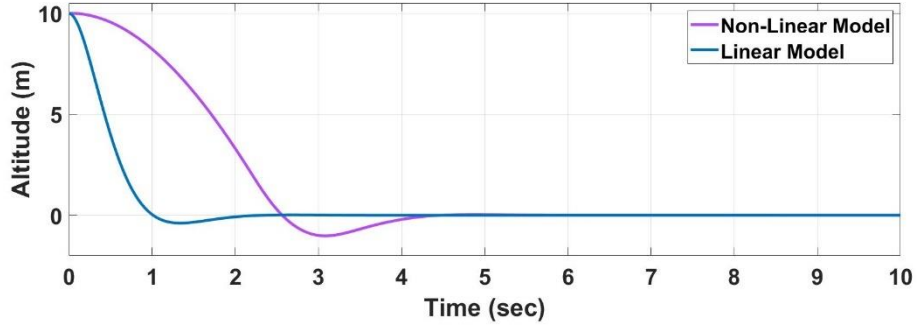


Figure 6.3. Altitude Response of the Aircraft in VTOL mode

Altitude change command is given in third seconds, and the aircraft is climbed at 10 m altitude within four seconds. It can be inferred from Figure 6.4 that the aircraft is able to reject the disturbances.

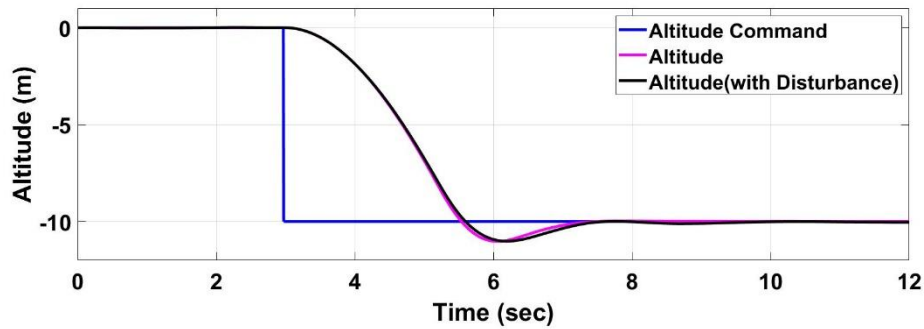


Figure 6.4. Altitude Command and Altitude Response of the Aircraft in VTOL Mode

6.2.2 Level Flight Simulation Results

Level Flight Simulation has shown that aircraft have reasonable dynamics in forward flight. The roll angle command is given with a rate limiter to decrease the risk of roll-yaw coupling. The system has overshoot at a reasonable level. Even if there is strong gust during the roll change, the aircraft is able to obey the given commands within acceptable levels.

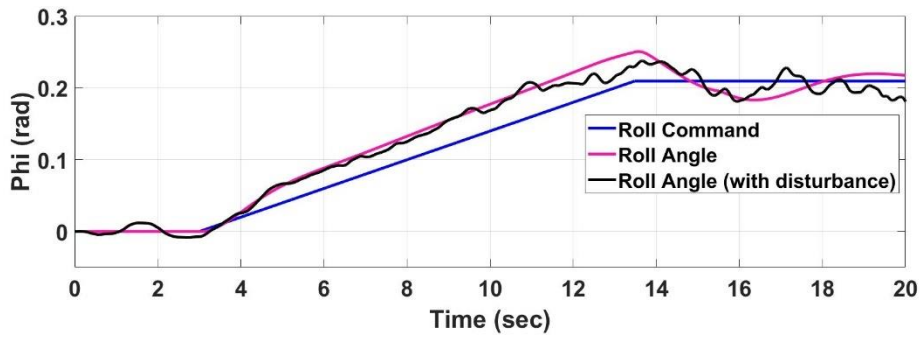


Figure 6.5. Roll Command and Roll Angle Response of the Aircraft in Forward Flight Mode

When there is no external force applied, the system is having a good correlation with the linear model response. Even if strong gust is applied, there are small deviations while converging to the trim conditions.

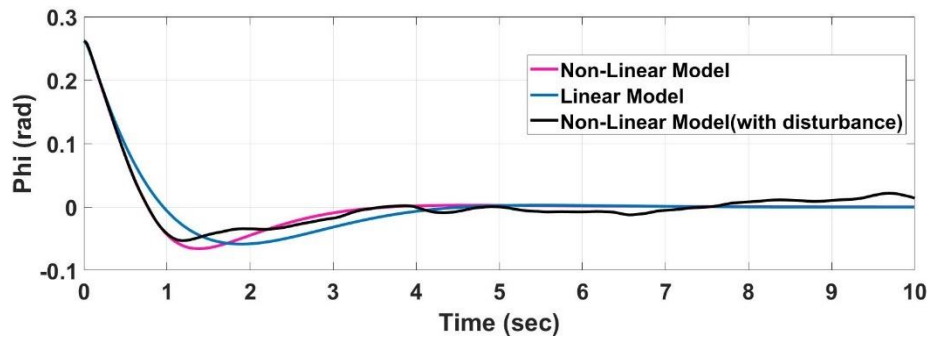


Figure 6.6. Roll Angle Response of the Aircraft in Forward Flight Mode

Although the linear model has a high time constant, the non-linear model shows a sluggish response since the weighting matrix used in LQR design is giving less importance to the theta while increasing the importance of the altitude.

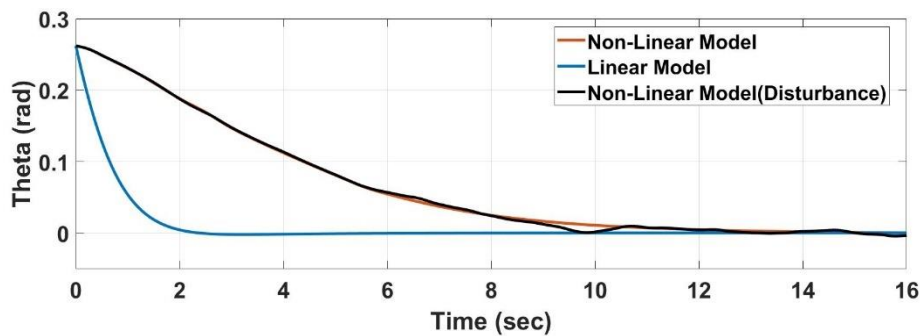


Figure 6.7. Pitch Angle Response of the Aircraft in Forward Flight Mode

The yaw response of the aircraft to the given yaw command seems to be acceptable. When the gust is applied, there is a small deviation from the desired angles. However, after a while, the aircraft is stabilized. Since yaw command is given as a step command, the pilot should give small commands when the yaw command is used. If there is a need for high yaw angle changes, roll command should be used to turn into the desired yaw angle.

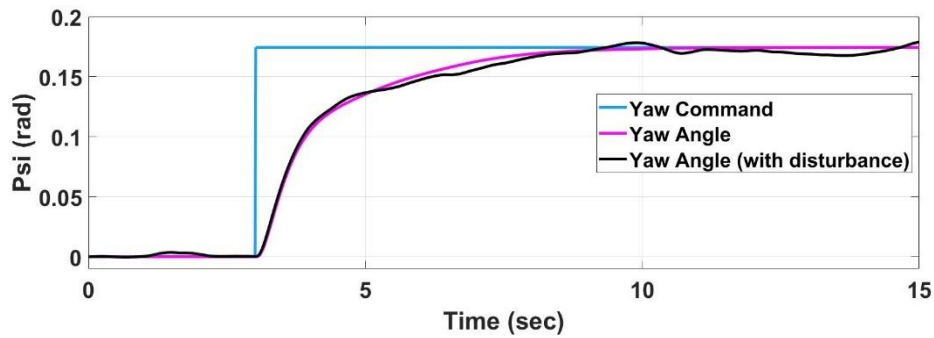


Figure 6.8. Yaw Command and Yaw Angle Response of the Aircraft in Forward Flight Mode

Non-linear and linear models have almost the same dynamics while converging to the trim condition. The disturbance rejection level of the aircraft is acceptable. Yaw angle is settling down in about 5 seconds, which shows the system has good directional stability.

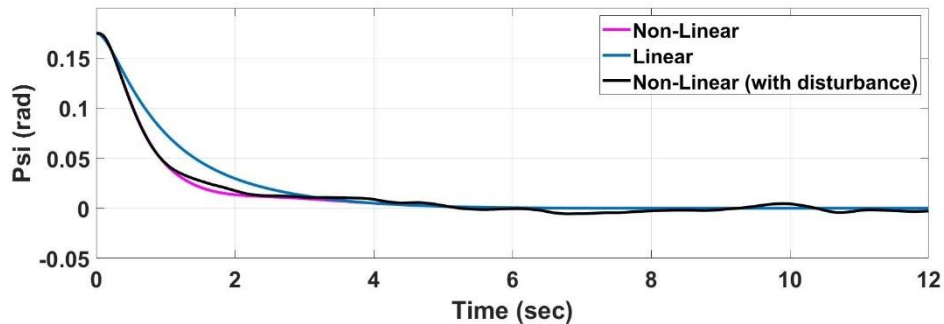


Figure 6.9. Yaw Angle Response of the Aircraft in Forward Flight Mode

Altitude command is given with a rate limiter. The altitude weight is very high, which means that LQR is giving a high penalty to the altitude error. This condition results in a rapid response in altitude dynamics. However, when the difference between desired altitude and current altitude is high, the controller gives a very high

altitude change command, which can cause an unstable movement. When the rate limiter is used in altitude command, the aircraft shows a good response to the altitude command.

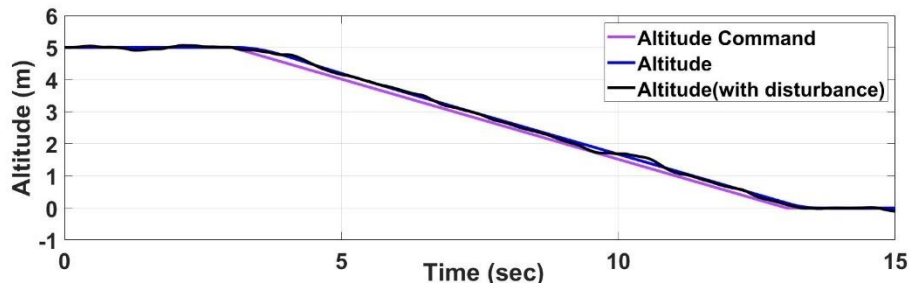


Figure 6.10. Altitude Command and Altitude Response of the Aircraft in Forward Flight Mode

The non-linear and linear model shows a good correlation for no external force case of the altitude response. Aircraft is settled down in six seconds. Although there is a strong gust, altitude dynamics did not change so much from the no disturbance case. The altitude error penalty creates a small difference between linear and non-linear responses. Since the penalty given to altitude error is a very high, non-linear model diverges from the trim point to compensate for the error quickly. However, a rate limiter has been used to prevent possible unstable behavior. This condition creates a difference between linear and non-linear responses.

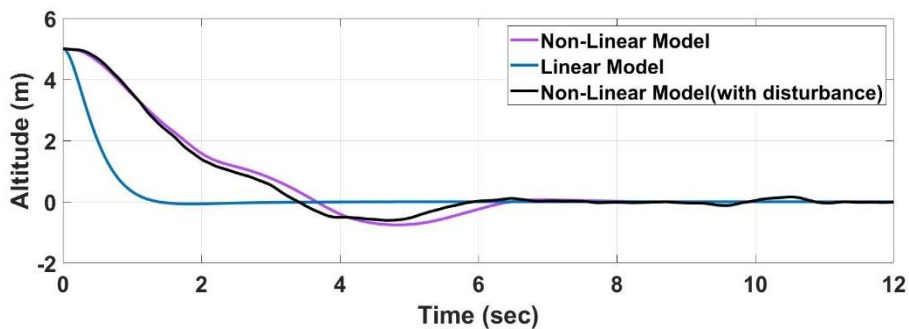


Figure 6.11. Altitude Response of the Aircraft in Forward Flight Mode

6.3 Controller Methods' Comparison Results

Three methods have been compared by looking at energy consumption and tracking errors. The first method is PID with a mixer, the second method is LQR with a mixer, and the last one is the LQR without the mixer. Figure 6.12 shows the time history of the tilt-wing angle during the transition.

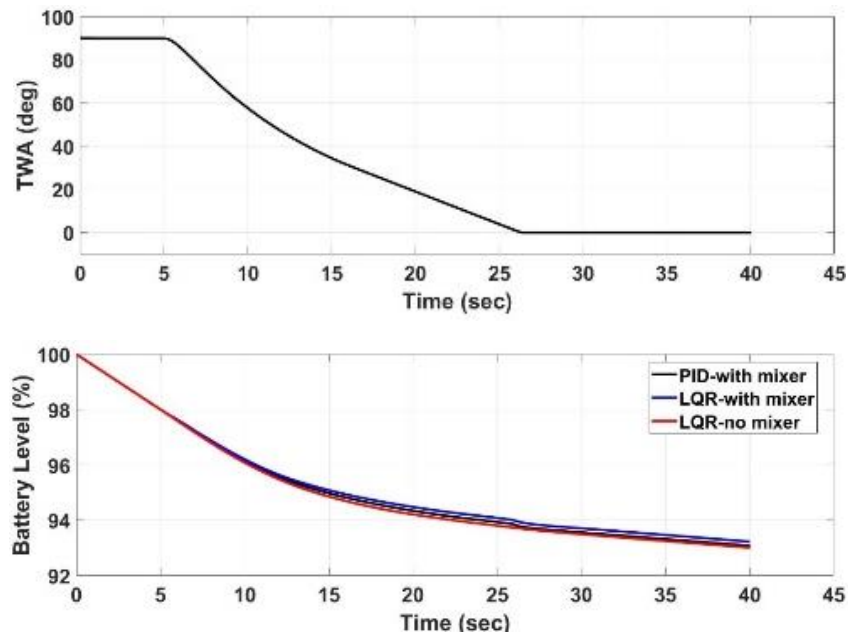


Figure 6.12. Tilt-Wing Angle and Battery Consumption Time History during Transition

Figure 6.12 shows that LQR with a mixer consumes the least battery, while LQR without mixer consumes the most. Two controller shows adequate performance in altitude and axial velocity while there is a 15 cm deviation in LQR without mixer method.

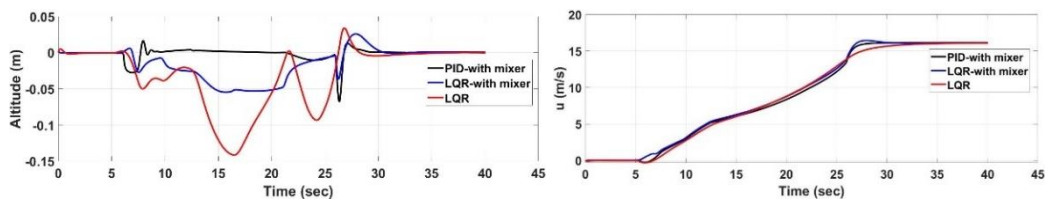


Figure 6.13. Altitude and Axial Velocity Change during Transition

All of the methods show excellent performance while tracking the desired states. However, fluctuations should be in minimum during the transition, since aircraft dynamics are changing very much during the transition.

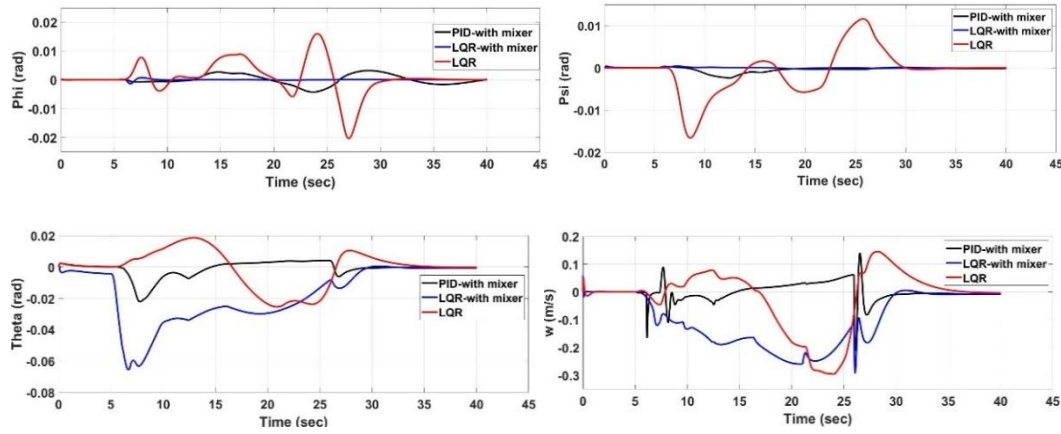


Figure 6.14. Euler Angles and Vertical Body Velocity Time History during Transition

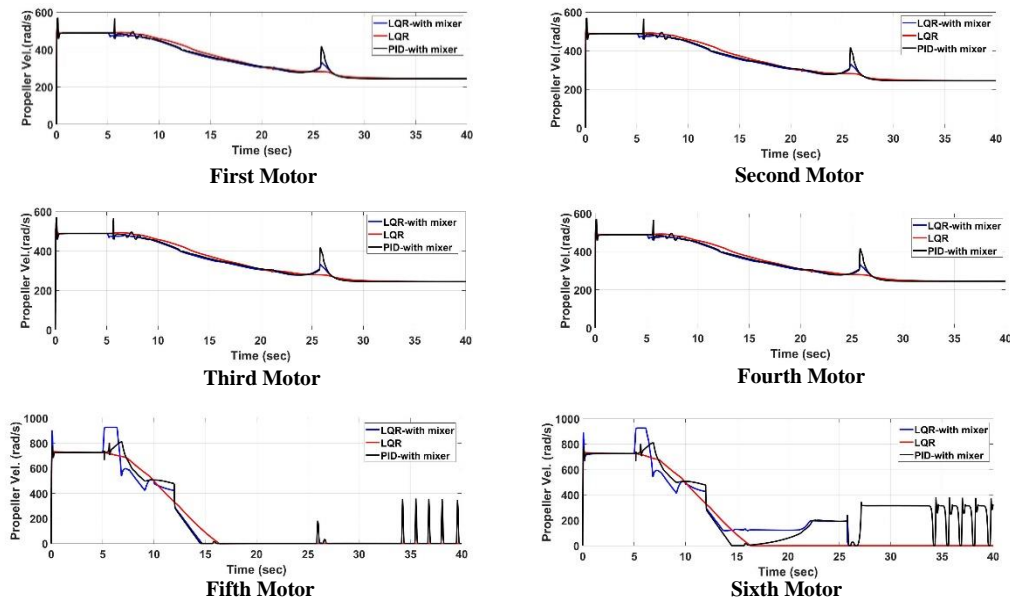


Figure 6.15. Propeller Angular Velocity Changes during Transition

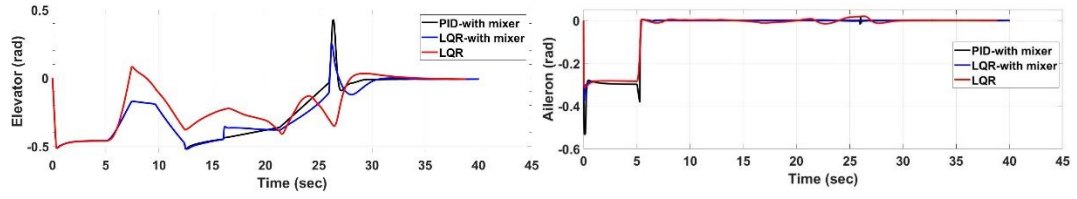


Figure 6.16. Elevator and Aileron Deflection during Transition

Control input changes should track the target input values, and there should not be a transient response of these control values. LQR without mixer shows good behavior while tracking the input values. Considering the three method comparison, LQR with a mixer is chosen as the base method for this study.

6.4 The Effect of Using Separate Signals for Each Motor

After choosing the control method, the effect of using separate signals for outer and inner motors for roll control has been investigated. Three nonlinear models have been compared using performance indexes. In the first model, ailerons have been used for roll control. The second model assumes that front motors have been used for roll control during the transition with the same weight of inner and outer motors. The third model is also using front motors for roll control; however, it assumes that front inner motors are not being used for roll control. The performance index to compare each method can be seen in Eq. 150.

$$J = \int_0^{\infty} |x| dt \quad (150)$$

The performance index calculates the error level of each method in every step and sums up the absolute value of them, cumulatively. The performance of altitude and roll control has been assessed in Table 6.1 for both under disturbance and no disturbance condition. In accordance with these results, the 3rd method has been implemented in the non-linear model. Separate signals will be sent for outer and inner motors during the transition.

Table 6.1 Performance Results of Each Method

	1 st Method (no dist.)	1 st Method (with dist.)	2 nd Method (no dist.)	2 nd Method (with dist.)	3 rd Method (no dist.)	3 rd Method (with dist.)
Altitude	0.6542	0.8785	0.595	0.697	0.5939	0.6958
Roll	0.3298	3.985	0.22	4.232	0.1957	4.113

6.5 CFD Resolution Effect on Model Accuracy

As discussed in Chapter 2, 5670 CFD runs have been performed during the CFD analysis. CFD resolution effect on the non-linear model has been investigated to contribute further studies about transition flight. We have decreased the number of CFD runs by employing five tilt angles (0° , 30° , 45° , 60° , 90°) instead of seven. A new lookup table that has five tilt angle positions have been used for the new simulation. Performance indexes for roll and yaw angles have been defined as given in Eq. 150 and altitude errors have been plotted to see the effect of decreasing the resolution of the CFD analysis. Roll and Yaw performances of the original and the low-resolution models can be seen in Table 6.2.

Table 6.2 Performance Results of Each Method

	5670 CFD Runs	4050 CFD Runs
Roll	0.1957	0.3505
Yaw	0.9621	1.187

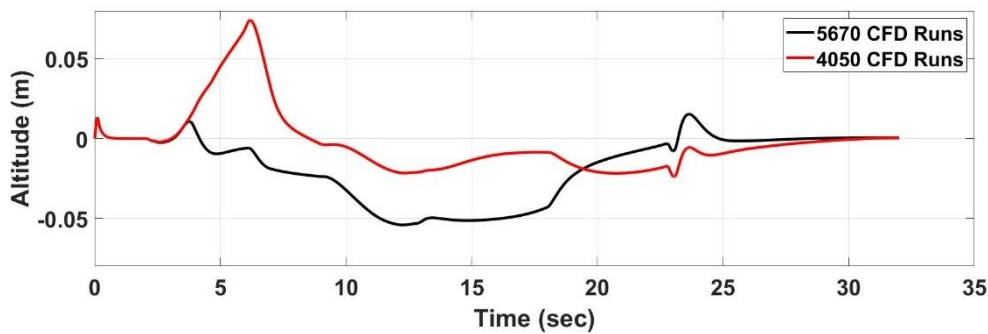


Figure 6.17. Altitude Change during Transition

Figure 6.17 shows the altitude hold performance of the two models. The analysis shows that decreasing 5670 runs to 4050 runs slightly effected the simulation results. Therefore, it is concluded that instead of performing 5670 runs, 4050 runs could be performed.

6.6 Full Mission Simulation Results

The simulation results cover the whole flight envelope of the aircraft for a given trajectory by the pilot. Aircraft will start from the hover position on the ground and will complete the mission when it is come back and starts to hover on the ground. Figure 6.18 shows the trajectory of the aircraft during the simulation. It can be clearly seen that aircraft are capable of doing the mission, which is proposed in Chapter 2.

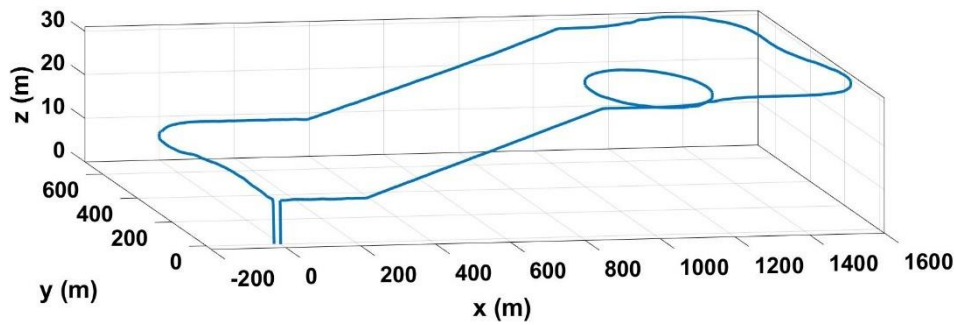


Figure 6.18. The trajectory of the Aircraft during the Mission

Figure 6.19 shows the wind gusts in 3-axis, which are given in the body-fixed coordinates. The prevailing wind is selected as coming from 0° head angle. Therefore, as aircraft change the head angle, the wind effect on aircraft is also changing. However, the disturbance block accepts the Direction Cosine Matrix as an input and converts the wind airspeeds into the body coordinates.

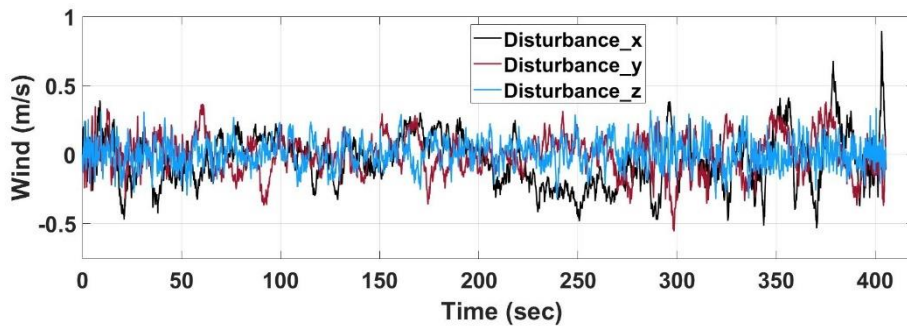


Figure 6.19. Random Gust Generated by the Disturbance Block

It can be clearly seen from Figure 6.20 that VTOL mode energy consumption is very high. Therefore, in mission planning, spent time in VTOL mode should be decreased as much as possible. The desired altitude should be achieved in Forward Flight mode. Energy consumption in Forward Flight is acceptable. Aircraft is capable of flying at forward flight for more than one hour.

Since there are two transition periods during the mission, the TWA angle is changing two times, from 90° to 0° and vice versa, during that period. There is a separate controller to hold the wing at the desired angle. The transition takes 28 seconds. In the transition mode, the main aim is to hold the desired altitude.

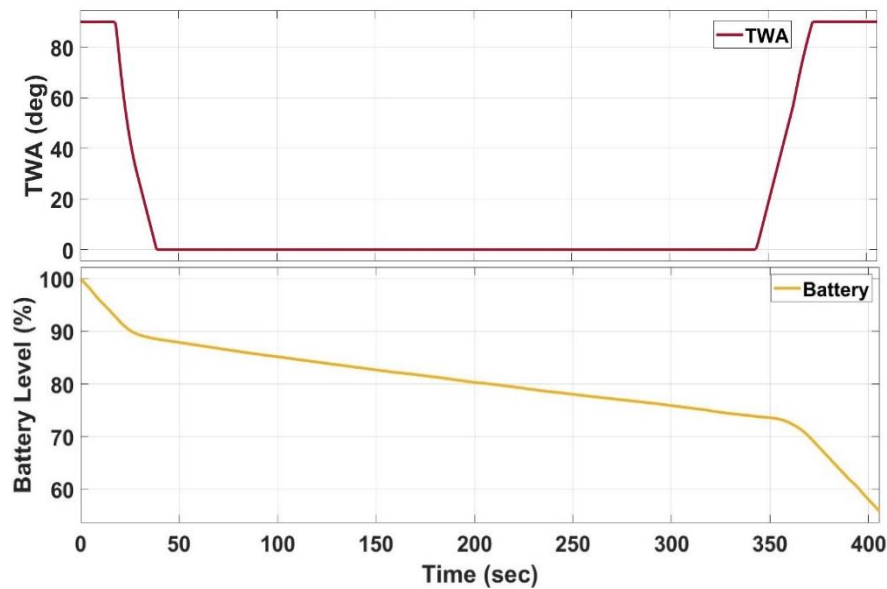


Figure 6.20. Tilt-Wing Angle and Battery Level Time Histories during the Mission

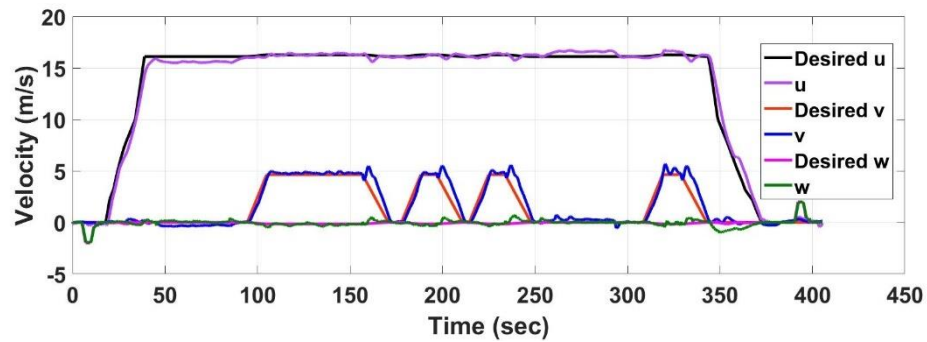


Figure 6.21. Desired and Actual Body Velocities During the Mission

Figure 6.21 shows that the desired and actual velocities are in good correlation. There can be small differences due to disturbances; however, aircraft are capable of rejecting the disturbance within an acceptable level. Body velocity in the “y” direction is increasing when the aircraft starts the turn maneuvering.

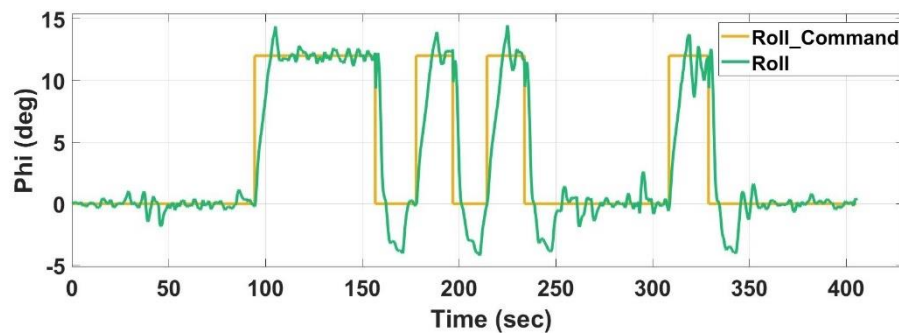


Figure 6.22. Roll Command and Roll Angle Histories During the Mission

Roll command is given when a coordinated turn is required. If the difference between the actual yaw angle and the desired yaw angle is higher than 10° , the pilot gives a roll command instead of giving yaw command. When the desired yaw angle is achieved, the pilot cancels the roll command.

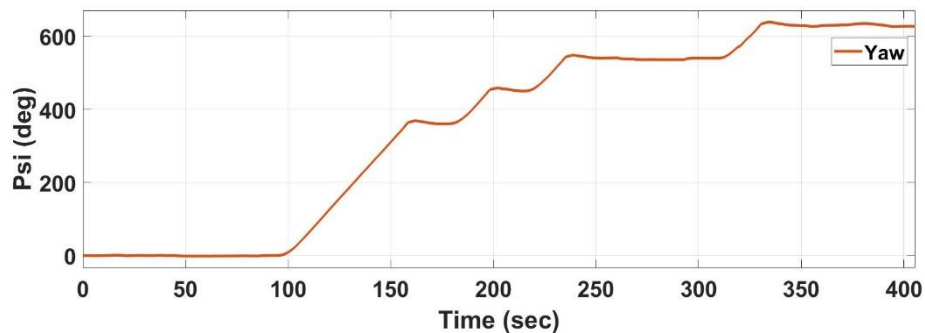


Figure 6.23. Yaw Angle History During the Mission

Figure 6.24 shows the aerodynamic surface deflections time histories. Almost maximum elevator deflection is given during the coordinated turn. Note that the disturbances cause the elevator deflection to fluctuate. In VTOL mode, aileron and elevators are almost fully deflected, since ailerons are used as flaperons in VTOL mode.

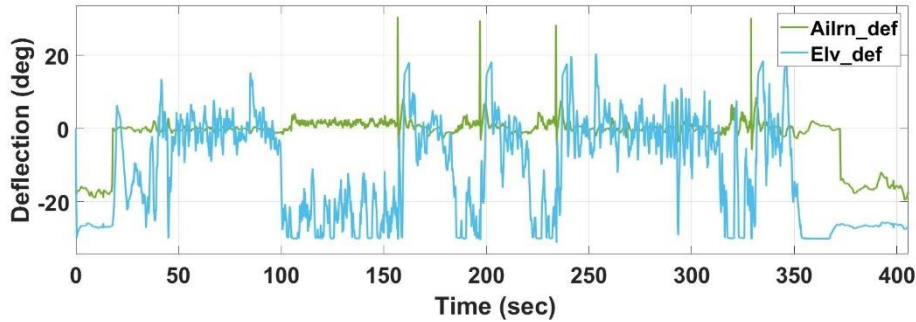


Figure 6.24. Control Surface Deflection History During the Mission

Front and rear motor angular velocities are given in Figure 6.25 and 6.26, respectively. Left and right motors angular velocities are differentiating from each other when yaw moment is needed in forward flight mode and when yaw and roll moment is needed in forward flight, transition, and VTOL mode. In forward flight, rear motors are shut down.

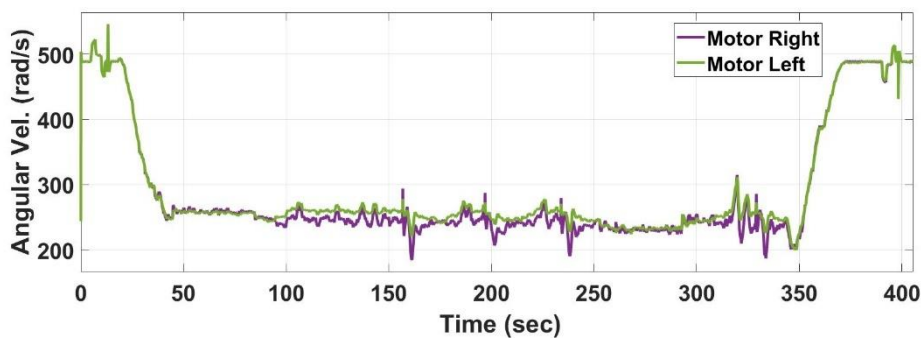


Figure 6.25. Front Motor Angular Velocity Time History During the Mission

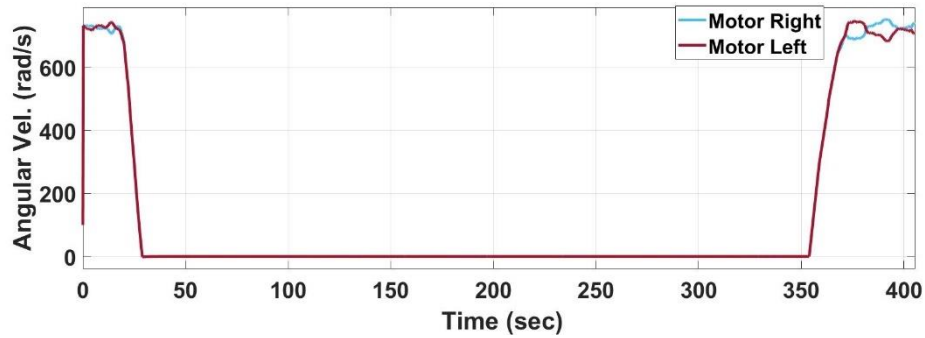


Figure 6.26. Rear Motor Angular Velocity Time History During the Mission

6.7 Vulnerability Analysis Against Parameter Variations

Non-linear six DoF model is good as how much it is close to the real plant. However, in real life, there will always be a deviation from the simulation world since there are several assumptions made while developing the six DoF model. Even if no assumption has been made while developing the model, there would be some differences from real-world applications.

Therefore, the controller should be robust against the uncertainties. Vulnerability analysis has been done to see how the system will behave when some parameters are changed. Figure 6.27 shows the pitch response of the aircraft in several parameter change conditions. Figure 6.27.a assumes that no error has been made when the static coefficients are obtained from CFD analysis. While Figure 6.27.b assumes that there is a 5% error, Figure 6.27.b assumes a 10% error.

System behavior against uncertainties seems good, according to Figure 6.27. Static coefficient errors change the behavior slightly while the damping derivative uncertainties are highly effective on-pitch response. If damping derivative changes, more than 10%, the system is starting to be unstable. Note that damping derivative is effecting the system behaves very much because the system is linearized around no error condition, and the system is getting far away from the trim point when these errors are made.

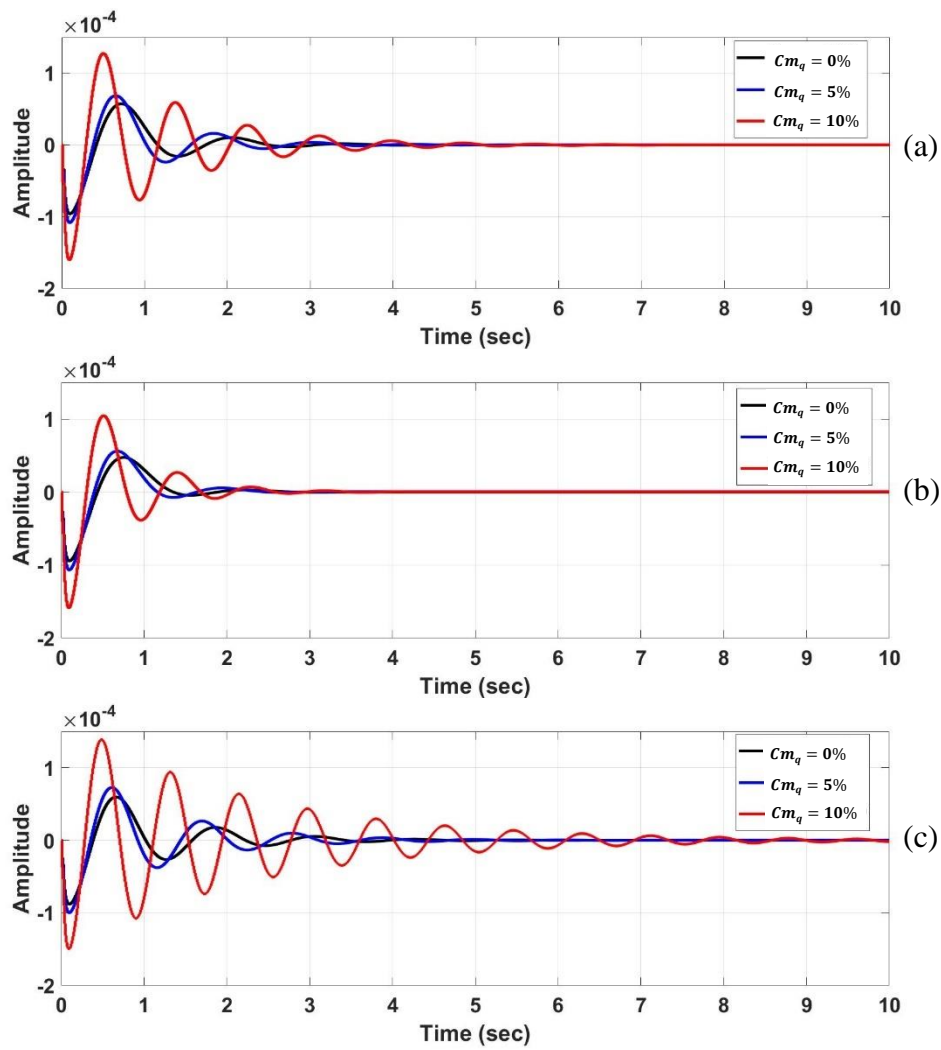


Figure 6.27. Pitch Angle Response of the Aircraft with respect to Several Parameter Changes

CHAPTER 7

CONCLUSION

In this thesis, the platform and controller design of a Tilt-Wing UAV, which is capable of doing hover, VTOL, level flight, and mode switching, is considered. In this regard, a solution approach is studied with the aim of combining the benefits of rotary and fixed-wing aircraft in one platform. Additionally, the methods for generating a non-linear model, designing controllers, are studied from existing methods for both conventional aircraft and multi-rotors.

No vertical tail has been employed for this study. 5% of weight reduction and 4% drag reduction has been achieved due to not using the vertical tail as part of this study.

In this study, the transition phase of the flight is mainly considered. The transition phase is divided into seven parts, and for each of them, a separate controller is designed. A gain scheduling algorithm is developed using look-up tables in Simulink. The air vehicle has a multi-copter configuration and is capable of taking off and landing vertically in VTOL mode. After taking off, it is starting a forward flight by tilting the wings forward. The nonlinear simulation model of the air vehicle that describes the physical properties in detail is created in the MATLAB/Simulink/Simscape environment, which consists of a propulsion model, aerodynamics model, gravity model, and the translational and rotational equations of motion. While developing the model, numerical analyses are carried out. Several linear models of the aircraft are also obtained. For this purpose, appropriate trim conditions are specified for hover, transition, and forward flight phases, separately. Linear Quadratic Regulator (LQR) and PID, controllers are designed for related linear models. The performance of the controllers against pilot commands is analyzed through nonlinear simulations, and the results are compared. The

simulation results show that the controllers developed successfully keeps its commanded states.

The platform is designed with physically integrated VTOL, transition, and Forward Flight control elements via using control allocation that enables multi-mode capability. Combining VTOL and Forward Flight modes, the aircraft is required to be operated in an extended flight envelope from hover to high-speed level flight. Therefore, the nonlinear model of the aircraft is constructed considering high α conditions, which arise from low speed over aerodynamical surfaces. A trimming algorithm in Simulink is utilized when finding trim conditions for all of the flight modes. The flight characteristics of VTOL Tilt-Wing UAV is compatible with the conventional platform types, which means that the aircraft demonstrates Rotary Wing and Fixed Wing characteristics when the corresponding mode is engaged. The analysis showed that the aircraft could be operated at close trim conditions in different modes for smooth transitions. Therefore, mode switching has been employed without stalling the wings, which is different from other platform's transition methods. Available control methods have been tailored to the aircraft characteristics to obtain a combined control structure for VTOL Tilt-Wing UAV that is capable of controlling a VTOL and Fixed Wing aircraft. They have performed well in controlling the aircraft in the whole flight envelope. Flight tests and analysis performed in the simulation environment proved that the VTOL Tilt-Wing UAV represents both VTOL and Fixed Wing capabilities in one platform. The proposed architecture of the controller system performed well in controlling the aircraft in VTOL, Forward Flight modes where switching between modes is handled by the pilot manually.

An analysis that shows the effect of CFD analysis resolution on the model accuracy has been carried out. One of the main contributions of this study is that studies showed that transition flight could be divided into five trim points instead of seven, which means that 28% of CFD runs would be decreased. It is a significant result for the literature to determine the number of CFD runs to establish an accurate nonlinear model.

The results obtained from this study reveals new objectives for future studies. The future study should include real-world flight tests of the VTOL Tilt-Wing UAV. Nonlinear controllers shall also be developed in the future, and the performance of the non-linear controllers shall be compared against the linear controllers presented in this study. More flight tests, both in simulation and real-world environments, should be conducted, including extended flight conditions for establishing more detailed implementation criteria. In order to reveal more functionalities of the platform, optimal flight maneuvers should be calculated through the utilization of redundant control elements. Several control techniques, such as linear quadratic tracking and sliding mode controller, and fault-tolerant control methods, must be applied for VTOL-Tilt-Wing in order to compare flight performance and robustness. Different mode tasking schemes should be tried in managing transition mode for optimum mission success like minimization of energy consumption, control effort, or time.

REFERENCES

- [1] D. Kurtulus, “Introduction to micro air vehicles: concepts, design and applications,” no. April 2011, pp. 219–255, 2011.
- [2] K. Nonami, F. Kendoul, S. Suzuki, W. Wang, and D. Nakazawa, “Autonomous flying robots: Unmanned aerial vehicles and micro aerial vehicles,” *Auton. Fly. Robot. Unmanned Aer. Veh. Micro Aer. Veh.*, pp. 1–329, 2010, doi: 10.1007/978-4-431-53856-1.
- [3] F. Cakici, “Control and Guidance of a Multi-Mode Unmanned Aerial Vehicle for Increased Versatility,” 2016.
- [4] R. G. Mcswain, L. J. Glaab, and C. R. Theodore, “Greased Lightning (GL-10) Performance Flight Research – Flight Data Report NASA STI Program in Profile,” no. November 2017, 2017, [Online]. Available: <https://ntrs.nasa.gov/archive/nasa/casi.ntrs.nasa.gov/20180000765.pdf>.
- [5] D. Anh, T. Isabelle, and F. Rogelio, *Modeling and Control of a Convertible Mini UAV*, vol. 44, no. 1. IFAC, 2011.
- [6] M. Hochstenbach, C. Notteboom, B. Theys, and J. De Schutter, “Design and control of an unmanned aerial vehicle for autonomous parcel delivery with transition from vertical take-off to forward flight - VertiKUL, a quadcopter tailsitter,” *Int. J. Micro Air Veh.*, vol. 7, no. 4, pp. 395–405, 2015, doi: 10.1260/1756-8293.7.4.395.
- [7] E. Cetinsoy, S. Dikyar, C. Hancer, O.K. Sirimoglu, E. Unel, M. Aksit, “Design and construction of a novel quad tilt-wing UAV,” *Mechatronics*, vol. 22, no. 6, pp. 723–745, 2012, doi: 10.1016/j.mechatronics.2012.03.003.
- [8] K. Muraoka, N. Okada, D. Kubo, and M. Daisuk, “Transition flight of quad tilt wing VTOL UAV,” *28th Congr. Int. Counc. Aeronaut. Sci. 2012, ICAS 2012*, vol. 4, pp. 3242–3251, 2012.
- [9] S. Rohde, N. Goddemeier, C. Wierfeld, F. Steinicke, K. Hinrichs, T.

- Ostermann, J. Holsten, D. Moormann, “AVIGLE: A system of systems concept for an avionic digital service platform based on micro unmanned aerial vehicles,” in *Conference Proceedings - IEEE International Conference on Systems, Man and Cybernetics*, 2010, pp. 459–466, doi: 10.1109/ICSMC.2010.5641767.
- [10] A. S. Onen, L. Cevher, M. Senipek, T. Mutlu, O. Gungor, İ. O. Uzunlar, “Modeling and controller design of a VTOL UAV,” *2015 Int. Conf. Unmanned Aircr. Syst. ICUAS 2015*, pp. 329–337, 2015, doi: 10.1109/ICUAS.2015.7152307.
- [11] S. Shkarayev, J.-M. Moschetta, and B. Bataille, “Aerodynamic Design of VTOL Micro Air Vehicles,” *3rd US-European Compet. Work. Micro Air Veh. Syst. Eur. Micro Air Veh. Conf. Flight Compet.*, no. September, pp. 1–18, 2007.
- [12] K. Muraoka, N. Okada, and D. Kubo, “Quad tilt wing VTOL UAV: Aerodynamic characteristics and prototype flight test,” *AIAA Infotech Aerosp. Conf. Exhib. AIAA Unmanned...Unlimited Conf.*, no. April, pp. 6–13, 2009.
- [13] K. C. Wong, J. A. Guerrero, D. Lara, and R. Lozano, “Attitude stabilization in hover flight of a mini tail-sitter UAV with variable pitch propeller,” *IEEE Int. Conf. Intell. Robot. Syst.*, no. May 2014, pp. 2642–2647, 2007, doi: 10.1109/IROS.2007.4399278.
- [14] R. H. Stone, “The T-Wing tail-sitter unmanned air vehicle: From design concept to research flight vehicle,” *Proc. Inst. Mech. Eng. Part G J. Aerosp. Eng.*, vol. 218, no. 6, pp. 417–433, 2004, doi: 10.1243/0954410042794920.
- [15] U. Ozdemir, Y.O. Aktas, A. Vuruskan, Y. Dereli, “Design of a commercial hybrid VTOL UAV system,” *J. Intell. Robot. Syst. Theory Appl.*, vol. 74, no. 1–2, pp. 371–393, 2014, doi: 10.1007/s10846-013-9900-0.
- [16] J. H. Lee, B. M. Min, E. T. Kim, “Autopilot design of tilt-rotor UAV using particle swarm optimization method,” *ICCAS 2007 - Int. Conf. Control.*

Autom. Syst., pp. 1629–1633, 2007, doi: 10.1109/ICCAS.2007.4406594.

- [17] J.D. Claridge and C. Manning, “X Plus One UAV.” <http://www.xcraft.io/> (accessed May 09, 2018).
- [18] Arcturus UAV, “Jump 20.” <http://arcturus-uav.com/product/JUMP-20> (accessed May 09, 2018).
- [19] Conquest Ventures, “Vertex VTOL Hybrid UAV.” <http://www.comquestventures.com/> (accessed May 09, 2018).
- [20] K. A. S. LLC, “Skyprowler UAV.” <http://www.krossblade.com/#skyprowler-section> (accessed May 09, 2018).
- [21] E. Feron, "*Autonomous Guidance of Agile Small-Scale Rotorcraft*", Massachusetts Institute of Technology, Massachusetts, USA, 2004.
- [22] X. Wu and Y. Liu, “Trajectory tracking control of quadrotor UAV,” *Chinese Control Conf. CCC*, vol. 2018-July, pp. 10020–10025, 2018, doi: 10.23919/ChiCC.2018.8482939.
- [23] A. B. Milhim, Y. Zhang, and C. A. Rabbath, “Gain scheduling based PID controller for fault tolerant control of a quad-rotor UAV,” *AIAA Infotech Aerosp. 2010*, no. April, pp. 1–13, 2010.
- [24] D. P. Boyle and G. E. Chamitoff, “Autonomous maneuver tracking for self-piloted vehicles,” *J. Guid. Control. Dyn.*, vol. 22, no. 1, pp. 58–67, 1999, doi: 10.2514/2.4371.
- [25] K. T. Oner, “Modeling and Control of a New ` with Unmanned Aerial Vehicle (SUAVI) Tilt-Wing Mechanism,” 2009.
- [26] D. A. Ta, I. Fantoni, and R. Lozano, *Modeling and control of a convertible mini-UAV*, vol. 44, no. 1 PART 1. IFAC, 2011.
- [27] A.S. Onen, L. Cevher, M. Senipek, T. Mutlu, O. Gungor, İ. O. Uzunlar, “Modeling and controller design of a VTOL UAV,” *2015 Int. Conf.*

Unmanned Aircr. Syst. ICUAS 2015, no. March, pp. 329–337, 2015, doi: 10.1109/ICUAS.2015.7152307.

- [28] M. U. T. Matsumoto, K. Kita, R. Suzuki, A. Oosedo, Y. Hoshino, “A Hovering Control Strategy for a Tail-Sitter VTOL UAV that Increases Stability Against Large Disturbance,” *2010 IEEE International Conference on Robotics and Automation*, 2010.
- [29] J. Escareño, S. Salazar, and R. Lozano, “Modelling and control of a convertible VTOL aircraft,” *Proc. IEEE Conf. Decis. Control*, pp. 69–74, 2006, doi: 10.1109/cdc.2006.376915.
- [30] O. Garcia, A. Sanchez, J. Escareño, and R. Lozano, *Tail-sitter UAV having one tilting rotor: Modeling, Control and Real-Time Experiments*, vol. 41, no. 2. IFAC, 2008.
- [31] R.H. Stone, “Control architecture for a tail-sitter unmanned air vehicle,” 2004 5th Asian Control Conference (IEEE Cat. No.04EX904), Melbourne, Victoria, Australia, 2004, pp. 736-744 Vol.2.
- [32] R. H. Stone, P. Anderson, C. Hutchison, A. Tsai, P. Gibbens, and K. C. Wong, “Flight testing of the T-wing tail-sitter unmanned air vehicle,” *J. Aircr.*, vol. 45, no. 2, pp. 673–685, 2008, doi: 10.2514/1.32750.
- [33] D. Kubo, “Study on Design and Transitional Flight of Tail-Sitting Vtol Uav,” *Int. Congr. Aeronaut. Sci.*, 2006.
- [34] J. V. Hogge, “Development of a Miniature VTOL Tailsitter Unmanned Aerial Vehicle,” 2008.
- [35] W. E. Green and P. Y. Oh, “A MAV that flies like an airplane and hovers like a helicopter,” *IEEE/ASME Int. Conf. Adv. Intell. Mechatronics, AIM*, vol. 1, pp. 693–698, 2005.
- [36] W. E. Green and P. Y. Oh, “Autonomous Hovering of a Fixed-Wing Micro Air Vehicle Drexel Autonomous Systems Lab Drexel University ,

- Philadelphia , PA Hovering a Fixed-Wing MAV,” in *IEEE International Conference on Robotics and Automation*, 2006, no. May, pp. 2164–2169.
- [37] Y. Jung, D. H. Shim, and N. Ananthkrishnan, “Controller synthesis and application to hover-to-cruise transition flight of a Tail Sitter UAV,” in *AIAA Atmospheric Flight Mechanics Conference 2010*, 2010, no. August, pp. 1–24.
- [38] X. Wang and H. Lin, “Design and control for rotor-fixed wing hybrid aircraft,” *Proc. Inst. Mech. Eng. Part G J. Aerosp. Eng.*, vol. 225, no. 7, pp. 831–847, 2011, doi: 10.1177/2041302510394742.
- [39] N. B. Knoebel and T. W. McLain, “Adaptive quaternion control of a miniature tailsitter UAV,” *Proc. Am. Control Conf.*, no. August, pp. 2340–2345, 2008, doi: 10.1109/ACC.2008.4586841.
- [40] M. Aksugur, G. Inalhan, and R. Beard, “Hybrid propulsion system design of a VTOL tailsitter UAV,” *SAE Tech. Pap.*, no. August, 2008, doi: 10.4271/2008-01-2242.
- [41] M. Aksugur and G. Inalhan, “Design methodology of a hybrid propulsion driven electric powered miniature tailsitter unmanned aerial vehicle,” *J. Intell. Robot. Syst. Theory Appl.*, vol. 57, no. 1–4, pp. 505–529, 2010, doi: 10.1007/s10846-009-9368-0.
- [42] ANSYS,2018,[Online].
Available: <https://www.ansys.com/products/fluids/ansys-fluent>.
- [43] S. I. I. U. Nunoa, “2010 Design Build and Fly Competition Top Scored Reports,” *Arh. Hig. Rada Toksikol.*, vol. 60, no. 4, pp. 982–992, 2010, doi: 10.1093/occmed/kqq062.
- [44] D. P. Raymer, “Aircraft design: A conceptual approach[Book],” *Washington, DC Am. Inst. Aeronaut. Astronaut. Inc, 1992.*, 1992.
- [45] XFLR5, [Online]. Available: <http://www.xflr5.tech/xflr5.htm>.

- [46] Y. Chen, A. Dore, and R. Jumpertz, “Graduate Team Aircraft Design Competition : Electric Vertical Takeoff and Landing (E-VTOL) Aircraft Mistral Air Taxi,” 2019.
- [47] S. Suzuki, R. Zhijia, Y. Horita, and K. Nonami, “Design and Attitude Control of Quad Rotors QTW-UAV with Tilt Wing Mechanism *,” vol. 4, no. 3, pp. 2012–2019, 2019, doi: 10.1299/jsdd.4.416.
- [48] Neu Motors, <https://www.ecalc.ch/motorcalc.php> (accessed Feb. 21, 2019).
- [49] E. Cetinsoy, C. Hancer, K. T. Oner, E. Sirimoglu, and M. Unel, “Aerodynamic design and characterization of a quad tilt-wing UAV via wind tunnel tests,” *J. Aerosp. Eng.*, vol. 25, no. 4, pp. 574–587, 2012, doi: 10.1061/(ASCE)AS.1943-5525.0000161.
- [50] D.P. Raymer, *Enhancing Aircraft Conceptual Design Using Multidisciplinary Optimization*, no. May. 2002.
- [51] R. Guzman, “A coordinated turn controller for a fixed-wing aircraft,” vol. 0, no. 2508, pp. 1–13, 2018, doi: 10.1177/0954410018761967.
- [52] S. Srinathkumar, *Eigenstructure Control Algorithms Eigenstructure Control Algorithms*.
- [53] S. Jafari, P. A. Ioannou, and L. Rudd, “What is L 1 Adaptive Control,” pp. 1–9, 2013.
- [54] L. Lublin and M. Athans, “Linear quadratic regulator control,” in *The Control Systems Handbook: Control System Advanced Methods, Second Edition*, 2010, pp. 375–400.
- [55] K. Masuda and K. Uchiyama, “Robust control design for Quad Tilt-Wing UAV,” *Aerospace*, vol. 5, no. 1, 2018, doi: 10.3390/aerospace5010017.
- [56] Y. Yildiz, M. Unel, and A. E. Demirel, “Nonlinear hierarchical control of a quad tilt-wing UAV: An adaptive control approach,” *Int. J. Adapt. Control*

- Signal Process.*, vol. 31, no. 9, pp. 1245–1264, 2017, doi: 10.1002/acs.2759.
- [57] A. R. Serrano, “Design methodology for hybrid (VTOL + Fixed Wing) unmanned aerial vehicles,” *Aeronaut. Aerosp. Open Access J.*, vol. 2, no. 3, pp. 165–176, 2018, doi: 10.15406/aaaj.2018.02.00047.
 - [58] J. McArthur, “Aerodynamics of wings at low reynolds numbers,” *Training*, no. May, p. 163, 2007, [Online]. Available: <http://digitallibrary.usc.edu/assetserver/controller/item/usctheses-m378/etd-Yates-20070411.pdf>.
 - [59] S. Yazırlı, “Development of a Conceptual Design Tool and Calculation of Stability and Control Derivatives for Mini UAV Systems,” 2015.
 - [60] J. D. Barton, “Fundamentals of small unmanned aircraft flight,” *Johns Hopkins APL Tech. Dig. (Applied Phys. Lab.*, vol. 31, no. 2, pp. 132–149, 2012.
 - [61] A. Güçlü, K. B. Arıkan, and D. F. Kurtuluş, “Attitude and altitude stabilization of a fixed wing VTOL unmanned air vehicle,” *AIAA Model. Simul. Technol. Conf. 2016*, no. June, pp. 1–13, 2016, doi: 10.2514/6.2016-3378.
 - [62] E. Çetinsoy, “Design, Construction and Flight Control of a Quad Tilt-Wing Unmanned Aerial Vehicle,” 2010.
 - [63] M. Drela, “Flight Dynamics and Control Overview,” no. 1, pp. 1–8.
 - [64] J. Lee, C. Yoo, Y. Park, B. Park “An experimental study on time delay control of actuation system of tilt rotor unmanned aerial vehicle,” *Mechatronics*, vol. 22, no. 2, pp. 184–194, 2012, doi: 10.1016/j.mechatronics.2012.01.005.
 - [65] S. Choi, Y. Kang, S. Chang, S. Koo, and J. M. Kim, “Development and conversion flight test of a small tiltrotor unmanned aerial vehicle,” *J. Aircr.*, vol. 47, no. 2, pp. 730–732, 2010, doi: 10.2514/1.46180.
 - [66] S. Park, J. Bae, Y. Kim, and S. Kim, “Fault tolerant flight control system for

- the tilt-rotor UAV,” *J. Franklin Inst.*, vol. 350, no. 9, pp. 2535–2559, 2013, doi: 10.1016/j.jfranklin.2013.01.014.
- [67] M. Science, “Naira Hovakimyan,” 1997.
- [68] Y. Kang, B. Park, C. Yoo, Y. Kim, and S. Koo, “Flight test results of automatic tilt control for small scaled tilt rotor aircraft,” *2008 Int. Conf. Control. Autom. Syst. ICCAS 2008*, pp. 47–51, 2008, doi: 10.1109/ICCAS.2008.4694527.
- [69] Y. Kang, B. Park, C. Yoo, and S. Koo, “Control law modification according to flight test of small scaled tilt rotor UAV,” *AIAA Guid. Navig. Control Conf. Exhib.*, no. August, pp. 1–8, 2008.
- [70] M. Kim, S. Kim, W. Kim, C. Kim, and Y. Kim, “Flow control of tiltrotor unmanned-aerial-vehicle airfoils using synthetic jets,” *J. Aircr.*, vol. 48, no. 3, pp. 1045–1057, 2011, doi: 10.2514/1.C031225.
- [71] E. Cetinsoy, S. Dikyar, C. Hancer, K. Oner, “Design and construction of a novel quad tilt-wing UAV,” *Mechatronics*, vol. 22, no. 6, pp. 723–745, 2012, doi: 10.1016/j.mechatronics.2012.03.003.
- [72] V. Dwivedi and M. Damodaran, “Computational aeromechanics of a maneuvering unmanned aerial vehicle with variable-incidence wings,” *J. Aircr.*, vol. 52, no. 6, pp. 1914–1926, 2015, doi: 10.2514/1.C033102.
- [73] W. J. Fredericks, R. G. McSwain, B. F. Beaton, D. W. Klassman, and C. R. Theodore, “Greased Lightning (GL-10) Flight Testing Campaign,” no. July 2017, 2017, [Online]. Available: file:///H:/FLEXOP/Literature/FLEXOP Attachments/20170007194.pdf M4 - Citavi.
- [74] V. Hrishikeshavan, C. Bogdanowicz, and I. Chopra, “Experimental investigation of performance of a wing-propeller system for a quad-rotor-biplane micro air vehicle,” *Collect. Tech. Pap. - AIAA/ASME/ASCE/AHS/ASC Struct. Struct. Dyn. Mater. Conf.*, 2013.

- [75] T. Yucelen and W. M. Haddad, "A robust adaptive control architecture for disturbance rejection and uncertainty suppression with L_∞ transient and steady-state performance guarantees," *Int. J. Adapt. Control Signal Process.*, vol. 26, no. 11, pp. 1024–1055, 2012, doi: 10.1002/acs.2281.
- [76] P. M. Rothhaar, "NASA langley distributed propulsion VTOL tilt-wing aircraft testing, modeling, simulation, control, and flight test development," *AIAA Aviat. 2014 -14th AIAA Aviat. Technol. Integr. Oper. Conf.*, no. June, pp. 1–14, 2014.
- [77] A. Kutluk, "Hibrit insansiz hava aracinin yönelim dinamiklerinin hibrit denetimi," pp. 1–7, 2016.
- [78] M. Mendes and D. A. Neto, "Control Strategies of a Tilt-rotor UAV for Load Transportation Marcelino Mendes de Almeida Neto," 2014.
- [79] A. T. Tran, N. Sakamoto, M. Sato, and K. Muraoka, "Control Augmentation System Design for Quad-Tilt-Wing Unmanned Aerial Vehicle via Robust Output Regulation Method," *IEEE Trans. Aerosp. Electron. Syst.*, vol. 53, no. 1, pp. 357–369, 2017, doi: 10.1109/TAES.2017.2650618.
- [80] D. Kaya, A. T. Kutay, D.F. Kurtulus, O. Tekinalp, "Propulsion system selection and modeling for a quadrotor with search and rescue mission," *54th AIAA Aerosp. Sci. Meet.*, no. January, pp. 1–10, 2016, doi: 10.2514/6.2016-1528.
- [81] J. J. Dickeson, O. Cifdaloz, D. W. Miles, P. M. Koziol, V. L. Wells, and A. A. Rodriguez, "Robust H_∞ gain-scheduled conversion for a tilt-wing rotorcraft," *Proc. IEEE Conf. Decis. Control*, pp. 5882–5887, 2006.
- [82] A. Deperrois, "About stability analysis using XFLR5," *ReVision*, no. November, 2010.
- [83] E. Çetinsoy, E. Sirimoğlu, K. Oner, C. Hancer, "Design and development of a tilt-wing UAV," *Turkish J. Electr. Eng. Comput. Sci.*, vol. 19, no. 5, pp.

733–741, 2011, doi: 10.3906/elk-1007-621.

- [84] Z. Liu, Y. He, L. Yang, and J. Han, “Control techniques of tilt rotor unmanned aerial vehicle systems: A review,” *Chinese J. Aeronaut.*, vol. 30, no. 1, pp. 135–148, 2017, doi: 10.1016/j.cja.2016.11.001.
- [85] D. Harris, “*Aircraft Control*” 2011.
- [86] S. Hong, J. Jeong, S. Kim, J. Suk, and J. I. Jung, *Longitudinal flight dynamics of a single tilt-wing unmanned aerial vehicle*, vol. 19, no. PART 1. IFAC, 2013.
- [87] C. Hancer, K. T. Oner, E. Sirimoglu, E. Cetinsoy, and M. Unel, “Robust hovering control of a quad tilt-wing UAV,” *IECON Proc. (Industrial Electron. Conf.)*, pp. 1615–1620, 2010, doi: 10.1109/IECON.2010.5675441.
- [88] E. Cetinsoy, C. Hancer, K. T. Oner, E. Sirimoglu, and M. Unel, “Aerodynamic design and characterization of a quad tilt-wing UAV via wind tunnel tests,” *J. Aerosp. Eng.*, vol. 25, no. 4, pp. 574–587, 2012, doi: 10.1061/(ASCE)AS.1943-5525.0000161.
- [89] S. G. Kontogiannis and J. A. Ekaterinaris, “Design, performance evaluation and optimization of a UAV,” *Aerosp. Sci. Technol.*, vol. 29, no. 1, pp. 339–350, 2013, doi: 10.1016/j.ast.2013.04.005.
- [90] C. Hancer, K. T. Oner, E. Sirimoglu, E. Cetinsoy, and M. Unel, “Robust position control of a tilt-wing quadrotor,” *Proc. IEEE Conf. Decis. Control*, pp. 4908–4913, 2010, doi: 10.1109/CDC.2010.5717283.
- [91] J. Holsten, T. Ostermann, and D. Moormann, “Design and wind tunnel tests of a tiltwing UAV,” *CEAS Aeronaut. J.*, vol. 2, no. 1–4, pp. 69–79, 2011, doi: 10.1007/s13272-011-0026-4.
- [92] K. Nonami, F. Kendoul, S. Suzuki, W. Wang, and D. Nakazawa, *Autonomous flying robots: Unmanned aerial vehicles and micro aerial vehicles*. 2010.

- [93] K. Oner, E. Cetinsoy, M. Unel, M. F. Aksit, I. Kandemir, and K. Gulez, "Dynamic Model and Control of a New Quadrotor Unmanned Aerial Vehicle with Tilt-Wing Mechanism.," *World Acad. Sci. Eng. Technol.*, vol. 45, no. 9, pp. 58–63, 2009.
- [94] A. Ailon, "Motion planning and optimal control of an autonomous VTOL aircraft," *IFAC Proc. Vol.*, vol. 6, no. PART 1, pp. 13–18, 2007.
- [95] C. Nicol, C. J. B. MacNab, and A. Ramirez-Serrano, "Robust adaptive control of a quadrotor helicopter," *Mechatronics*, vol. 21, no. 6, pp. 927–938, 2011, doi: 10.1016/j.mechatronics.2011.02.007.
- [96] D.P. Raymer, "Aircraft Design-A Conceptual Approach", Air force Institute of Technology, Wright-Patterson Air Force Base, Ohio, 1984.
- [97] Y. Beyer, "Simulation and Control of a Tandem Tiltwing RPAS Without Experimental Data," pp. 162–169, 2017.
- [98] "VTOL Design Problems," *Flight*, no. October, p. 1957, 1957.
- [99] K. Benkhoud, S. Bouallegue, "Modeling and LQG Controller Design for a Quad Tilt-Wing UAV", 3rd International Conference on Automation, Control and Computer Science, March, 2017.
- [100] G. Cai, B. M. Chen, and T. H. Lee, "Unmanned Rotorcraft Systems," *Media*, p. 267, 2011, doi: 10.1007/978-0-85729-635-1.
- [101] R. J. A. W. Hosman, "Control of Aircraft Motions," vol. 105, 1996.
- [102] P. M. Rothhaar, "NASA langley distributed propulsion VTOL tilt-wing aircraft testing, modeling, simulation, control, and flight test development," *AIAA Aviat. 2014 -14th AIAA Aviat. Technol. Integr. Oper. Conf.*, pp. 1–14, 2014.
- [103] M. Robert, "An analysis of the stick fixed dynamic stability of a typical VTOL aircraft during transition flight out of ground effect," 1965.

- [104] D. Caughey, "Introduction to Aircraft Stability and Control Course Notes," *Sibley Sch. Mech. Aerosp. Eng. Cornell Univ.*, p. 153, 2011, doi: 10.1038/172515b0.
- [105] J. Holsten, P. Hartmann, and D. Moormann, "Modeling of tiltwing aircraft dynamics as linear system," no. 2012, 2016.
- [106] D. L. Blount, "dynamic Stability Prgram," 2009, [Online]. Available: http://www.dlba-inc.com/Dynamic_Stability_Calculator.aspx.
- [107] J. Holsten and D. Moormann, "Flight control law design criteria for the transition phase for a tiltwing aircraft using multi-objective parameter synthesis," *CEAS Aeronaut. J.*, vol. 6, no. 1, pp. 17–30, 2014, doi: 10.1007/s13272-014-0126-z.
- [108] W. Ko, K. Oo, H. M. Tun, Z. M. Naing, and W. K. Moe, "Design Of Vertical Take-Off And Landing (VTOL) Aircraft System," *Int. J. Sci. Technol. Res.*, vol. 6, no. 4, pp. 179–183, 2017.
- [109] D. A. Caughey, "Dynamical Equations for Flight Vehicles," 2011, [Online]. Available: <https://courses.cit.cornell.edu/mae5070/DynamicEquations.pdf>.
- [110] J. D. Anderson, *Fundamentals of Aerodynamics*, vol. 53, no. 9. 2013.
- [111] C. A. Lyon, A. P. Broeren, P. Giguere, A. Gopalarathnam, and M. S. Selig, *Summary of Low-Speed Airfoil Data - Volume 3*, vol. 3. 1997.
- [112] S. C. Kriel, "A comparison of control systems for the flight transition of VTOL unmanned aerial vehicles," no. March, 2008, [Online]. Available: <http://scholar.sun.ac.za/handle/10019.1/1535>.
- [113] J. G. Wozniak, "Nonlinear Six Degree Of Freedom Simulation Of A Twin Jet Engine Transport Aircraft," 1997.
- [114] J. Fritz, D.H. Russ, "A Nonlinear Flight Controller Design for an Advanced Flight Control Test Bed by Trajectory Linearization Method," 2004.

- [115] A. Ferrarelli, D. Caporale, A. Settimi, and L. Pallottino, “APRICOT: Aerospace prototyping control toolbox. A modeling and simulation environment for aircraft control design,” *Lect. Notes Comput. Sci. (including Subser. Lect. Notes Artif. Intell. Lect. Notes Bioinformatics)*, vol. 9991 LNCS, pp. 139–157, 2016, doi: 10.1007/978-3-319-47605-6_11.
- [116] P. Murrieri, “Design and Control of an Experimental Tiltwing Aircraft,” no. April, pp. 4393–4398, 2004, doi: 10.1109/ROBOT.2004.1302409.
- [117] F. Saghafi, “Development of a Simulation Tool for Flight Dynamics and Control Investigations of Articulated VTOL Unmanned Aircraft,” 1996.
- [118] F. S. Time and R. Free, “Hybrid simulation of a controlled system,” pp. 1–22.
- [119] M. Bodson and M. Athans, “Multivariable Control of Vtol Aircraft for Shipboard Landing.,” *AIAA Pap.*, no. April, pp. 473–481, 1985.
- [120] R. V. Ramnath, “Transition dynamics of VTOL aircraft,” *AIAA J.*, vol. 8, no. 7, pp. 1214–1221, 1970, doi: 10.2514/3.5875.
- [121] B. Theys, G. De Vos, and J. De Schutter, “A control approach for transitioning VTOL UAVs with continuously varying transition angle and controlled by differential thrust,” *2016 Int. Conf. Unmanned Aircr. Syst. ICUAS 2016*, pp. 118–125, 2016, doi: 10.1109/ICUAS.2016.7502519.
- [122] V. I. George, C. P. Kurian, J. D’Souza, and I. Thirunavukkarasu, “A Simulink model for an aircraft landing system using energy functions,” *Proc. 2012 7th IEEE Conf. Ind. Electron. Appl. ICIEA 2012*, no. July, pp. 355–360, 2012, doi: 10.1109/ICIEA.2012.6360752.
- [123] A. S. Saeed, A. B. Younes, S. Islam, J. Dias, L. Seneviratne, and G. Cai, “A review on the platform design, dynamic modeling and control of hybrid UAVs,” *2015 Int. Conf. Unmanned Aircr. Syst. ICUAS 2015*, pp. 806–815, 2015, doi: 10.1109/ICUAS.2015.7152365.
- [124] U. Ahmed, “3-DOF Longitudinal Flight Simulation Modeling And Design

- Using MATLAB / SIMULINK,” *Ryerson Univ.*, p. 54, 2012, [Online]. Available: <http://digitalcommons.ryerson.ca/dissertations>.
- [125] J. Jeong, S. Yoon, S. Kim, and J. Suk, “Dynamic modeling and analysis of a single tilt-wing unmanned aerial vehicle,” *AIAA Model. Simul. Technol. Conf. 2015*, no. January, pp. 1–12, 2015.
- [126] T. Ostermann, J. Holsten, Y. Dobrev, and D. Moormann, “Control concept of a tiltwing UAV during low speed manoeuvring,” *28th Congr. Int. Counc. Aeronaut. Sci. 2012, ICAS 2012*, vol. 4, pp. 3232–3241, 2012.
- [127] P. Nu, W. Lin, N. L. Kham, and H. M. Tun, “Longitudinal And Lateral Dynamic System Modeling Of A Fixed-Wing UAV,” *Int. J. Sci. Technol. Res.*, vol. 6, no. 4, pp. 171–174, 2017.
- [128] K. Barnstorff, “Ten-engine electric plane prototype takes off,” no. May, pp. 3–5, 2015.
- [129] H. Çakır; D. Kurtuluş, “Hovering Control of A Tilt-Wing UAV,” in *Hovering Control of A Tilt-Wing UAV*, 2019, no. September, pp. 1–19.
- [130] A. L’Afflito, *Equations of motion of an aircraft*, no. 9783319474663. 2017.
- [131] W. J. Fredericks, D. D. North, M. A. Agate, and Z. R. Johns, “NASA GL-10 Tilt-Wing VTOL UAS Flight Validation Experiments,” pp. 1–24, 2015.
- [132] M. S. Selig, “AIAA Atmospheric Flight Mechanics 2010 Conference Modeling Propeller Aerodynamics and Slipstream Effects on Small UAVs in Realtime,” *AIAA Atmos. Flight Mech. 2010 Conf.*, pp. 1–23, 2010, doi: 10.2514/6.2010-7938.
- [133] J. Roskam, *Methods for Estimating Stability and Control Derivatives of Conventional Subsonic Airplanes*, Roskam Aviation and Engineering Corporation, Lawrence, Kansas, 1971.
- [134] L. Brian, F. Stevens, L. Lewis, N. Johnson, " Aircraft Control and Simulation:

Dynamics, Controls Design, and Autonomous Systems: Dynamics, Controls Design, and Autonomous Systems, Third Edition", 2015.

- [135] M. E. Ece, "AERO01 : Vertical Take-Off and Landing (VTOL)," pp. 1–11, 2017.
- [136] J. M. de Jong, "Model-Based Flight Control for a VTOL Aircraft with Independently Tilting Rotors", Delft University of Technology, 2019
- [137] P. Casau, "Autonomous Transition Flight for a Vertical Take-Off and Landing aircraft," 2011 50th IEEE Conference on Decision and Control and European Control Conference, Orlando, FL, 2011, pp. 3974-3979, doi: 10.1109/CDC.2011.6160819.
- [138] S. J. Miller, "Adaptive Wing Structures for Aeroelastic Drag Reduction and Loads Alleviation," no. September, 2010.
- [139] I. M. Gregory, "Adaptive Flight Control System : Flight Evaluation and Technology Transition", American Institute of Aeronautics and Astronautics, 2019.
- [140] S. R. Whyte, "Flight Characteristics of a Tilt-Wing, Distributed-Propulsion, Vertical Take-off and Landing Aircraft Concept," 2018.
- [141] J. Paul, "A Qualitative Discussion of the Stability and Control of VTOL Aircraft During Hover (out of ground effect) and Transition," 1964.

APPENDICES

A. Aerodynamic Database

Table A.1 Aerodynamic Coefficients for $TWA = 0^\circ$

Lift Coefficient					
	-30	-15	0	15	30
-14	-0,3231	-0,2632	-0,205	-0,2632	-0,3231
-12	-0,2338	-0,1974	-0,1416	-0,1974	-0,2338
-10	-0,1631	-0,119	-0,0944	-0,119	-0,1631
-8	-0,0294	-0,0358	-0,0203	-0,0358	-0,0294
-6	0,10095	0,09033	0,07454	0,09033	0,10095
-4	0,25115	0,23054	0,22627	0,23054	0,25115
-2	0,41899	0,45524	0,46246	0,45524	0,41899
0	0,59503	0,70449	0,7607	0,70449	0,59503
2	0,7338	0,89946	0,98536	0,89946	0,7338
4	0,8695	1,06919	1,17346	1,06919	0,8695
6	1,00692	1,22443	1,34189	1,22443	1,00692
8	1,12844	1,37373	1,49304	1,37373	1,12844
10	1,23314	1,5055	1,62963	1,5055	1,23314
12	1,35996	1,61195	1,74486	1,61195	1,35996
14	1,45427	1,68956	1,82773	1,68956	1,45427
16	1,53283	1,70003	1,87063	1,70003	1,53283
18	1,60667	1,74404	1,81268	1,74404	1,60667
20	1,58396	1,74275	1,83458	1,74275	1,58396

Drag Coefficient					
	-30	-15	0	15	30
-14	0,13682	0,21783	0,23567	0,21783	0,13682
-12	0,11033	0,18925	0,20174	0,18925	0,11033
-10	0,08818	0,15705	0,17509	0,15705	0,08818
-8	0,06223	0,13257	0,14478	0,13257	0,06223
-6	0,04118	0,1036	0,12174	0,1036	0,04118
-4	0,02305	0,07947	0,10389	0,07947	0,02305
-2	0,01172	0,06715	0,09087	0,06715	0,01172
0	0,0156	0,06909	0,08915	0,06909	0,0156
2	0,02472	0,08281	0,10527	0,08281	0,02472
4	0,03601	0,10028	0,12551	0,10028	0,03601
6	0,04939	0,11979	0,14888	0,11979	0,04939
8	0,06442	0,14241	0,17519	0,14241	0,06442
10	0,08105	0,16795	0,20441	0,16795	0,08105
12	0,09884	0,19633	0,23671	0,19633	0,09884
14	0,12113	0,22911	0,27523	0,22911	0,12113
16	0,14985	0,26822	0,32609	0,26822	0,14985
18	0,1866	0,31041	0,36766	0,31041	0,1866
20	0,23939	0,36247	0,41807	0,36247	0,23939

Roll Coefficient					
	-30	-15	0	15	30
-14	-0,022	-0,027	0	0,027	0,02203
-12	-0,0197	-0,0198	0	0,01984	0,01966
-10	-0,0142	-0,0147	0	0,01468	0,01422
-8	-0,0107	-0,0111	0	0,01109	0,01067
-6	-0,0063	-0,0068	0	0,00684	0,00628
-4	-0,0056	-0,006	0	0,00603	0,00564
-2	-0,0117	-0,0085	0	0,00848	0,01167
0	-0,0025	-0,0044	0	0,00442	0,00254
2	0,00086	0,00083	0	-0,0008	-0,0009
4	0,00372	0,00499	0	-0,005	-0,0037
6	0,0082	0,00926	0	-0,0093	-0,0082
8	0,01478	0,01339	0	-0,0134	-0,0148
10	0,02091	0,01694	0	-0,0169	-0,0209
12	0,02649	0,02292	0	-0,0229	-0,0265
14	0,03372	0,02999	0	-0,03	-0,0337
16	0,04057	0,03589	0	-0,0359	-0,0406
18	0,04716	0,04335	0	-0,0434	-0,0472
20	0,05116	0,05639	0	-0,0564	-0,0512

Pitch Coefficient					
	-30	-15	0	15	30
-14	0,22542	0,273	0,27156	0,273	0,22542
-12	0,16887	0,24135	0,2691	0,24135	0,16887
-10	0,17373	0,19486	0,27273	0,19486	0,17373
-8	0,11357	0,16245	0,20743	0,16245	0,11357
-6	0,06186	0,11582	0,14683	0,11582	0,06186
-4	-0,0069	0,0703	0,06541	0,0703	-0,0069
-2	-0,075	0,00329	0,02703	0,00329	-0,075
0	-0,0661	-0,0299	-0,0196	-0,0299	-0,0661
2	-0,0651	-0,0454	-0,0498	-0,0454	-0,0651
4	-0,0593	-0,0563	-0,0582	-0,0563	-0,0593
6	-0,0737	-0,071	-0,0654	-0,071	-0,0737
8	-0,0867	-0,0888	-0,087	-0,0888	-0,0867
10	-0,0994	-0,1145	-0,1245	-0,1145	-0,0994
12	-0,1335	-0,1326	-0,1693	-0,1326	-0,1335
14	-0,1522	-0,1569	-0,2048	-0,1569	-0,1522
16	-0,1886	-0,2078	-0,2497	-0,2078	-0,1886
18	-0,2305	-0,257	-0,355	-0,257	-0,2305
20	-0,3086	-0,3456	-0,4259	-0,3456	-0,3086

Yaw Coefficient					
	-30	-15	0	15	30
-14	0,00849	0,00741	0	-0,0074	-0,0085
-12	0,01068	0,00988	0	-0,0099	-0,0107
-10	0,01212	0,00888	0	-0,0089	-0,0121
-8	0,01215	0,00915	0	-0,0092	-0,0122
-6	0,0119	0,00727	0	-0,0073	-0,0119
-4	0,01199	0,00475	0	-0,0048	-0,012
-2	0,01159	0,0051	0	-0,0051	-0,0116
0	0,01327	0,0068	0	-0,0068	-0,0133
2	0,01297	0,00816	0	-0,0082	-0,013
4	0,01196	0,00825	0	-0,0083	-0,012
6	0,01091	0,0075	0	-0,0075	-0,0109
8	0,0098	0,0064	0	-0,0064	-0,0098
10	0,00828	0,00523	0	-0,0052	-0,0083
12	0,00608	0,00436	0	-0,0044	-0,0061
14	0,00554	0,00346	0	-0,0035	-0,0055
16	0,00615	0,00118	0	-0,0012	-0,0062
18	0,00851	0,00082	0	-0,0008	-0,0085
20	0,01014	0,00279	0	-0,0028	-0,0101

Table A.2 Aerodynamic Coefficients for $TWA = 15^\circ$

Lift Coefficient					
	-30	-15	0	15	30
-14	-0.5992	-0.5374	-0.6755	-0.5374	-0.5992
-12	-0.2838	-0.3974	-0.4961	-0.3974	-0.2838
-10	-0.1973	-0.2526	-0.3123	-0.2526	-0.1973
-8	-0.0809	-0.1016	-0.1265	-0.1016	-0.0809
-6	0.04316	0.05691	0.05757	0.05691	0.04316
-4	0.17104	0.21724	0.24139	0.21724	0.17104
-2	0.29252	0.37574	0.42279	0.37574	0.29252
0	0.42008	0.53017	0.60292	0.53017	0.42008
2	0.53988	0.67868	0.77959	0.67868	0.53988
4	0.65745	0.81835	0.94954	0.81835	0.65745
6	0.77238	0.95521	1.11418	0.95521	0.77238
8	0.88087	1.08938	1.27534	1.08938	0.88087
10	0.99357	1.22026	1.43217	1.22026	0.99357
12	1.10106	1.34989	1.5854	1.34989	1.10106
14	1.20692	1.48682	1.73448	1.48682	1.20692
16	1.31421	1.62062	1.88081	1.62062	1.31421
18	1.42179	1.74761	2.02599	1.74761	1.42179
20	1.52682	1.87985	2.17182	1.87985	1.52682

Drag Coefficient					
	-30	-15	0	15	30
-14	0.17909	0.29946	0.40438	0.29946	0.17909
-12	0.08647	0.24011	0.32587	0.24011	0.08647
-10	0.06377	0.19063	0.2598	0.19063	0.06377
-8	0.03778	0.15095	0.2071	0.15095	0.03778
-6	0.01633	0.1188	0.16841	0.1188	0.01633
-4	0.00062	0.095	0.14114	0.095	0.00062
-2	-0.0094	0.07957	0.12576	0.07957	-0.0094
0	-0.0136	0.07274	0.12048	0.07274	-0.0136
2	-0.0117	0.07469	0.12693	0.07469	-0.0117
4	-0.0044	0.08487	0.14382	0.08487	-0.0044
6	0.00737	0.10169	0.16785	0.10169	0.00737
8	0.02317	0.12377	0.19762	0.12377	0.02317
10	0.04321	0.15064	0.2325	0.15064	0.04321
12	0.06703	0.18275	0.27142	0.18275	0.06703
14	0.09489	0.22051	0.31392	0.22051	0.09489
16	0.12747	0.26363	0.36048	0.26363	0.12747
18	0.16544	0.31265	0.41362	0.31265	0.16544
20	0.20907	0.36971	0.47436	0.36971	0.20907

Roll Coefficient					
	-30	-15	0	15	30
-14	-0.02124	-0.02269	0	0.022688	0.021238
-12	-0.03839	-0.01798	0	0.017984	0.038394
-10	-0.0254	-0.01467	0	0.014672	0.025402
-8	-0.01859	-0.0122	0	0.012196	0.018591
-6	-0.01319	-0.01	0	0.010003	0.013194
-4	-0.00892	-0.00766	0	0.00766	0.008918
-2	-0.00296	-0.00517	0	0.005174	0.002955
0	0.002043	-0.00222	0	0.002219	-0.00204
2	0.007515	0.001273	0	-0.00127	-0.00752
4	0.012167	0.004575	0	-0.00458	-0.01217
6	0.016605	0.007665	0	-0.00767	-0.0166
8	0.021162	0.010768	0	-0.01077	-0.02116
10	0.024675	0.014156	0	-0.01416	-0.02468
12	0.028356	0.017349	0	-0.01735	-0.02836
14	0.031849	0.019993	0	-0.01999	-0.03185
16	0.034815	0.022755	0	-0.02275	-0.03481
18	0.037353	0.025875	0	-0.02587	-0.03735
20	0.039882	0.028629	0	-0.02863	-0.03988

Pitch Coefficient					
	-30	-15	0	15	30
-14	0.27268	0.20323	0.29354	0.20323	0.27268
-12	0.12817	0.11528	0.19498	0.11528	0.12817
-10	0.08455	0.04454	0.10303	0.04454	0.08455
-8	0.02974	-0.0193	0.03019	-0.0193	0.02974
-6	-0.0242	-0.0799	-0.0271	-0.0799	-0.0242
-4	-0.0737	-0.1353	-0.077	-0.1353	-0.0737
-2	-0.12	-0.1868	-0.123	-0.1868	-0.12
0	-0.1761	-0.2363	-0.1652	-0.2363	-0.1761
2	-0.2313	-0.2872	-0.2111	-0.2872	-0.2313
4	-0.286	-0.3396	-0.2558	-0.3396	-0.286
6	-0.3398	-0.3949	-0.2993	-0.3949	-0.3398
8	-0.3917	-0.4503	-0.3434	-0.4503	-0.3917
10	-0.4465	-0.5074	-0.3894	-0.5074	-0.4465
12	-0.5005	-0.5675	-0.4378	-0.5675	-0.5005
14	-0.5562	-0.6371	-0.4901	-0.6371	-0.5562
16	-0.6179	-0.7104	-0.5498	-0.7104	-0.6179
18	-0.6862	-0.787	-0.6259	-0.787	-0.6862
20	-0.7579	-0.8774	-0.7198	-0.8774	-0.7579

Yaw Coefficient					
	-30	-15	0	15	30
-14	0.011274	0.012162	0	-0.01216	-0.01127
-12	0.014021	0.011103	0	-0.0111	-0.01402
-10	0.013586	0.009747	0	-0.00975	-0.01359
-8	0.012604	0.008561	0	-0.00856	-0.0126
-6	0.011373	0.007547	0	-0.00755	-0.01137
-4	0.010194	0.006506	0	-0.00651	-0.01019
-2	0.008617	0.005578	0	-0.00558	-0.00862
0	0.006672	0.004653	0	-0.00465	-0.00667
2	0.004546	0.003421	0	-0.00342	-0.00455
4	0.002404	0.001882	0	-0.00188	-0.0024
6	0.000227	0.000294	0	-0.00029	-0.00023
8	-0.0021	-0.0012	0	0.001204	0.002104
10	-0.00411	-0.00261	0	0.002609	0.004109
12	-0.00603	-0.00385	0	0.00385	0.006027
14	-0.00774	-0.00491	0	0.004912	0.007738
16	-0.00929	-0.00607	0	0.006075	0.009295
18	-0.01048	-0.00729	0	0.007292	0.010476
20	-0.01154	-0.00856	0	0.00856	0.01154

Table A.3 Aerodynamic Coefficients for $TWA = 30^\circ$

Lift Coefficient					
	-30	-15	0	15	30
-14	-0.49	-0.7281	-0.7052	-0.7281	-0.49
-12	-0.392	-0.5989	-0.5416	-0.5989	-0.392
-10	-0.2936	-0.4604	-0.3688	-0.4604	-0.2936
-8	-0.1889	-0.3205	-0.1959	-0.3205	-0.1889
-6	-0.0853	-0.1685	-0.0202	-0.1685	-0.0853
-4	0.01213	-0.0124	0.15461	-0.0124	0.01213
-2	0.12329	0.15197	0.33043	0.15197	0.12329
0	0.23462	0.30618	0.50423	0.30618	0.23462
2	0.34088	0.4537	0.67327	0.4537	0.34088
4	0.45565	0.60017	0.8368	0.60017	0.45565
6	0.56784	0.74274	0.99477	0.74274	0.56784
8	0.68581	0.88208	1.14847	0.88208	0.68581
10	0.80526	1.01379	1.29808	1.01379	0.80526
12	0.92549	1.15096	1.44273	1.15096	0.92549
14	1.04146	1.28531	1.58198	1.28531	1.04146
16	1.15721	1.41616	1.71618	1.41616	1.15721
18	1.26968	1.54779	1.847	1.54779	1.26968
20	1.38565	1.67945	1.97613	1.67945	1.38565

Drag Coefficient					
	-30	-15	0	15	30
-14	0.17674	0.40089	0.45505	0.40089	0.17674
-12	0.13781	0.33496	0.37612	0.33496	0.13781
-10	0.11866	0.27552	0.30666	0.27552	0.11866
-8	0.0946	0.22621	0.25057	0.22621	0.0946
-6	0.07146	0.18377	0.20561	0.18377	0.07146
-4	0.04972	0.14929	0.17333	0.14929	0.04972
-2	0.0323	0.1237	0.15153	0.1237	0.0323
0	0.01992	0.107	0.14047	0.107	0.01992
2	0.01319	0.0988	0.14018	0.0988	0.01319
4	0.01484	0.1006	0.15034	0.1006	0.01484
6	0.02259	0.10981	0.16899	0.10981	0.02259
8	0.03521	0.12441	0.19265	0.12441	0.03521
10	0.05177	0.14399	0.22199	0.14399	0.05177
12	0.07252	0.16932	0.25504	0.16932	0.07252
14	0.09669	0.19901	0.29154	0.19901	0.09669
16	0.12434	0.23301	0.3317	0.23301	0.12434
18	0.156	0.27267	0.3766	0.27267	0.156
20	0.19226	0.3188	0.42665	0.3188	0.19226

Roll Coefficient					
	-30	-15	0	15	30
-14	-0.02866	-0.0206	0	0.020603	0.028656
-12	-0.02127	-0.01643	0	0.016427	0.021271
-10	-0.01306	-0.01227	0	0.012268	0.01306
-8	-0.0084	-0.00862	0	0.008617	0.008401
-6	-0.00416	-0.00521	0	0.005213	0.004163
-4	-0.00033	-0.00203	0	0.002032	0.000335
-2	0.003466	0.000713	0	-0.00071	-0.00347
0	0.006837	0.003214	0	-0.00321	-0.00684
2	0.009807	0.006034	0	-0.00603	-0.00981
4	0.013098	0.008648	0	-0.00865	-0.0131
6	0.015453	0.011075	0	-0.01108	-0.01545
8	0.01805	0.013509	0	-0.01351	-0.01805
10	0.02043	0.016337	0	-0.01634	-0.02043
12	0.022663	0.018845	0	-0.01884	-0.02266
14	0.024825	0.021596	0	-0.0216	-0.02482
16	0.026879	0.024297	0	-0.0243	-0.02688
18	0.029478	0.026605	0	-0.0266	-0.02948
20	0.031448	0.028619	0	-0.02862	-0.03145

Pitch Coefficient					
	-30	-15	0	15	30
-14	0.1057	0.17256	0.18058	0.17256	0.1057
-12	0.13941	0.10442	0.1035	0.10442	0.13941
-10	0.09493	0.05151	0.02474	0.05151	0.09493
-8	0.06654	0.00917	-0.0331	0.00917	0.06654
-6	0.02602	-0.0359	-0.0741	-0.0359	0.02602
-4	-0.0198	-0.0758	-0.1073	-0.0758	-0.0198
-2	-0.0581	-0.1127	-0.1394	-0.1127	-0.0581
0	-0.0896	-0.1425	-0.1705	-0.1425	-0.0896
2	-0.1271	-0.1722	-0.1996	-0.1722	-0.1271
4	-0.1628	-0.2058	-0.2296	-0.2058	-0.1628
6	-0.1975	-0.2417	-0.2601	-0.2417	-0.1975
8	-0.2325	-0.2794	-0.289	-0.2794	-0.2325
10	-0.2684	-0.3183	-0.3209	-0.3183	-0.2684
12	-0.3063	-0.3594	-0.3511	-0.3594	-0.3063
14	-0.3458	-0.4019	-0.3806	-0.4019	-0.3458
16	-0.388	-0.4462	-0.4122	-0.4462	-0.388
18	-0.4339	-0.4933	-0.4522	-0.4933	-0.4339
20	-0.4849	-0.5445	-0.4984	-0.5445	-0.4849

Yaw Coefficient					
	-30	-15	0	15	30
-14	0.016424	0.018184	0	-0.01818	-0.01642
-12	0.020252	0.017761	0	-0.01776	-0.02025
-10	0.016668	0.016028	0	-0.01603	-0.01667
-8	0.015217	0.014398	0	-0.0144	-0.01522
-6	0.013652	0.012526	0	-0.01253	-0.01365
-4	0.011897	0.011194	0	-0.01119	-0.0119
-2	0.010111	0.009831	0	-0.00983	-0.01011
0	0.008502	0.008815	0	-0.00881	-0.0085
2	0.0064	0.007357	0	-0.00736	-0.0064
4	0.003974	0.005744	0	-0.00574	-0.00397
6	0.002268	0.003894	0	-0.00389	-0.00227
8	0.000401	0.001823	0	-0.00182	-0.0004
10	-0.00144	-0.00034	0	0.000341	0.001443
12	-0.00337	-0.00252	0	0.002523	0.003373
14	-0.00505	-0.00526	0	0.005261	0.005049
16	-0.00696	-0.0082	0	0.008202	0.006964
18	-0.00901	-0.01121	0	0.011207	0.00901
20	-0.01151	-0.01416	0	0.014162	0.011507

Table A.4 Aerodynamic Coefficients for $TWA = 45^\circ$

Lift Coefficient					
	-30	-15	0	15	30
-14	-0.5862	-0.4702	-0.5007	-0.4702	-0.5862
-12	-0.2926	-0.3578	-0.3813	-0.3578	-0.2926
-10	-0.2249	-0.2407	-0.2558	-0.2407	-0.2249
-8	-0.1342	-0.1193	-0.1235	-0.1193	-0.1342
-6	-0.0388	0.00837	0.01351	0.00837	-0.0388
-4	0.0613	0.13637	0.14996	0.13637	0.0613
-2	0.16833	0.26765	0.29021	0.26765	0.16833
0	0.27495	0.39685	0.43211	0.39685	0.27495
2	0.3749	0.52326	0.56899	0.52326	0.3749
4	0.47736	0.64473	0.69967	0.64473	0.47736
6	0.57495	0.76442	0.82571	0.76442	0.57495
8	0.67031	0.87935	0.95088	0.87935	0.67031
10	0.76554	0.99464	1.07496	0.99464	0.76554
12	0.85745	1.11182	1.19739	1.11182	0.85745
14	0.95335	1.22186	1.3125	1.22186	0.95335
16	1.04658	1.33776	1.43015	1.33776	1.04658
18	1.14636	1.44875	1.54624	1.44875	1.14636
20	1.23799	1.56011	1.6654	1.56011	1.23799

Drag Coefficient					
	-30	-15	0	15	30
-14	0.26701	0.38851	0.44917	0.38851	0.26701
-12	0.16906	0.33154	0.38783	0.33154	0.16906
-10	0.13399	0.28315	0.33558	0.28315	0.13399
-8	0.10691	0.24308	0.29146	0.24308	0.10691
-6	0.08662	0.20969	0.256	0.20969	0.08662
-4	0.0679	0.18506	0.22755	0.18506	0.0679
-2	0.05462	0.16477	0.2061	0.16477	0.05462
0	0.04858	0.15058	0.19116	0.15058	0.04858
2	0.04737	0.14346	0.18574	0.14346	0.04737
4	0.05133	0.14684	0.19024	0.14684	0.05133
6	0.05873	0.15598	0.20202	0.15598	0.05873
8	0.0708	0.16935	0.21908	0.16935	0.0708
10	0.08654	0.18791	0.23999	0.18791	0.08654
12	0.10473	0.2123	0.26583	0.2123	0.10473
14	0.12779	0.24097	0.2958	0.24097	0.12779
16	0.15401	0.27467	0.3302	0.27467	0.15401
18	0.18424	0.31266	0.36896	0.31266	0.18424
20	0.21771	0.35626	0.41377	0.35626	0.21771

Roll Coefficient					
	-30	-15	0	15	30
-14	-0.0144	-0.0245	0	0.02453	0.01436
-12	-0.0358	-0.0208	0	0.02078	0.03576
-10	-0.0258	-0.0178	0	0.01779	0.02577
-8	-0.0187	-0.0148	0	0.01479	0.01874
-6	-0.0129	-0.0124	0	0.01237	0.01288
-4	-0.0078	-0.0102	0	0.01022	0.00784
-2	-0.004	-0.0077	0	0.00772	0.00399
0	-2E-05	-0.005	0	0.00499	2E-05
2	0.00429	-0.002	0	0.00197	-0.0043
4	0.00798	0.00077	0	-0.0008	-0.008
6	0.01203	0.00367	0	-0.0037	-0.012
8	0.0156	0.00643	0	-0.0064	-0.0156
10	0.01875	0.00911	0	-0.0091	-0.0188
12	0.02161	0.01147	0	-0.0115	-0.0216
14	0.02379	0.01386	0	-0.0139	-0.0238
16	0.026	0.01588	0	-0.0159	-0.026
18	0.02744	0.01781	0	-0.0178	-0.0274
20	0.02963	0.01954	0	-0.0195	-0.0296

Pitch Coefficient					
	-30	-15	0	15	30
-14	0.11104	0.08501	0.07738	0.08501	0.11104
-12	0.02703	0.03241	0.01932	0.03241	0.02703
-10	0.02079	-0.0089	-0.0235	-0.0089	0.02079
-8	-0.0046	-0.046	-0.0597	-0.046	-0.0046
-6	-0.0334	-0.0833	-0.0938	-0.0833	-0.0334
-4	-0.0582	-0.111	-0.1223	-0.111	-0.0582
-2	-0.0809	-0.136	-0.1492	-0.136	-0.0809
0	-0.0968	-0.1587	-0.1762	-0.1587	-0.0968
2	-0.1192	-0.1905	-0.199	-0.1905	-0.1192
4	-0.1459	-0.2187	-0.2206	-0.2187	-0.1459
6	-0.1745	-0.2518	-0.2438	-0.2518	-0.1745
8	-0.2032	-0.2858	-0.2762	-0.2858	-0.2032
10	-0.2319	-0.3191	-0.3133	-0.3191	-0.2319
12	-0.2638	-0.35	-0.3465	-0.35	-0.2638
14	-0.2955	-0.3831	-0.3783	-0.3831	-0.2955
16	-0.3294	-0.4161	-0.4094	-0.4161	-0.3294
18	-0.3648	-0.4531	-0.4419	-0.4531	-0.3648
20	-0.4023	-0.4941	-0.4796	-0.4941	-0.4023

Yaw Coefficient					
	-30	-15	0	15	30
-14	0.01832	0.03487	0	-0.0349	-0.0183
-12	0.04283	0.03052	0	-0.0305	-0.0428
-10	0.03172	0.02765	0	-0.0277	-0.0317
-8	0.02598	0.02516	0	-0.0252	-0.026
-6	0.02188	0.02288	0	-0.0229	-0.0219
-4	0.01781	0.02157	0	-0.0216	-0.0178
-2	0.01468	0.019	0	-0.019	-0.0147
0	0.01221	0.01613	0	-0.0161	-0.0122
2	0.00875	0.01259	0	-0.0126	-0.0088
4	0.00548	0.00952	0	-0.0095	-0.0055
6	0.00149	0.00629	0	-0.0063	-0.0015
8	-0.0017	0.0027	0	-0.0027	0.0017
10	-0.0045	-0.0005	0	0.00045	0.0045
12	-0.0074	-0.0029	0	0.00289	0.00738
14	-0.0094	-0.0053	0	0.0053	0.00938
16	-0.0116	-0.0072	0	0.00725	0.01156
18	-0.0131	-0.0092	0	0.00923	0.01315
20	-0.0155	-0.0111	0	0.01112	0.01549

Table A.5 Aerodynamic Coefficients for $TWA = 60^\circ$

Lift Coefficient					
	-30	-15	0	15	30
-14	-0,5205	-0,4042	-0,5751	-0,4042	-0,5205
-12	-0,3059	-0,3063	-0,4267	-0,3063	-0,3059
-10	-0,2225	-0,204	-0,2736	-0,204	-0,2225
-8	-0,1374	-0,0934	-0,1151	-0,0934	-0,1374
-6	-0,0478	0,02464	0,0459	0,02464	-0,0478
-4	0,04688	0,14895	0,2079	0,14895	0,04688
-2	0,1431	0,27475	0,37018	0,27475	0,1431
0	0,2386	0,39929	0,52531	0,39929	0,2386
2	0,33364	0,52041	0,67497	0,52041	0,33364
4	0,42744	0,63339	0,82418	0,63339	0,42744
6	0,51986	0,74274	0,97487	0,74274	0,51986
8	0,61236	0,85028	1,12779	0,85028	0,61236
10	0,70331	0,96197	1,27556	0,96197	0,70331
12	0,79448	1,06248	1,41699	1,06248	0,79448
14	0,88062	1,1677	1,55321	1,1677	0,88062
16	0,9749	1,27469	1,68324	1,27469	0,9749
18	1,06523	1,3791	1,80861	1,3791	1,06523
20	1,15315	1,48413	1,93016	1,48413	1,15315

Drag Coefficient					
	-30	-15	0	15	30
-14	0,31795	0,42497	0,46827	0,42497	0,31795
-12	0,24695	0,37866	0,40025	0,37866	0,24695
-10	0,21683	0,3391	0,34099	0,3391	0,21683
-8	0,19405	0,30464	0,29066	0,30464	0,19405
-6	0,17398	0,27486	0,25016	0,27486	0,17398
-4	0,15567	0,24828	0,21919	0,24828	0,15567
-2	0,14221	0,23004	0,201	0,23004	0,14221
0	0,13449	0,22078	0,19377	0,22078	0,13449
2	0,13213	0,22001	0,19206	0,22001	0,13213
4	0,13747	0,22747	0,19979	0,22747	0,13747
6	0,14336	0,24004	0,21524	0,24004	0,14336
8	0,15273	0,25617	0,23705	0,25617	0,15273
10	0,16501	0,27568	0,26503	0,27568	0,16501
12	0,18003	0,29717	0,29818	0,29717	0,18003
14	0,19869	0,32367	0,3359	0,32367	0,19869
16	0,22116	0,35302	0,37609	0,35302	0,22116
18	0,24645	0,38569	0,41934	0,38569	0,24645
20	0,2755	0,42345	0,468	0,42345	0,2755

Roll Coefficient					
	-30	-15	0	15	30
-14	-0,0118	-0,0203	0	0,02029	0,01176
-12	-0,0189	-0,0168	0	0,01684	0,01894
-10	-0,0133	-0,0133	0	0,01334	0,01329
-8	-0,0088	-0,0102	0	0,0102	0,00878
-6	-0,0047	-0,0073	0	0,00729	0,00475
-4	-0,0007	-0,0045	0	0,00446	0,00066
-2	0,00344	-0,0018	0	0,00177	-0,0034
0	0,00735	0,00082	0	-0,0008	-0,0074
2	0,01092	0,00358	0	-0,0036	-0,0109
4	0,01387	0,00592	0	-0,0059	-0,0139
6	0,01658	0,00794	0	-0,0079	-0,0166
8	0,01888	0,00992	0	-0,0099	-0,0189
10	0,02111	0,01184	0	-0,0118	-0,0211
12	0,0231	0,01367	0	-0,0137	-0,0231
14	0,02502	0,01543	0	-0,0154	-0,025
16	0,02656	0,01714	0	-0,0171	-0,0266
18	0,02805	0,01878	0	-0,0188	-0,0281
20	0,02957	0,02036	0	-0,0204	-0,0296

Pitch Coefficient					
	-30	-15	0	15	30
-14	0,08377	0,06922	-0,0367	0,06922	0,08377
-12	0,04691	0,03151	-0,0828	0,03151	0,04691
-10	0,02421	0,0041	-0,1192	0,0041	0,02421
-8	0,00835	-0,0208	-0,144	-0,0208	0,00835
-6	-0,0086	-0,0443	-0,1618	-0,0443	-0,0086
-4	-0,0303	-0,0759	-0,176	-0,0759	-0,0303
-2	-0,0481	-0,1039	-0,1808	-0,1039	-0,0481
0	-0,0678	-0,127	-0,175	-0,127	-0,0678
2	-0,087	-0,1484	-0,1766	-0,1484	-0,087
4	-0,0985	-0,1657	-0,1878	-0,1657	-0,0985
6	-0,1187	-0,1828	-0,2082	-0,1828	-0,1187
8	-0,1399	-0,2	-0,2335	-0,2	-0,1399
10	-0,159	-0,2158	-0,2573	-0,2158	-0,159
12	-0,1798	-0,2327	-0,2793	-0,2327	-0,1798
14	-0,2029	-0,2525	-0,2968	-0,2525	-0,2029
16	-0,224	-0,2755	-0,3154	-0,2755	-0,224
18	-0,2481	-0,3007	-0,3325	-0,3007	-0,2481
20	-0,2743	-0,3241	-0,3553	-0,3241	-0,2743

Yaw Coefficient					
	-30	-15	0	15	30
-14	0,01745	0,04066	0	-0,0407	-0,0174
-12	0,03346	0,03505	0	-0,0351	-0,0335
-10	0,02452	0,02929	0	-0,0293	-0,0245
-8	0,0188	0,0241	0	-0,0241	-0,0188
-6	0,01363	0,01954	0	-0,0195	-0,0136
-4	0,00802	0,01339	0	-0,0134	-0,008
-2	0,0021	0,00932	0	-0,0093	-0,0021
0	-0,0035	0,00576	0	-0,0058	0,0035
2	-0,0085	0,00292	0	-0,0029	0,00849
4	-0,0118	0,00014	0	-0,0001	0,01178
6	-0,0153	-0,0007	0	0,00067	0,01531
8	-0,018	-0,0028	0	0,00276	0,01804
10	-0,0207	-0,0052	0	0,00515	0,02068
12	-0,0229	-0,0076	0	0,00762	0,02287
14	-0,0254	-0,0091	0	0,00912	0,02545
16	-0,0275	-0,0108	0	0,01082	0,02752
18	-0,0296	-0,0122	0	0,01217	0,02956
20	-0,0317	-0,0141	0	0,01412	0,03166

Table A.6 Aerodynamic Coefficients for $TWA = 75^\circ$

Lift Coefficient					
	-30	-15	0	15	30
-14	-0,4171	-0,3459	-0,3573	-0,3459	-0,4171
-12	-0,2216	-0,2479	-0,248	-0,2479	-0,2216
-10	-0,1376	-0,1471	-0,1316	-0,1471	-0,1376
-8	-0,0485	-0,033	-0,0015	-0,033	-0,0485
-6	0,04628	0,09343	0,13485	0,09343	0,04628
-4	0,14211	0,22687	0,27556	0,22687	0,14211
-2	0,2365	0,35695	0,41948	0,35695	0,2365
0	0,33183	0,48269	0,5605	0,48269	0,33183
2	0,42277	0,60183	0,69055	0,60183	0,42277
4	0,51057	0,71244	0,81258	0,71244	0,51057
6	0,59966	0,81799	0,93408	0,81799	0,59966
8	0,68898	0,92085	1,0467	0,92085	0,68898
10	0,76942	1,02634	1,16095	1,02634	0,76942
12	0,85933	1,12763	1,26974	1,12763	0,85933
14	0,94556	1,22786	1,3698	1,22786	0,94556
16	1,03423	1,33054	1,47259	1,33054	1,03423
18	1,12037	1,43597	1,57316	1,43597	1,12037
20	1,20772	1,5407	1,6865	1,5407	1,20772

Drag Coefficient					
	-30	-15	0	15	30
-14	0,3392	0,44361	0,42542	0,44361	0,3392
-12	0,2849	0,40184	0,37413	0,40184	0,2849
-10	0,25566	0,36483	0,33086	0,36483	0,25566
-8	0,23437	0,32892	0,29341	0,32892	0,23437
-6	0,21832	0,30051	0,26358	0,30051	0,21832
-4	0,20924	0,27764	0,24278	0,27764	0,20924
-2	0,19871	0,26154	0,22804	0,26154	0,19871
0	0,19478	0,25427	0,21984	0,25427	0,19478
2	0,1947	0,25428	0,22147	0,25428	0,1947
4	0,19888	0,26246	0,23042	0,26246	0,19888
6	0,20776	0,27736	0,24761	0,27736	0,20776
8	0,22032	0,29428	0,26828	0,29428	0,22032
10	0,23508	0,31773	0,29246	0,31773	0,23508
12	0,25726	0,34408	0,32023	0,34408	0,25726
14	0,27966	0,37309	0,35076	0,37309	0,27966
16	0,30197	0,40526	0,38391	0,40526	0,30197
18	0,32651	0,44162	0,41837	0,44162	0,32651
20	0,35591	0,48357	0,4617	0,48357	0,35591

Roll Coefficient					
	-30	-15	0	15	30
-14	-0,0033	-0,0098	0	0,0098	0,00335
-12	-0,0076	-0,0076	0	0,00759	0,00765
-10	-0,0048	-0,0055	0	0,00553	0,00476
-8	-0,0023	-0,0037	0	0,00368	0,00234
-6	-0,0002	-0,002	0	0,00204	0,00019
-4	0,00225	-0,0002	0	0,00023	-0,0023
-2	0,00491	0,00151	0	-0,0015	-0,0049
0	0,00725	0,00357	0	-0,0036	-0,0073
2	0,0095	0,00567	0	-0,0057	-0,0095
4	0,01139	0,00735	0	-0,0073	-0,0114
6	0,01299	0,00875	0	-0,0088	-0,013
8	0,01475	0,01013	0	-0,0101	-0,0147
10	0,01622	0,01132	0	-0,0113	-0,0162
12	0,0174	0,01246	0	-0,0125	-0,0174
14	0,01854	0,01342	0	-0,0134	-0,0185
16	0,01958	0,01442	0	-0,0144	-0,0196
18	0,02061	0,01537	0	-0,0154	-0,0206
20	0,02162	0,01604	0	-0,016	-0,0216

Pitch Coefficient					
	-30	-15	0	15	30
-14	0,00722	0,00946	0,01067	0,00946	0,00722
-12	-0,0089	-0,0079	-0,0123	-0,0079	-0,0089
-10	-0,0154	-0,0184	-0,0255	-0,0184	-0,0154
-8	-0,0212	-0,0254	-0,0372	-0,0254	-0,0212
-6	-0,0229	-0,0328	-0,0487	-0,0328	-0,0229
-4	-0,0237	-0,0454	-0,0603	-0,0454	-0,0237
-2	-0,0307	-0,0642	-0,0746	-0,0642	-0,0307
0	-0,0339	-0,0745	-0,092	-0,0745	-0,0339
2	-0,042	-0,0875	-0,1017	-0,0875	-0,042
4	-0,0513	-0,1004	-0,1107	-0,1004	-0,0513
6	-0,0611	-0,107	-0,116	-0,107	-0,0611
8	-0,0715	-0,1129	-0,12	-0,1129	-0,0715
10	-0,0779	-0,121	-0,1266	-0,121	-0,0779
12	-0,0876	-0,122	-0,1315	-0,122	-0,0876
14	-0,0978	-0,1363	-0,1345	-0,1363	-0,0978
16	-0,116	-0,1509	-0,1412	-0,1509	-0,116
18	-0,1329	-0,1623	-0,1557	-0,1623	-0,1329
20	-0,148	-0,1783	-0,1779	-0,1783	-0,148

Yaw Coefficient					
	-30	-15	0	15	30
-14	0,01187	0,04152	0	-0,0415	-0,0119
-12	0,02481	0,03236	0	-0,0324	-0,0248
-10	0,01515	0,02421	0	-0,0242	-0,0152
-8	0,00831	0,01641	0	-0,0164	-0,0083
-6	0,002	0,01091	0	-0,0109	-0,002
-4	-0,0047	0,00541	0	-0,0054	0,00466
-2	-0,012	-0,0013	0	0,00128	0,01197
0	-0,0185	-0,0076	0	0,00763	0,01847
2	-0,0256	-0,0149	0	0,01489	0,02561
4	-0,0316	-0,0187	0	0,01871	0,03158
6	-0,0354	-0,0222	0	0,02218	0,03539
8	-0,0395	-0,0259	0	0,02594	0,03951
10	-0,0423	-0,0285	0	0,02854	0,04235
12	-0,0431	-0,0309	0	0,03085	0,04314
14	-0,0449	-0,0319	0	0,03186	0,04494
16	-0,0471	-0,0332	0	0,03318	0,04706
18	-0,0492	-0,035	0	0,03498	0,04915
20	-0,0511	-0,0358	0	0,03585	0,05114

Table A.7 Aerodynamic Coefficients for $TWA = 90^\circ$

Lift Coefficient					
	-30	-15	0	15	30
-14	-0,3602	-0,4124	-0,4464	-0,4124	-0,3602
-12	-0,2768	-0,2928	-0,3055	-0,2928	-0,2768
-10	-0,1713	-0,1684	-0,163	-0,1684	-0,1713
-8	-0,0548	-0,0387	-0,014	-0,0387	-0,0548
-6	0,06931	0,09664	0,13878	0,09664	0,06931
-4	0,19116	0,24051	0,30066	0,24051	0,19116
-2	0,31228	0,39385	0,47021	0,39385	0,31228
0	0,42426	0,54387	0,6388	0,54387	0,42426
2	0,53268	0,68204	0,77534	0,68204	0,53268
4	0,63334	0,80999	0,89365	0,80999	0,63334
6	0,72902	0,9316	1,01752	0,9316	0,72902
8	0,81793	1,0479	1,13629	1,0479	0,81793
10	0,90188	1,14967	1,24131	1,14967	0,90188
12	0,98113	1,24457	1,33285	1,24457	0,98113
14	1,05325	1,33293	1,41593	1,33293	1,05325
16	1,12353	1,40953	1,49502	1,40953	1,12353
18	1,18896	1,48053	1,56711	1,48053	1,18896
20	1,24499	1,54263	1,62917	1,54263	1,24499

Drag Coefficient					
	-30	-15	0	15	30
-14	0,299	0,38414	0,39822	0,38414	0,299
-12	0,25955	0,34758	0,35185	0,34758	0,25955
-10	0,24794	0,3165	0,31185	0,3165	0,24794
-8	0,24331	0,29024	0,27781	0,29024	0,24331
-6	0,24372	0,26771	0,24928	0,26771	0,24372
-4	0,24237	0,25137	0,22853	0,25137	0,24237
-2	0,2351	0,24396	0,21659	0,24396	0,2351
0	0,22849	0,24449	0,21673	0,24449	0,22849
2	0,22545	0,25456	0,22685	0,25456	0,22545
4	0,2262	0,27126	0,24095	0,27126	0,2262
6	0,23414	0,29004	0,26746	0,29004	0,23414
8	0,24871	0,31293	0,29905	0,31293	0,24871
10	0,26816	0,33353	0,33089	0,33353	0,26816
12	0,29034	0,36221	0,3679	0,36221	0,29034
14	0,31491	0,39865	0,40394	0,39865	0,31491
16	0,34416	0,43729	0,44299	0,43729	0,34416
18	0,37354	0,48128	0,49041	0,48128	0,37354
20	0,40485	0,5301	0,54194	0,5301	0,40485

Roll Coefficient					
	-30	-15	0	15	30
-14	-0,0047	-0,0027	0	0,00266	0,00474
-12	-0,0034	-0,0025	0	0,00251	0,00343
-10	-0,0035	-0,0026	0	0,00255	0,00347
-8	-0,0035	-0,0028	0	0,00281	0,00354
-6	-0,0036	-0,0028	0	0,00277	0,00364
-4	-0,0039	-0,003	0	0,00296	0,00388
-2	-0,0042	-0,0032	0	0,00316	0,00419
0	-0,0045	-0,0036	0	0,00365	0,0045
2	-0,0047	-0,0038	0	0,0038	0,00467
4	-0,0049	-0,0038	0	0,00383	0,0049
6	-0,0051	-0,0039	0	0,00389	0,00506
8	-0,0053	-0,0039	0	0,00394	0,00532
10	-0,0056	-0,0041	0	0,00414	0,00558
12	-0,006	-0,0044	0	0,00437	0,00597
14	-0,0063	-0,0042	0	0,00423	0,00626
16	-0,0063	-0,0043	0	0,00431	0,00627
18	-0,0063	-0,0044	0	0,00438	0,00634
20	-0,0065	-0,0044	0	0,00441	0,00646

Pitch Coefficient					
	-30	-15	0	15	30
-14	-0,044	-0,0417	-0,078	-0,0417	-0,044
-12	-0,0123	-0,0427	-0,0818	-0,0427	-0,0123
-10	-0,0092	-0,042	-0,08	-0,042	-0,0092
-8	-0,0062	-0,0423	-0,071	-0,0423	-0,0062
-6	0,00365	-0,0431	-0,0701	-0,0431	0,00365
-4	0,01824	-0,0473	-0,0708	-0,0473	0,01824
-2	0,02653	-0,0429	-0,0641	-0,0429	0,02653
0	0,02931	-0,0393	-0,0556	-0,0393	0,02931
2	0,02459	-0,0384	-0,0491	-0,0384	0,02459
4	0,01624	-0,0338	-0,0436	-0,0338	0,01624
6	0,01344	-0,0275	-0,0346	-0,0275	0,01344
8	0,01466	-0,0111	-0,0266	-0,0111	0,01466
10	0,01583	-0,0121	-0,0265	-0,0121	0,01583
12	0,01261	-0,009	-0,0166	-0,009	0,01261
14	0,00904	-0,0076	-0,0089	-0,0076	0,00904
16	0,00915	-0,0073	-0,0068	-0,0073	0,00915
18	0,00531	-0,0046	-0,0016	-0,0046	0,00531
20	-0,0022	0,00507	0,00534	0,00507	-0,0022

Yaw Coefficient					
	-30	-15	0	15	30
-14	-0,0309	-0,0313	0	0,0313	0,03093
-12	-0,0153	-0,0251	0	0,02508	0,01533
-10	-0,0078	-0,0191	0	0,01908	0,00776
-8	-0,001	-0,0115	0	0,01146	0,00102
-6	0,00493	-0,0035	0	0,00345	-0,0049
-4	0,01114	0,00591	0	-0,0059	-0,0111
-2	0,01857	0,01214	0	-0,0121	-0,0186
0	0,02608	0,01738	0	-0,0174	-0,0261
2	0,0335	0,02208	0	-0,0221	-0,0335
4	0,04226	0,02708	0	-0,0271	-0,0423
6	0,04893	0,03108	0	-0,0311	-0,0489
8	0,05507	0,03435	0	-0,0343	-0,0551
10	0,06024	0,04108	0	-0,0411	-0,0602
12	0,06463	0,0462	0	-0,0462	-0,0646
14	0,06831	0,04477	0	-0,0448	-0,0683
16	0,07071	0,04708	0	-0,0471	-0,0707
18	0,0742	0,04911	0	-0,0491	-0,0742
20	0,07732	0,05157	0	-0,0516	-0,0773

B. Linearized System Matrices

$$A_{00} =$$

-0.2447	-0.0077	0.5662	-0.0000	2.6440	-0.0000	0.0000	-0.7121	0.1242	0	0	0
-0.0000	-0.0615	0.0000	-0.1893	0.0001	-0.0001	9.8090	0.0000	0.9861	0	0	0
-0.8789	-0.0212	-5.9750	-0.0000	-128.70	0.0000	0.0000	-96.0000	0.3403	0	0	0
-0.0000	0.0829	0.0000	-29.6600	0.0143	-0.0132	-0.0004	0.0006	-1.3310	0	0	0
0.0100	0.0081	-1.1460	0.0016	-417.60	0.0000	-0.0000	-18.4100	-0.1302	0	0	0
0.0000	-0.0882	-0.0000	-3.2090	-0.0011	-0.0004	-0.0091	-0.0001	1.4170	0	0	0
0	0	0	1.0000	0	0	0	0	0	0	0	0
0	0	0	0	1.0000	0	0	0	0	0	0	0
0	0	0	0	0	1.0000	0	0	0	0	0	0
1.0000	0	0	0	0	0	0	0	0	0	0	0
0	1.0000	0	0	0	0	0	0	0	0	0	0
0	0	1.0000	0	0	0	0	0	0	0	0	0

$$B_{00} =$$

0.0013	0.7513	-0.0061	0.0086	0	0	0	0	0	0	0	0
-0.1838	0.0000	0.0000	0.0000	0	0	0	0	0	0	0	0
0.0001	-4.6000	0.0206	0.0000	0	0	0	0	0	0	0	0
-29.0100	0.0008	0.0005	0.0005	0	0	0	0	0	0	0	0
-0.2042	-24.66	0.0003	-0.0004	0	0	0	0	0	0	0	0
0.6028	-0.0001	0.0148	0.0148	0	0	0	0	0	0	0	0
0	0	0	0	0	0	0	0	0	0	0	0
0	0	0	0	0	0	0	0	0	0	0	0
0	0	0	0	0	0	0	0	0	0	0	0
0	0	0	0	0	0	0	0	0	0	0	0
0	0	0	0	0	0	0	0	0	0	0	0
0	0	0	0	0	0	0	0	0	0	0	0

$$Q_{00} =$$

1000	0	0	0	0	0	0	0	0	0	0	0
0	1000	0	0	0	0	0	0	0	0	0	0
0	0	1000	0	0	0	0	0	0	0	0	0
0	0	0	3282	0	0	0	0	0	0	0	0
0	0	0	0	3282	0	0	0	0	0	0	0
0	0	0	0	0	32820	0	0	0	0	0	0
0	0	0	0	0	0	3282	0	0	0	0	0
0	0	0	0	0	0	0	3282	0	0	0	0
0	0	0	0	0	0	0	0	32820	0	0	0
0	0	0	0	0	0	0	0	0	1.0000	0	0
0	0	0	0	0	0	0	0	0	0	1.0000	0
0	0	0	0	0	0	0	0	0	0	0	200000

$$A_{90} =$$

-1.3360	0.0039	0.0013	-0.0000	-20.6600	0.0000	-0.0000	-9.8260	0.0000	0	0	0
-0.0000	-0.0639	-0.0000	-0.0000	0.0000	-0.0000	9.8140	0.0000	-0.0041	0	0	0
-0.0729	0.0081	-0.1658	-0.0000	-0.0438	0.0000	-0.0001	0.0036	0.0000	0	0	0
-0.0000	-0.0017	0.0000	0.0000	0.0007	-0.0002	0.0005	-0.0000	0.0000	0	0	0
0.3305	-0.0023	-0.0283	0.0000	-68.0100	0.0000	0.0000	0.0031	-0.0000	0	0	0
0.0000	0.0001	-0.0000	-0.0001	-0.0014	-0.0000	0.0182	0.0000	0.0000	0	0	0
0	0	0	1.0000	0	0	0	0	0	0	0	0
0	0	0	0	1.0000	0	0	0	0	0	0	0
0	0	0	0	0	1.0000	0	0	0	0	0	0
1.0000	0	0	0	0	0	0	0	0	0	0	0
0	1.0000	0	0	0	0	0	0	0	0	0	0
0	0	1.0000	0	0	0	0	0	0	0	0	0

$$B_{90} =$$

-3.4650	-1.2920	0.0001	-0.0001	0.0000	0.0000	0	0	0	0	0	0
0.0000	0.0000	0.0004	0.0004	0.0000	0.0000	0	0	0	0	0	0
0.0443	-0.0853	0.0169	-0.0189	0.0012	-0.0012	0	0	0	0	0	0
0.0000	0.0000	0.0517	0.0517	0.0016	0.0016	0	0	0	0	0	0
-0.1255	-0.1127	-0.0100	0.0098	0.0068	-0.0068	0	0	0	0	0	0
0	0	0	0	0	0	0	0	0	0	0	0
0	0	0	0	0	0	0	0	0	0	0	0
0	0	0	0	0	0	0	0	0	0	0	0
0	0	0	0	0	0	0	0	0	0	0	0
0	0	0	0	0	0	0	0	0	0	0	0
0	0	0	0	0	0	0	0	0	0	0	0
0	0	0	0	0	0	0	0	0	0	0	0

$$Q_{90} =$$

1000	0	0	0	0	0	0	0	0	0	0	0
0	1000	0	0	0	0	0	0	0	0	0	0
0	0	1000	0	0	0	0	0	0	0	0	0
0	0	0	3282	0	0	0	0	0	0	0	0
0	0	0	0	3282	0	0	0	0	0	0	0
0	0	0	0	0	32820	0	0	0	0	0	0
0	0	0	0	0	0	3282	0	0	0	0	0
0	0	0	0	0	0	0	3282	0	0	0	0
0	0	0	0	0	0	0	0	32820	0	0	0
0	0	0	0	0	0	0	0	0	1.0000	0	0
0	0	0	0	0	0	0	0	0	0	1.0000	0
0	0	0	0	0	0	0	0	0	0	0	200000

CURRICULUM VITAE

PERSONAL INFORMATION

Surname, Name: Çakır, Hasan
Nationality: Turkish (TC)
Date and Place of Birth: 10 July 1988, Gaziantep
Marital Status: Married
Phone: +90 312 414 22 44
email: e204293@metu.edu.tr

EDUCATION

Degree	Institution	Year of Graduation
MS	METU Aerospace Engineering	2015
BS	Turkish Air Force Academy Aeronautical Engineering	2010
High School	Işıklar Military High School, Bursa	2006

WORK EXPERIENCE

Year	Place	Enrollment
2016-Present	National Combat Aircraft Division/TurAF/Ankara	Project Officer
2014-2016	3 rd Air Maintenance Center/Ankara	Project Officer
2010-2014	1 st Main Jet Base	Maintenance Officer

FOREIGN LANGUAGES

Advanced English

PUBLICATIONS

1. Çakır H., Kurtuluş D.F. "Dikey İniş/Kalkış Yapabilen Hareketli Kanatlı İnsansız Hava Aracının Tasarımı", VI. Ulusal Havacılık ve Uzay Konferansı (2016)
2. Çakır H., Kurtuluş D.F. "Hovering Control of A Tilt-Wing UAV", 10th Ankara International Aerospace Conference (2019)
3. Çakır H., Kurtuluş D.F. "Design and Aerodynamic Analysis of a VTOL Tilt-Wing UAV", Aerospace Science and Technology (2020) (Under preparation)

4. Çakır H., Kurtuluş D.F. "Modeling and Controller Design of a Tilt-Wing UAV ",
Aerospace Science and Technology (2020) (Under preparation)

Model Airplanes, Computer Technologies, Movies, Books